

DISSERTATION

submitted to the

Combined Faculties for the Natural Sciences and for
Mathematics of the Ruperto-Carola-University of
Heidelberg, Germany

and

the Université Paris VI, Frankreich

for the degree of

Doctor of Natural Science

Put forward by

Pia STREICHER

born in

Worms, Germany

Oral examination: November 28th 2008

Studying Integrin-Mediated Cell Spreading Using a Biomimetic System

Referees:

Prof. Dr. Joachim Spatz
Prof. Dr. Valérie Marchi-Artzner

English Abstract

A novel system mimicking the first steps of integrin-mediated cell spreading was developed and characterized. This was achieved by reconstituting the transmembrane protein integrin $\alpha_{IIb}\beta_3$ into giant unilamellar vesicles (GUVs). The method consisted of a detergent-mediated reconstitution of solubilized integrins into small proteoliposomes (0.1 - 0.2 μm in size) followed by electroswelling of a partially dried film of the same proteoliposomes. The reconstitution process was validated by analyzing protein incorporation and biological activity. Biological activity of integrin in GUVs was also confirmed by adhesion tests using biofunctionalized surface. The adhesion dynamics was studied experimentally and the results compared to theoretical predictions. The adhesion started with the spontaneous formation of several small (~ 200 nm) domains of tight adhesion, which grew and eventually fuse to form a ring-shaped adhesive patch at the border of the contact zone. This ring grew toward the center until it formed a uniformly adhering zone. Three distinct regimes were identified: For the first regime, the single adhesion zones were predicted to grow with $R \sim t^{5/8}$, which agreed well with our experimental data. Disk formation in the third regime was predicted to proceed with $R_i \sim -t$, which matched the experimental data.

In dieser Arbeit beschreiben wir zum erstmals ein experimentelles System, welches die ersten Schritte der Integrin-vermittelten Zelladhäsion nachahmt. Mit Hilfe einer zuvor in der Gruppe von P. Bassereau entwickelten Methode haben wir das transmembrane Protein Integrin $\alpha_{IIb}\beta_3$ in unilamellare Riesenvesikel rekonstituiert. Die Methode besteht aus einer Detergenz-vermittelten Rekonstitution in kleine Proteoliposomen (Durchmesser 0,1 - 0,2 μm). Im Anschluß werden diese Riesenvesikel mittels Elektroformation aus einem teilweise getrockneten Film dieser Proteoliposome erzeugt. Konfokalmikroskopische Untersuchungen zeigten, dass die fluoreszenzmarkierten Proteine homogen in die Riesenvesikel eingebracht wurden. Die Funktionalität des Integrins wurde mit Hilfe eines ELISA-Tests (enzyme-linked immunosorbent assay) auf kleinen Vesikeln überprüft. Eine spezifische Wechselwirkung zwischen in kleine Vesikel eingebrachtes Integrin und RGD-funktionalisierten Quantum Dots wurde ebenfalls nachgewiesen (RGD ist ein bekannter Integrin-Ligand). Darüber hinaus belegte der Adhäsionstests auf mit RGD biofunktionalisierten Oberflächen, dass die Proteine ihre biologische Aktivität auch nach der Elektroformation bewahren. Im weiteren wurde die Adhäsionsdynamik der Integrin-funktionalisierten Riesenvesikel auf RGD-beschichteten Oberflächen experimentell untersucht. Der Adhäsionsprozess kann in drei Sequenzen unterteilt werden, die experimentellen Daten der Sequenzen 1) und 3) wurden mit theoretischen Modellen verglichen. Es kann gezeigt werden, dass der Adhäsionsprozess in beiden Regimen durch die Diffusion der Liganden limitiert ist.

Key Words

1. cell adhesion
2. integrin
3. biomimetic system
4. giant unilamellar vesicle (GUV)

Mots Clés

1. adhésion cellulaire
2. intégrine
3. système biomimétique
4. vésicule géante

Schlagwörter

1. Zelladhäsion
2. Integrin
3. Biomimetisches System
4. Riesenvesikel

Contents

1	Introduction	1
2	Cell Adhesion Molecules and Integrins	5
A	Aspects of Cell Adhesion	5
B	The Integrins	7
B.1	The Integrin $\alpha_{IIb}\beta_3$	9
B.1.1	Activation and Binding	12
B.2	Examples of the Role of Integrin: Leukocytes and Platelets	13
B.2.1	Inflammation: Leukocyte Adhesion	13
B.2.2	Injury: Platelet Adhesion	18
C	Cell Spreading and Reorganization in vitro	20
D	Glossary	25
3	Biological and Model Membranes	31
A	Biological Membranes: Components and Characteristics	31
A.1	Lipids and Organisation in Lipid Bilayers	31
A.2	Mechanical Properties of Lipid bilayers	35
A.3	Vesicle Shapes	42
B	Model Membranes: Giant Unilamellar Vesicles	45
B.1	General Characteristics	45
B.2	Standard Methods for the Preparation of GUVs	45
B.2.1	Electroformation	45
B.2.2	Spontaneous Swelling	47
B.2.3	Electroinjection Technique	47
B.3	Functionalized Giant Unilamellar Vesicles	48
B.3.1	Methods to Reconstitute Membrane Proteins into GUVs	49

CONTENTS

	B.3.2	GUV Formation under Physiological Conditions	50
C		Interactions between Membranes	50
	C.1	Generic Interactions	51
		C.1.1 Van der Waals forces	51
		C.1.2 Repulsive Forces	51
	C.2	Specific Adhesion	51
		C.2.1 Techniques	54
		C.2.2 The example of the Streptavidin-biotin pair	55
4		Adhesion in Model Systems	59
A		Basic Principles	59
	A.1	Water Droplet on a Surface	59
	A.2	Adhesion of Vesicles : Static Approach	61
	A.3	Comparing Water Droplet and Vesicle Spreading	64
B		Theory: Adhesion Kinetics of Model Membranes Mediated by Specific Interactions	64
	B.1	Simulations	64
		B.1.1 Numerical Simulations on Spreading of a Model System for Cell Adhesion	64
	B.2	Analytical approaches	65
		B.2.1 Kinetics of membrane adhesion mediated by ligand-receptor interaction (Boulbitch et al. approach)	65
		B.2.2 Growth and Shape Stability in an Adhesion Plaque in the Diffusion-Mediated Regime (Shenoy et al.)	66
		B.2.3 A More General Approach: de Gennes and Brochard-Wyart	66
C		Experiments: Functionalized GUVs Mimicking Cell Adhesion	67
	C.1	Adhesion Dynamics of GUVs mediated by Biotin-Streptavidin Systems	67
		C.1.1 Immobile Receptors on the Substrate	67
		C.1.2 Mobile Receptors on the Substrate	69
	C.2	The Homophilic Receptor Contact Site A from <i>Dic-tyostelium Discoideum</i>	72
	C.3	The Ligand- Receptor Pair Sialyl-Lewis ^x - E-Selectin	73
	C.4	The Ligand-Receptor-Pair Integrin- RGD	73
5		The Minimal System	81
A		Reconstitution of integrin $\alpha_{IIb}\beta_3$ into Giant Unilamellar Vesicles	82
	A.1	General Scheme	82
	A.2	Challenges	86
		A.2.1 Other Tested Procedures	89

CONTENTS

A.2.1.1	Influence of Sucrose during Reconstitution	89
A.2.1.2	The Effect of Divalent Ions on the Growth of Vesicles	90
A.3	Summary	91
A.4	GUVs from Native Membranes	91
B	Incorporation and Functionality	93
B.1	ELISA-Test on Integrin-Containing SUVs	93
B.2	Confocal Microscopy	94
B.3	Quantum Dots Assay	94
B.3.1	Fluorescence Microscopy on Platelets	95
B.3.2	Spectrofluorimetry on Platelets	96
B.3.3	Spectrofluorimetry on Proteoliposomes	98
B.4	Adhesion Tests	99
B.4.1	Passivated Surfaces	99
B.4.1.1	PEG-Coated Surfaces	99
B.4.1.2	Casein-Coated Surfaces	101
B.4.2	Adhesive Surface	102
B.4.3	Adhesion Assay in the Presence of Soluble RGD	102
C	Conclusion	104
6	Adhesion Dynamics	105
A	Adhesion Dynamics: First Observations	105
B	Adhesion Dynamics: Detailed Description	109
B.1	Formation of Single Adhesion Patches	109
B.1.1	Theoretical Predictions	110
B.1.2	Comparison with Experimental Data	111
B.1.2.1	Fitting the Data	111
B.1.2.2	Discussion	112
B.1.3	Conclusion	114
B.2	Disk Formation	114
B.2.1	The Dewetting Velocity	117
B.2.2	Growth from the Edge of the Ring	118
B.2.3	Growth Acceleration at Longer Times	118
B.2.4	Mechanisms of Water Depletion	118
B.2.5	Conclusion	119
C	Conclusion and Perspective	119
7	Conclusion	121

CONTENTS

A	Materials and Methods	125
A	Materials	125
A.1	Lipids	125
A.2	Other Products	127
B	Methods	128
B	Experimental Techniques	129
A	Reflection Interference Contrast Microscopy (RICM)	129
B	Epifluorescence Microscopy	131
C	Phase Contrast Microscopy	133
D	Confocal Microscopy	134
C	Protocols for Protein Purification	137
A	Purification of the Human Platelet Membrane Glycoprotein $\alpha_{IIb}\beta_3$ complex	137
A.1	Buffers	137
A.2	Purification	139
A.3	Enzyme-Linked Immunosorbent Assay (ELISA)	141
A.3.1	Buffers	141
A.3.2	Preparation	142
A.4	Fluorescent labeling of the Human Platelet Membrane Glycoprotein $\alpha_{IIb}\beta_3$ complex [1]	143
B	Membrane Purification from Human Platelets	144
B.0.1	Buffers	144
B.1	Purification	145
D	Preparation Protocols for GUVs	147
A	Preparation of Giant Unilamellar Vesicles without integrin - Standard Protocol	147
B	Preparation of Giant Unilamellar Vesicles with integrin	147
B.1	Biobeads®Preparation	147
B.2	Initial Munich Protocol	148
B.3	Initial Paris Protocol	149
B.4	Final Paris Protocol (higher lipid-integrin-ratio)	150
C	Preparation of Giant Unilamellar Vesicles from purified platelet membranes	150
E	Protocols for Adhesive Surfaces and Adhesion Tests	153
A	Passivated Surfaces	153
A.1	Preparation of PEG surfaces	153
A.1.1	Silanisation	153
A.1.2	PEG Binding	154
A.1.3	Observation Chamber	154
A.2	Casein Surfaces	155

CONTENTS

A.3	Fibrinogen Surfaces	155
B	Adhesion Assay for Integrin-Containing GUVs	156
C	Adhesion Assay in the Presence of Soluble RGD	156
F	Protocols for Quantum Dot (QD) Assays	157
A	Fluorescence Microscopy of QDs	157
A.1	Fluorescence Microscopy of Platelets	158
B	Spectrofluorimetry	158
B.1	Protocol for Platelets	158
B.2	Protocol for Proteoliposomes	159

CONTENTS

CHAPTER 1

Introduction

More than a century ago, biologists described how cells differentiate and associate to form the different organs in living organisms. In turn, the cell is composed of many different sub-units (e.g. nucleus, mitochondria, Golgi apparatus, ribosomes,...) which allows the cell to act as a miniature "factory". This tremendous complexity is evident in the depiction of a typical eukaryotic cell shown in figure 1.1.

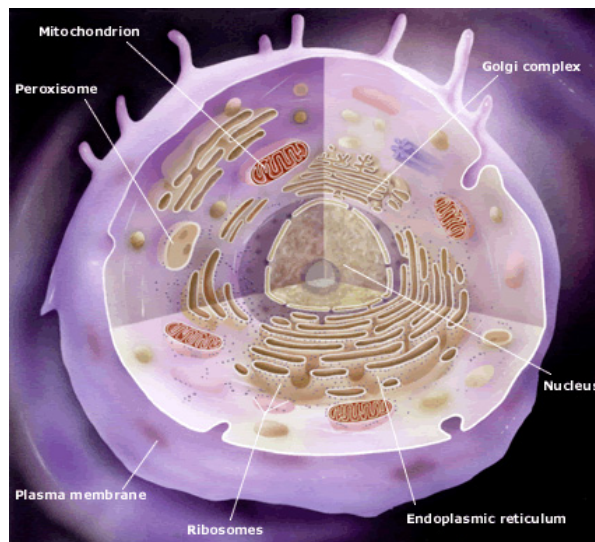


Figure 1.1. A typical eukaryotic cell. It contains intracellular compartments, such as the nucleus, the Golgi complex, mitochondria, ribosomes and the endoplasmic reticulum. From [2].

CHAPTER 1. INTRODUCTION

With the help of specific receptor proteins, cells can interact with each other or bind to the extracellular matrix. These interactions permit stable connections between the millions of cells in a tissue, while still allowing the tissue to reorganize and adapt in response to external signals. These complex processes require a huge number of proteins and other specialized molecules. The objective of this project was to establish a minimal system able to mimic the first stages of a cell undergoing protein-mediated adhesion to another cell or the extracellular matrix. We decided to focus on integrin $\alpha_{IIb}\beta_3$ and one of its ligands, the RGD-carrying protein fibrinogen, as their molecular and biochemical properties are fairly well known. The first step in integrin-mediated cell adhesion is thought to be the contact between integrin and ligands bearing the tripeptide RGD. In this work, we reconstituted integrin $\alpha_{IIb}\beta_3$ into giant unilamellar vesicles (= model cell) and studied their adhesion dynamics on fibrinogen-covered substrates. Our simple model system represents a "bottom-up" approach to study cell adhesion and reproduces several features of this complex biological process.

Outline:

Although other groups have previously develop model systems, integrin-mediated adhesion has not previously been studied with a system that closely mimics cell adhesion. The goal of this study was to prepare such a biomimetic system and to characterize it both from a functional and a physical point of view.

Chapter 2 reviews the basic biological principals of cell adhesion and spreading. Integrin-mediated adhesion is a highly complex and regulated process involving signals from the cytoplasm (inside-out signaling) and ECM (outside-in signaling), conformational changes of proteins, and biochemical modifications (phosphorylation or similar processes). The last part of the chapter focuses on the integrin family and in particular, integrin $\alpha_{IIb}\beta_3$.

Giant Unilamellar Vesicles (GUVs) are a very popular model for cells, as they share an important feature : the lipid bilayer. Chapter 3 reviews a number of experimental and theoretical studies of model systems containing lipid bilayers. Over the years biomimetic models of the cell membrane have been improved and complexified in order to better mimic biological cells.

The experimental and theoretical framework that inspired us to develop our biomimetic system are described in chapter 4. The work of the group of Prof. Sackmann (TU Munich, Germany) was particularly important in allowing us to develop our biomimetic system of integrin-mediated cell adhesion, but the experimental work and the theoretical framework of other studies are also presented in this chapter.

In Chapter 5, we describe the reconstitution of integrin $\alpha_{IIb}\beta_3$ into Giant Unilamellar Vesicles. The final protocol, the different trials to obtain a satisfactory result, and the assays to prove protein incorporation and functionality are all described. The aspects of proteoliposome preparation which proved to be important for the successful reconstitution of integrin $\alpha_{IIb}\beta_3$ are also discussed.

Chapter 6 describes the adhesion dynamics of the integrin-containing vesicles and the theoretical models of this process. Three different stages of adhesion are identified and the first and the last stages are discussed in detail.

The conclusion can be found in chapter 7.

In appendix B we present the experimental techniques used in this work.

Materials and methods can be found in appendix A.

Detailed protocols of experiments described in chapter 5 are described in the appendices C, D, E, and F.

This work greatly benefited from the expertise in the group of Prof. Sackmann concerning the purification of integrin $\alpha_{IIb}\beta_3$. This was combined with the protocol developed by Girard et al. [3] which was adapted and enhanced in order to reconstitute the integrin $\alpha_{IIb}\beta_3$ into giant unilamellar vesicles.

The presented project encountered several administrative and technical challenges which had to be overcome. First, insufficient amounts of human blood, needed for the purification of integrin $\alpha_{IIb}\beta_3$, were available in France. While the Red Cross in Germany was able to help us out, because it was not possible to get authorization to bring blood plasma to France we had to find a lab in Germany which was equipped for such a purification procedure and was willing to host us. We are very thankful that the E22 laboratory at TU Munich hosted us repeatedly and made its lab and expertise available to us. The continuous help and readiness of Monika Rusp and Michael Bärmann were indispensable for the success of the purification.

The integrin $\alpha_{IIb}\beta_3$ is a very large and fragile protein. Due to a limited life time of only 6 months after purification, we had to call upon this support on a regular basis.

Purification and functionality testing turned out to be difficult and time consuming. Frequently, the purification process either did not yield integrin or only in insufficient concentration or quality. Finally, GUVs could not be obtained as reproducibly as had been the case for simpler transmembrane proteins studied earlier [3], [4]. In combination, these difficulties made this project especially challenging and we were unable to achieve all of our initial research goals. However, we still succeeded reconstituting functional integrin into giant unilamellar vesicles which allowed us to then study the dynamics of their adhesion onto fibrinogen-coated substrates.

CHAPTER 1. INTRODUCTION

CHAPTER 2

Cell Adhesion Molecules and Integrins

Nota bene! A glossary with biological terms that might not be familiar to the reader can be found in section D. Words listed in the glossary are marked with a * in the text.

A Aspects of Cell Adhesion

Cell adhesion is crucial for the assembly of individual cells into three-dimensional tissues as well as for dynamic processes such as wound healing or cell migration. Cells do not simply "stick" together to form tissues, but are instead organized into very diverse and highly distinctive patterns. Tissue is constantly reorganizing via detachment and reattachment of cells, especially during development. A variety of cell adhesion mechanisms are responsible for assembling and reorganizing cells and, together with their connections to the cytoskeleton and the extracellular matrix, help determine the overall architecture of the tissue. The following section describes how this architecture is generated and maintained.

Typically, the functional units of cell adhesion are multi-protein complexes made up of three general classes of proteins (see figure 2.1 for a simplified schematic depiction):

1. *cell adhesion molecules (CAMs) / adhesion receptors*
2. *extracellular matrix (ECM) proteins*
3. *cytoplasmic proteins*

Cell adhesion molecules (CAMs) are usually transmembrane proteins that mediate binding interactions at the extracellular surface and determine the

CHAPTER 2. CELL ADHESION MOLECULES AND INTEGRINS A

specificity of cell-cell and cell-ECM recognition. They include members of the **integrin**, cadherin, immunoglobulin (Ig), selectin, and proteoglycan (for example, syndecans) superfamilies.

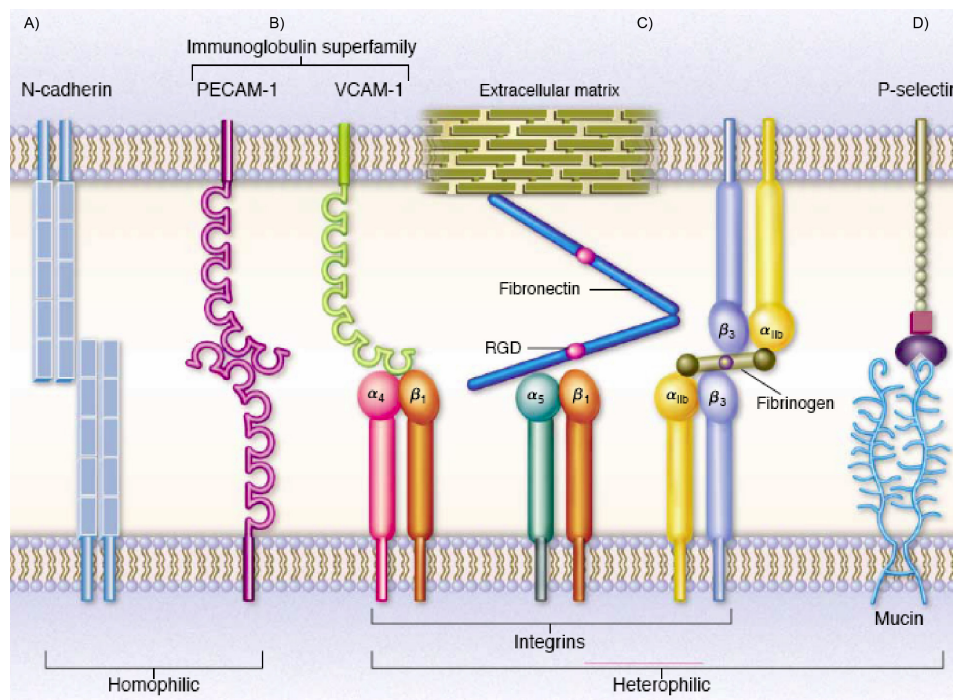


Figure 2.1. The four predominant families of adhesion molecules are a) cadherins, b) immunoglobulin (Ig) superfamily members, c) integrins, d) selectins. From [5]

On the extracellular side, the cell adhesion receptors recognize and interact with other cell adhesion molecules on neighboring cells or proteins of the *extracellular matrix (ECM)*. ECM proteins are large glycoproteins, including the collagens, fibronectins, laminins, and proteoglycans that assemble into fibrils or other complex macromolecular arrays. Owing to their binding to adhesion receptors, they can also be tightly associated with the cell surface. Figure 2.2 shows examples of adhesive interactions at different locations on a cell.

At the intracellular surface of the plasma membrane, cell adhesion receptors associate with *cytoplasmic plaque** or peripheral membrane proteins. Cytoplasmic plaque proteins serve to link the adhesion systems to the cytoskeleton, to regulate the functions of the adhesion molecules, and transduce signals initiated at the cell surface by the adhesion receptors.

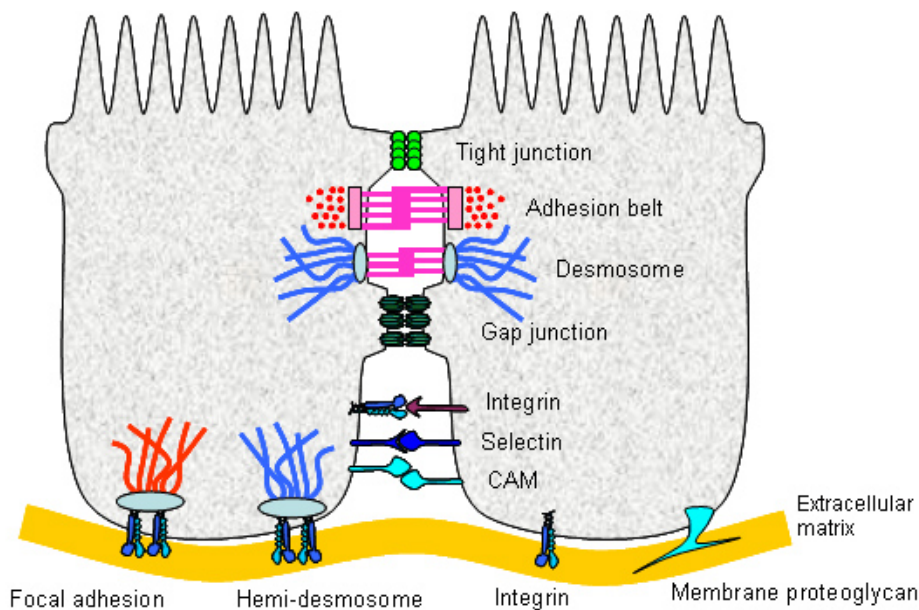


Figure 2.2. CAMs form different forms of adhesive interactions at different locations on the cell. From [6].

Maintaining a Tissue's Three-Dimensional Structure

Stable cell-cell connections are essential for maintaining the three-dimensional architecture of tissue. Although adhesive contacts between cells or between cells and the neighbouring tissue are generally stable, they should not be regarded as static, and in many cases the maintenance of stable connections requires active cellular processes. This will be discussed in connection with the protein class of integrins as they are of major interest for the presented project.

B The Integrins

Integrins are the major metazoan receptors for cell adhesion to extracellular matrix proteins and in vertebrates also play important roles in certain cell-cell adhesions. A schematic representation is presented in figure 2.3.

In addition to mediating cell adhesion, integrins make transmembrane connections to the cytoskeleton and activate many intracellular signaling pathways. Since the recognition of the integrin receptor family nearly 20 years ago [7], they have become the best-understood cell adhesion receptors. Integrins and their ligands play key roles in development, immune responses, leukocyte* trafficking, hemostasis, and cancer and malfunctioning or misregulated integrins are at the heart of many human diseases, including genetic, autoimmune, and other disorders. They are the target of effective therapeutic drugs against

CHAPTER 2. CELL ADHESION MOLECULES AND INTEGRINS B

thrombosis and inflammation, and they are receptors for many viruses and bacteria.

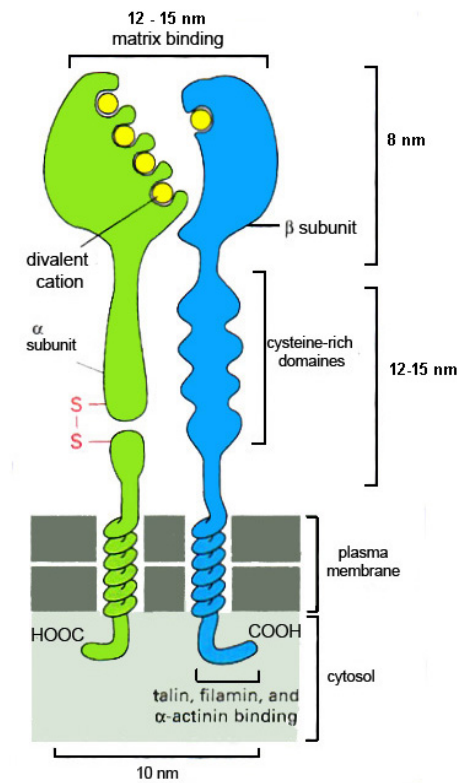


Figure 2.3. *The typical structure of an integrin. From [8].*

Integrins are restricted to the metazoa; no homologs are detected in prokaryotes, plants, or fungi [9]. The simplest metazoa, sponges and cnidaria*, have integrins [10], [11] and it is clear that primitive bilateria had at least two integrin $\alpha\beta$ heterodimers, the descendants of which persist to this day in organisms as diverse as flies, nematodes, and vertebrates [12]. In mammals, 19 α and 8 β subunits have been characterized, whereas the *Drosophila* and *Caenorhabditis* genomes encode only five α and two β subunits [13] (see figure 2.4 for an overview of currently known integrins).

A single β chain can interact with multiple α chains, forming integrins that bind to different ligands (see figure 2.4). The heterodimer complex requires divalent ions (Ca^{2+} or Mg^{2+} , depending on the integrin) reflecting the presence of divalent-cation binding domains in the extracellular part of the α and β subunits. The type of divalent cation can influence both the affinity and the

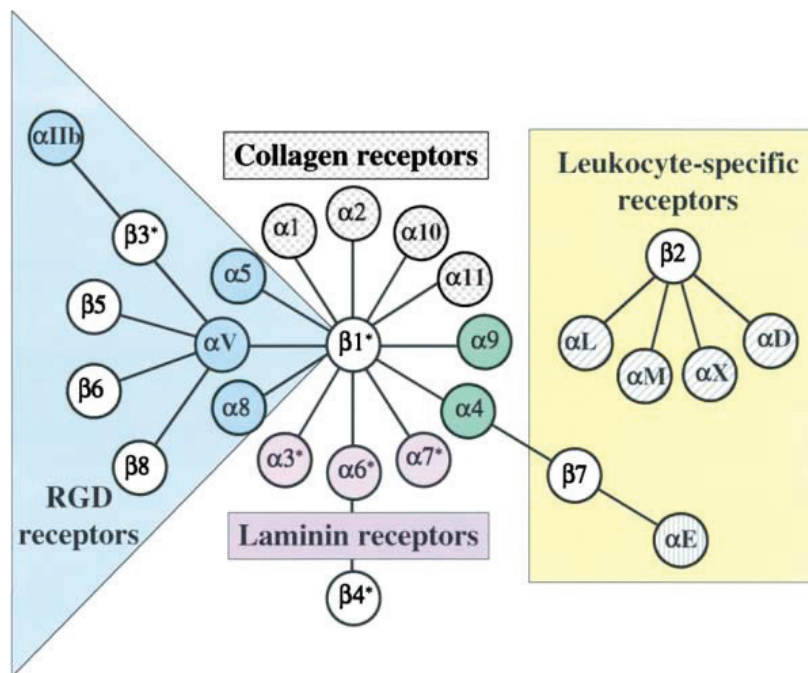


Figure 2.4. α and β subunits pair to form the large family of integrins. From [14].

specificity of the binding of an integrin to its ligand.

Most integrins are expressed on a variety of cells, and most cells express several integrins, enabling them to bind to several matrix molecules.

Integrins typically exhibit relatively low affinities for their ligands (dissociation constants K_D between 10^{-6} and 10^{-8} mol/L) compared with the high affinities (K_D values of 10^{-9} and 10^{-11} mol/L) for typical cell - surface hormone receptors. However, the multiple weak interactions generated by binding of hundreds or thousands of integrin molecules to ECM proteins allow a cell to remain firmly anchored to the matrix. Alternatively, in situations where cells are migrating, it is essential that the cells are able to make and break contacts with the ECM and this is facilitated if individual contacts are weak. Cells that express several different integrins that bind the same ligand often can selectively regulate the activity of each type of integrin, thereby fine-tuning their interaction with the matrix (see table 2.1).

B.1 The Integrin $\alpha_{IIb}\beta_3$

The integrin $\alpha_{IIb}\beta_3$ (GPIIb/IIIa following an old nomenclature) is the most abundant transmembrane protein on platelets* [15]. 3 % of the overall protein amount and 17 % of the membrane protein amount of the platelets is

The Integrin Receptor Family *		
Subunits		Ligands and Counterreceptors
β_1	α_1	collagens, laminin
	α_2	collagens, laminin
	α_3	fibronectin, laminin, collagens
	α_4	fibronectin, VCAM-1
	α_5	fibronectin
	α_6	laminin
	α_7	laminin
	α_8	fibronectin, osteopontin
	α_V	vitronectin, fibronectin
β_2	α_L	ICAM-1, ICAM-2
	α_M	C3b, fibrinogen, factor X, ICAM-1
	α_X	fibrinogen, C3b
β_3	α_{IIb}	fibrinogen, fibronectin, von Willebrand factor, vitronectin, thrombospondin
	α_V	vitronectin, fibrinogen, von Willebrand factor, thrombospondin, fibronectin, osteopontin, collagen
β_4	α_6	laminin, fibronectin type III
β_5	α_V	vitronectin
β_6	α_V	fibronectin
β_7	α_V	fibronectin, VCAM-1

Table 2.1. Some examples for $\alpha\beta$ combinations which form integrins and their counterreceptors. From [8].

$\alpha_{IIb}\beta_3$ [16]. Their abundance on platelets make them very accessible for purification (from outdated platelet donations.) Depending on the source, an intact platelet contains on average 40.000 to 100.000 integrin complexes [15], [17]. The average diameter of a platelet ranges from 1.5 to 3 μm .

The integrin $\alpha_{IIb}\beta_3$ exists as a dimer on platelets, and 1:1 stoichiometry is also preserved after purification in the presence of detergent. The α - subunit has a size of 136 kDa, the β - subunit 92 kDa. Figure 2.5 shows a surface shaded 3D density map of the integrin $\alpha_{IIb}\beta_3$.

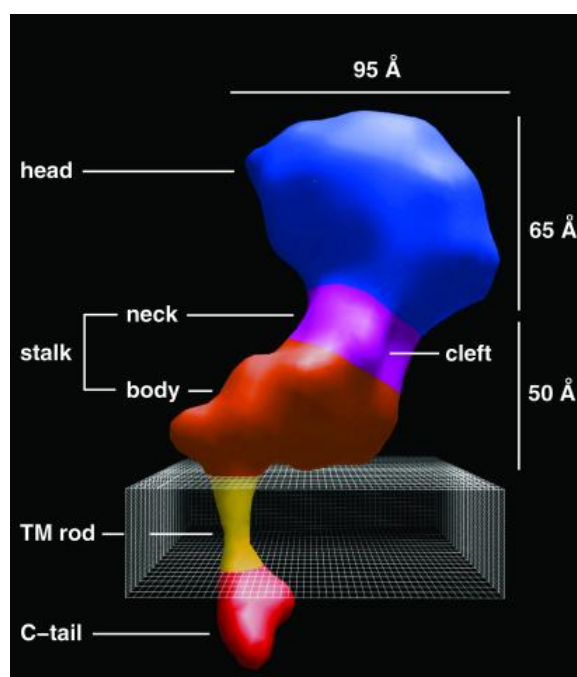


Figure 2.5. Surface-shaded 3D density map of the $\alpha_{IIb}\beta_3$ heterodimer at 2 nm resolution. The dimensions and domains are indicated. It is presumed that the cleft in the neck domain separates the α_{IIb} and β_3 subunits, and the larger lobe of the cytoplasmic domain corresponds to the C tail of the β_3 subunit which is twice the size of the α_{IIb} C tail. The model has been oriented so that the putative transmembrane rod is roughly perpendicular to the membrane (boxed area, 3 nm thick). From [18]

The integrin $\alpha_{IIb}\beta_3$ is essential for blood coagulation due to its ability to bind to RGD*-containing ligands in an activated state. However, the selective ligand recognition by RGD-binding integrins like $\alpha_{IIb}\beta_3$ is determined by additional sequence motifs in the recognition epitope in the structural framework of the ECM. The integrin $\alpha_{IIb}\beta_3$ specifically recognizes the RGD-motif of fibrinogen*, but also a non - RGD decapeptide sequence of the γ - chain of fibrinogen [19], [20].

Glanzmann's thrombasthenia demonstrates the important role of intact integrin $\alpha_{IIb}\beta_3$ on platelets. Patients with this rare hereditary bleeding disorder caused by a genetic defect have platelets less able to adhere to each other and to the underlying tissue of damaged blood vessel. As a result, platelets fail to form a plug at the site of an injury, and bleeding time is significantly prolonged.

B.1.1 Activation and Binding

The integrin $\alpha_{IIb}\beta_3$ is a Ca^{2+} -dependent complex *in vivo*. However, *in vitro* addition of Mn^{2+} or removal of Ca^{2+} strikingly increases (2-3 fold) ligand binding affinity and adhesiveness compared to adhesiveness in the presence of $\text{Mg}^{2+} + \text{Ca}^{2+}$ [21], [22]. Furthermore, it was shown that activation can be mimicked *in vitro* by cations such as Mn^{2+} or Mg^{2+} , whereas Ca^{2+} typically favors the inactive state [23]. The different effects of these cations are related to their differential abilities to induce the integrin to undergo structure changes involved in activation. An unusual feature compared to other adhesion molecules is that the activation (e.g. in integrins $\alpha_{IIb}\beta_3$ on platelets) happens on a short timescale of <1 s. [24]

In vivo, integrin $\alpha_{IIb}\beta_3$ binds soluble fibrinogen only after **platelet activation** (see section B.2.2) by antagonists like ATP or thrombin [25], whereas interaction with immobilized ligand can occur with nonactivated platelets [26]. *In vitro*, integrin $\alpha_{IIb}\beta_3$ can be fully activated, since soluble, monomeric fibrinogen exhibits the same binding characteristics as measured for $\alpha_{IIb}\beta_3$ on native platelets [27]. Binding of antibodies has been shown to change the affinity of integrins for various ligands [28], [29]. But because antibodies also were able to cluster the integrin molecules, the mechanism of activation remains unclear. Experiments with monovalent FAB (fragment antigen binding) fragments suggested that clustering was not necessary for activation [30], although this notion was later challenged by additional experiments indicating that clustering is essential for ligand binding [31]. The structural basis of the activation process remains the subject of lively discussion [13], [32], [33], [34], [35], [36].

The integrin $\alpha_{IIb}\beta_3$, reconstituted into a planar lipid bilayer [37], binds ligand via a two-step mechanism, comprised of an initial reversible and a subsequent irreversible step. Analysis of the binding kinetics with surface plasmon resonance and immobilized integrin molecules confirmed these observations [38]. The initial reversible complex, the result of a low-affinity interaction with an equilibrium dissociation constant $K_d = 155\text{-}180$ nM, is slowly converted into a more stable and irreversible complex which binds fibrinogen with higher affinity ($K_d = 20\text{-}70$ nM). This irreversible binding event was also observed in the physiological interaction between activated platelets and fibrinogen [27].

B.2 Examples of the Role of Integrin: Leukocytes and Platelets

The dynamic aspects of cell adhesion described briefly above underline the need to regulate cell adhesion receptors at the cell surface. Many different adhesion receptors among them the class of **integrins** are known to be subject to regulation, as they control complex and very dynamic processes (for example reorganization and differentiation during tissue development). Integrins are known to be regulated at several levels [39], [40].

Modulation of the affinity of the adhesion receptor for ligand (called affinity modulation) is a very important mechanism for the activation of platelet aggregation and is thought to underlie activation of leukocyte adhesion (figure 2.6C) which will be described below. Adhesive strengthening by the clustering of adhesion receptors or by cytoskeletal-dependent processes such as cell spreading (figure 2.6B) is known to be crucial for strong cell attachment, the control of cell growth, and cell motility. These regulatory changes occur either in response to intracellular events (hence, sometimes called inside-out signaling), as a result of EC ligand binding (often called post-receptor occupancy events), or in many instances from both. Some integrins are subject to multiple levels of regulation (see below).

B.2.1 Inflammation: Leukocyte Adhesion

Tissue damage or injury, characterized by redness, heat, swelling, and pain, causes a defense reaction of the affected tissue called inflammation. The inflammation reaction enables the host to localize and eliminate the irritant and repair the surrounding tissue. For the survival of the host, inflammation is therefore a necessary process. Leukocyte transmigration through endothelium* and accumulation at the site of injury is a major event in inflammation (see figure 2.7).

The leukocyte adhesion cascade is a sequence of adhesion and activation events. After extravasation of the leukocyte (movement out of the circulatory system toward the site of tissue damage or infection), the cell exerts its effects (localization, elimination of the irritant, tissue repair) on the inflamed site (see figure 2.7). The adhesion cascade includes at least five steps: 1) capture, 2) rolling, 3) slow rolling, 4) firm adhesion, and 5) transmigration. Each of these five steps appears to be necessary for effective leukocyte recruitment, because blocking any of the five can severely reduce leukocyte accumulation in the tissue.

The first contact of a leukocyte with the activated endothelium is called **capture** or tethering. Capture occurs after margination*, allowing leukocytes to move close to the endothelium and away from the central blood stream. During the inflammatory response endothelial activation is required to initiate capture.

P-selectin on endothelial cells is the primary adhesion molecule for capture

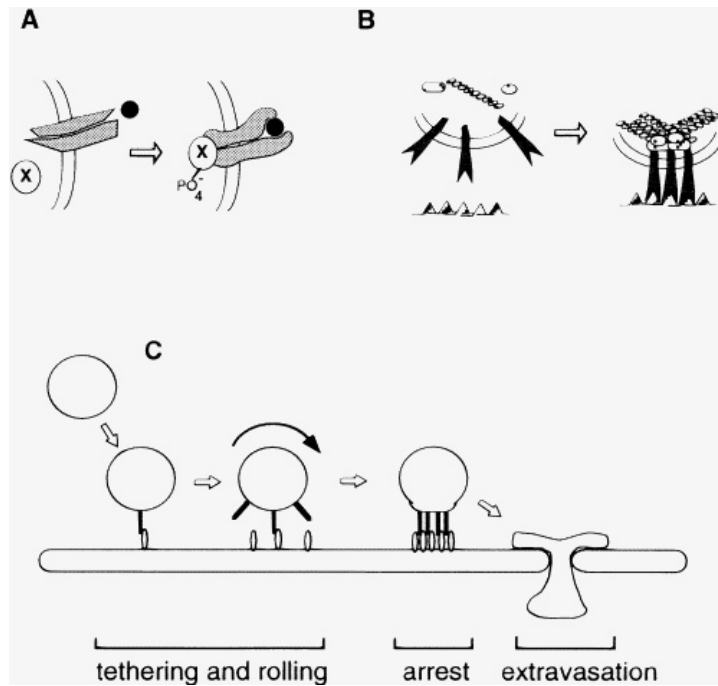


Figure 2.6. Mechanisms for regulating the binding activities of adhesion receptors (A) Affinity modulation. A conformational change in the EC adhesion-binding site occurs in response to intracellular signals. The conformational change is propagated from the cytoplasmic tail to the EC domain and is probably triggered by unknown cytoplasmic tail-binding proteins. (B) Adhesion receptor clustering and cytoskeletal interactions are associated with the development of extensive tight adhesion, such as spreading and focal adhesion* formation. (C) Different adhesive states exhibited by β_1 integrins during lymphocyte endothelial interactions under conditions of flow. In the inactivated state, the integrin can mediate tethering and rolling, which probably represents weaker attachments with high on and off rates. The same integrin can be activated to mediate arrest and tight binding. From [41].

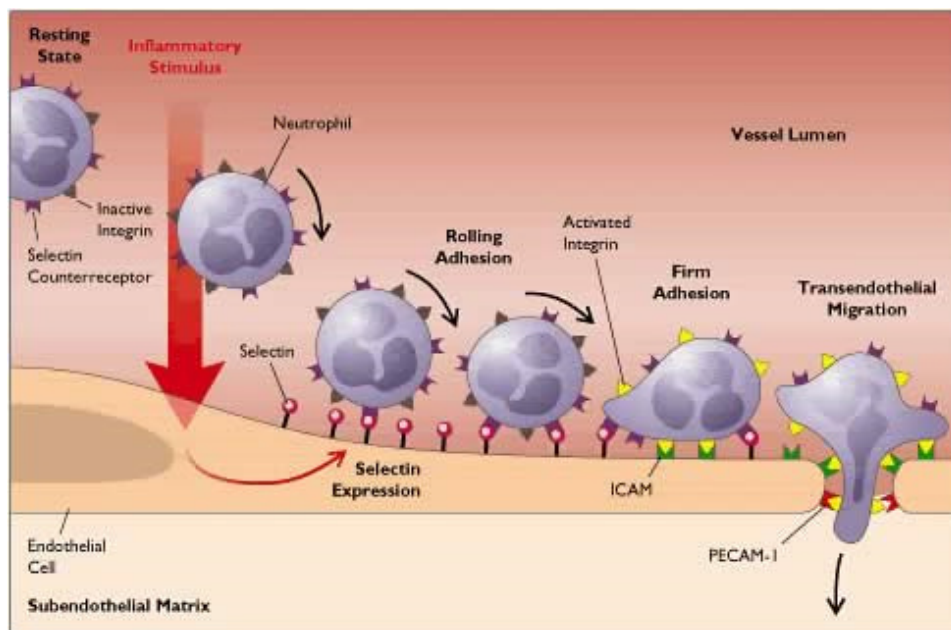


Figure 2.7. *Inflammation: The leukocyte adhesion cascade. From [42].*

and the initiation of rolling. The main leukocyte ligand for P-selectin is PSGL-1 (P-Selectin Glycoprotein Ligand-1).

After capture leukocytes transiently adhere to the venular endothelium and begin to roll. **Rolling** occurs at or below the velocity of freely flowing cells like erythrocytes in the same radial position in the same vessel. The selectin family of transmembrane adhesion receptors mediates this rolling process. P-selectin is the most important selectin involved in rolling and it can support both capture and rolling in the absence of L-selectin. Upon stimulation, P-selectin is rapidly surface-expressed on the venular endothelium, and it makes the endothelium "sticky" to leukocytes. PSGL-1 is constitutively expressed on all lymphocytes, monocytes, eosinophils, and neutrophils. During rolling, bonds are formed at the leading edge of the rolling cell and broken at the trailing edge.

L-selectin and E-selectin also take part in the rolling process. L-selectin is necessary for the normal inflammatory response in capturing leukocytes and initiating rolling. E-selectin is thought to be responsible for slow rolling interactions below $5 \mu\text{m/s}$ and possibly for the initiation of firm adhesion.

The key parameters in determining the success of the recruitment process as reflected in **firm adhesion** are 1.) the time that the leukocyte takes to pass through the microcirculation and 2.) the time during which it is in close proximity with the endothelium. The important role of leukocyte transit time

CHAPTER 2. CELL ADHESION MOLECULES AND INTEGRINS B

is dependant on chemokines, a class of cytokines*, that are presented on the endothelial surface and are likely to be accessible to a leukocyte as long as it rolls. Rolling leukocytes are likely to be activated by these surface-bound chemoattractants and through adhesion molecule-based signaling.

E-selectin also participates in the conversion of rolling to firm adhesion. In cytokine-induced inflammation, slow-rolling leukocytes do not stop abruptly, but show a gradual decrease of their rolling velocity before becoming adherent [43]. This deceleration is strictly dependent on CD18 integrins. Since rolling leukocytes show a graded elevation of intracellular free calcium as rolling slows, it appears that rolling leukocytes are partially activated before arrest. This process takes place on a times scale of one minute or more.

Leukocytes **migrate** across the resting endothelium if an exogenous chemoattractant is present. **Integrins** play an important role in this process, which has been termed "leukocyte driven" or chemotactic transmigration. The pathophysiological characteristic of established inflammatory transmigration is endothelial activation, an event requiring transcription and protein synthesis. As a result, adhesion molecules are upregulated. Upregulation means that they are activated and become more adhesive to their receptor, probably due to a conformational change of the protein.

Inflammatory mediators are produced and the endothelium secretes chemoattractants, all of which contribute to transmigration. The stimulus for endothelial activation in vivo is probably local production of cytokines and other inflammatory mediators released on tissue injury.

A number of adhesion molecules have been implicated in transmigration (for example PECAM-1, ICAM-1, VE-cadherin, CD11a/CD18 (LFA-1), IAP (CD47) and VLA-4 integrin), although the level of confidence in their actual involvement varies .

It has been recently shown that a single type of integrin can mediate all adhesive phases including the initial tethering and rolling. For example, $\alpha_4\beta_1$ (VLA4) mediates tethering and rolling on vascular cell adhesion molecule 1 (VCAM-1), an endothelial integrin ligand belonging to the immunoglobulin superfamily [44]. As expected, this integrin can also become activated to bring about arrest and tight adhesion. Thus, prior to activation, the integrin exhibits binding properties that support tethering and rolling.

The spectrum of behaviors exhibited by leukocytes under shear flow and in responses to physiological stimuli highlight the diversity of mechanism that cells can use to regulate the dynamics of adhesion. It is possible that similar mechanisms are relevant to the problems of cell motility and cell rearrangements in tissue morphogenesis. A comprehensive illustration of the processes involved in leukocyte rolling and capture emphasizing the inside-out and outside-in signaling is shown in figure 2.8.

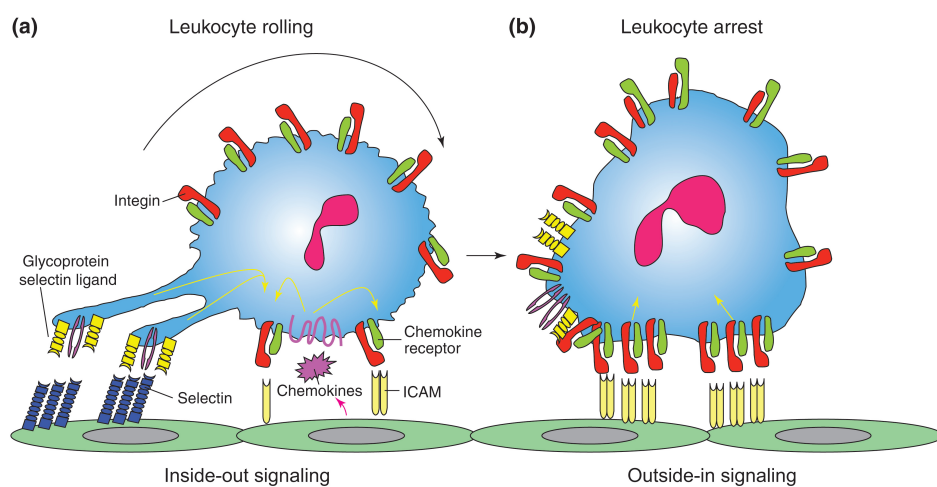


Figure 2.8. *Leukocyte rolling and capture* A) Selectin ligands on the leukocyte (yellow and purple) bind to selectins (blue) (homophilic* interaction), and low affinity integrins on the leukocyte (green) interact with ICAMs (pale yellow) on the endothelial surface facilitating cell tethering and rolling. Together with chemokines, this generates inside-out signals (yellow arrows) that shift the bound integrins to a high-affinity ligand-binding state. B) Leukocyte arrest is mediated by clustered high-affinity integrins (red) binding to ICAMs on the endothelial cells. These protein clusters can signal outside-in to affect functions such as cell polarization and migration. From [45].

B.2.2 Injury: Platelet Adhesion

At the site of injuries, the hemostatic plug closing the wound is initially formed through platelet adhesion. When injury occurs to the endothelium, platelets leave the blood vessel. Under the high shear flow stress at the site of injury they come in contact with and adhere to subendothelial tissues (see figure 2.9). Platelet adhesion is mediated by von Willebrand Factor (vWF)*, forming bridges or connections between the integrin $\alpha_{IIb}\beta_3$ and components on the subendothelium (mostly collagen fibers). Recently, it was shown that shear-induced unfolding of vWF triggers adhesion [46]. The process continues with attachment of platelet receptors to several adhesive proteins in the matrix of the connective tissue. Other platelets spread in a similar fashion, covering the collagen surface with a single layer of platelets.

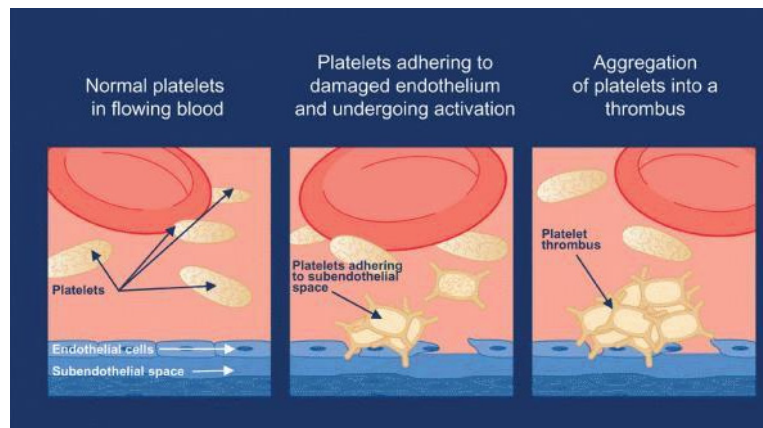


Figure 2.9. Platelet activation: A) Normal platelets flow in the blood stream without adhering. B) When the endothelial is damaged, platelets adhere and undergo activation. C) Platelets aggregate at the site of injury, forming a hemostatic plug. From [47].

When platelets adhere to collagen fibers in the subendothelium, a series of morphologic and functional changes known as activation occurs. Though not fully understood, platelet activation involves changes to platelet metabolic biochemistry, shape, surface receptors, and membrane phospholipid orientation. Platelets can be activated by many mechanisms. Most of the substances released by these cells (in particular adenosine diphosphate, serotonin, thromboxane and others) can, in an autocrine (released by the cell itself) and paracrine (released by a neighboring cell) fashion, further enhance platelet activation and aggregation. During activation of the coagulation cascade, thrombin is formed, which also markedly stimulates platelet activation. The activation of the the platelet surface molecule integrin $\alpha_{IIb}\beta_3$ is most important.

One of the biochemical changes that occurs within the platelet is an increase in internal calcium levels. When these levels reach a threshold a change in the shape of the platelet occurs. The activated platelet is transformed from a disc-shaped cell to a sphere with spiny projections called pseudopods. This change in shape results in an increase in the surface area available for biochemical reactions and increased chance of contact with other platelets. As they change shape platelets spread over the surface of the collagen to which they adhere, filling in the spaces between pseudopods.

During platelet activation, **integrin $\alpha_{IIb}\beta_3$ is activated**. Activation also causes a "change" in the membrane surface. This change enables fibrin-forming proteins (coagulation factors) to bind to the membrane.

The major platelet integrin $\alpha_{IIb}\beta_3$ is thought to be activated by affinity modulation [48], [49]. These proteins have been shown to undergo conformational changes during activation, as detected by antibody binding to activation-induced epitopes. Moreover, ligand binding studies indicate that these conformational changes are associated with changes in binding affinity. In fact, many integrins can be activated by the binding of certain monoclonal antibodies, presumably because the antibodies favor binding to the activated conformations of the molecules.

During platelet activation the integrin $\alpha_{IIb}\beta_3$ is converted to a high affinity state for binding to soluble fibrinogen or von Willebrand factor. This regulatory event is very important, of course, to prevent circulating platelets from aggregating in the absence of an appropriate hemostatic stimulus. $\alpha_{IIb}\beta_3$ can, however, mediate the adhesion of inactivated platelets to immobilized fibrinogen, presumably to facilitate recruitment of platelets to a preexisting hemostatic platelet plug. This demonstrates the important point that the inactivated $\alpha_{IIb}\beta_3$ is not truly an inactive or nonfunctional molecule, but rather that activation causes the conversion of a functional adhesion receptor to a different affinity state or binding specificity.

The molecular mechanisms underlying affinity modulation are only partially understood. Although activation by physiological signals must normally be initiated in the cytoplasm, the conformational change underlying the change in fibrinogen binding affinity can be triggered in isolated $\alpha_{IIb}\beta_3$ molecules by binding of activating antibodies. The propagation of the conformational change can occur at long range over the length of the molecule, since the activating antibodies bind to the "stalk" region near the membrane anchor, while the ligand-binding region of $\alpha_{IIb}\beta_3$ is known to reside at the distal "head" of the protein. This is consistent with the hypothesis that structural alterations in the integrin cytoplasmic tails are somehow propagated across the membrane to induce conformational changes at the ligand-binding sites. Indeed, there is abundant evidence that the cytoplasmic tails of $\alpha_{IIb}\beta_3$ and leukocyte β_2 integrins control the affinities or the adhesive states (or both) of the EC domains [50]. It is likely that specific cytoplasmic tail binding proteins are in-

CHAPTER 2. CELL ADHESION MOLECULES AND INTEGRINS C

volved in regulation, since overexpression of isolated cytoplasmic tail domains specifically inhibit activation of $\alpha_{IIb}\beta_3$ [51]. Thusfar, the identity of such a protein is unknown; it is not clear whether the known cytoplasmic plaque integrin-binding proteins, such as talin, α -actinin*, paxillin, or focal adhesion Tyr kinase* (FAK), or novel unknown proteins are required for regulating affinity.

Following platelet activation, formation of the primary hemostatic plug continues with platelet aggregation. This is the phase in which activated platelets become attached to one another. After the release of agonists such as adenosine diphosphate (ADP) by platelets and the injured vessels, platelets undergo a change in shape and integrin $\alpha_{IIb}\beta_3$ receptor sites become exposed. These changes enable the activated platelet to stick readily to those adhering to collagen. Aggregation takes place in two phases. In the primary phase, platelets attach loosely and, if the agonist stimulus is weak, they can be separated. The secondary phase requires a longer period of time in which platelets release their own ADP, further stimulating the aggregation process. When activation and primary adhesion have been achieved, platelets discharge their granule contents. Granule contents include ADP, adenosine triphosphate (ATP), serotonin, calcium, vWF, Factor V, and fibrinogen. The secreted substances further promote formation of the platelet plug by means of stimulating other platelets to adhere, aggregate and secrete.

C Cell Spreading and Reorganization in vitro

The goal of this thesis was to mimic integrin-mediated cell adhesion. Therefore, several steps involved in cell spreading are discussed below. Cell-cell or cell-ECM adhesion has been described in classical molecular biology textbooks for many years [8], [52]. However, the detailed underlying molecular processes which are responsible for signaling between the cell and its surrounding environment are often only poorly understood. Physical and biological in vitro experiments provide insights into the mechanisms of cell spreading and signaling. Some relevant results will be described here.

Recently it was shown by Cuvelier et al. that the very early steps of cell spreading dynamics follows a universal power-law behavior that is independent of adhesion molecules or substrate properties, and applies to various cell types [53]. The spreading dynamics of several cell types (wild-type and mutant) were studied after contact initiation and preceding cell polarization. The growth rate of adhesion zones was unaffected by the concentration of adhesive molecules on the substrate and was shown to be uniform among different cell types (see figure 2.10). The authors suggest that the complex mechanisms of cell spreading are ultimately limited by collective aspects of the cell's material properties, such as its geometry and thermodynamic and mechanical proper-

ties. During the early stages of adhesion, cells can be effectively modeled as a viscous adhesive cortical shell enclosing a less viscous interior. Thus their behavior appears to be independent of the complex biochemical interaction and signaling cascade that will set in shortly afterward. It was found that the contact radius follows an initial diffusive regime summarized by the scaling law $R \sim t^{\frac{1}{2}}$ before slowing down to a sub-diffusive behavior, $R \sim t^{\frac{1}{4}}$.

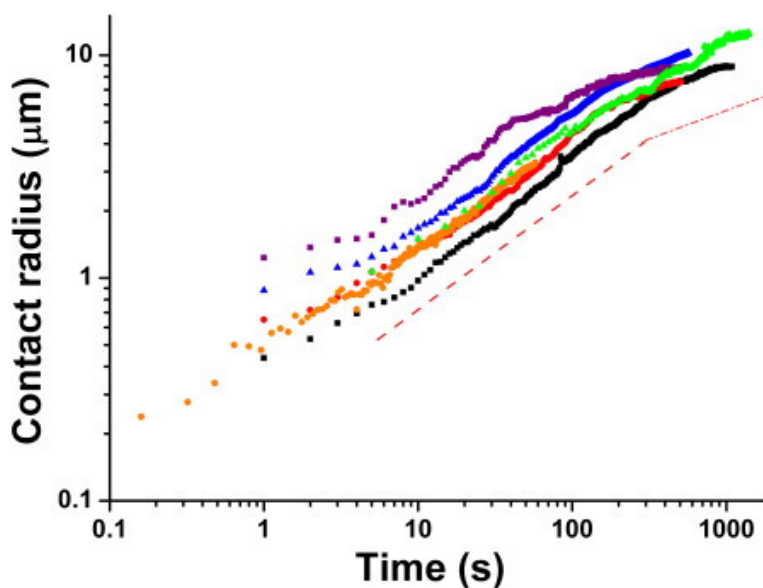


Figure 2.10. *The growth of adhesive patches during early stages of spreading exhibits a universal power law that is independent of cell type, substrate, and adhesion receptors. The following cells are shown: black square: HeLa cell/fibronectin (1 mg/μl) substrate, green triangle: E-cadherin S180 cell/E-cadherin substrate, red circle: Cdc42DN S180 cell/fibronectin substrate, purple square: nocodazol-treated HeLa cell/fibronectin substrate, blue triangle: HeLa cell/polylysine substrate, and orange circle: biotinylated red blood cell/streptavidin. From [53].*

Shortly after this first contact between the cell and the underlying substrate mimicking the ECM, a complex, tightly regulated process switches on, which further controls the cell spreading. Depending on the chemical and physical properties of the substrate, the cell responds with spreading, proliferation, differentiation or apoptosis. The cell attaches to the ECM, and regulates the adhesion-mediated signaling via focal adhesions and similar structures. Through cytoplasmic anchor proteins, integrin receptors link the actin* cytoskeleton to the ECM, usually through RGD-motifs. Integrins are found to cluster in focal adhesions. Complex pathways are involved, including protein activation or conformation change of focal adhesion molecules as well as proteins of the cytoplasm and the ECM. Focal adhesion signaling can occur in

CHAPTER 2. CELL ADHESION MOLECULES AND INTEGRINS C

both directions (inside-out and outside-in) and influences these proteins, the reorganization of actin cytoskeleton on the inside of the cell and the adhesion molecules on the outside of the cell.

In order to understand these complex biochemical processes, one approach is to develop substrates which can be functionalized and controlled on micro- or nanometer scale in order to mimic efficiently the ECM. The group of J. Spatz. developed a substrate consisting of a nanopattern of gold dots functionalized with an RGD-motif that is recognized by numerous integrins [54] (see figure 2.11). For geometric reasons, the size of a functionalized gold dot allows the binding of only one integrin. Using such precise tools, they found a universal length scale for integrin clustering and activation that is within the range of 58 to 73 nm. A separation larger than 73 nm between adhesive dots results in limited cell attachment and spreading, and dramatically reduces the formation of focal adhesions and actin stress fibers. Separations smaller than 73 nm between the dots allowed effective adhesion. This result can not be attributed to an insufficient number of ligands but rather to the restriction of integrin clustering. The same length scale was found for several cell types indicating a universal spacing for effective adhesion mediated by integrins. Recent developments permit transfer of the gold patterns to almost any type of soft surface [55], thereby allowing considerable control of surface properties which are known to have an impact on cellular responses [56]. Furthermore, nanopatterns have been prepared on non-planar surfaces such as curved glass fibers with varying diameters. The universal scale length of the range of 58 to 73 nm has been confirmed in such experiments [57].

Integrins are associated via their cytoplasmic domains with a protein complex including vinculin, talin, paxillin, tensin and many other proteins (for a schematic description see [58]) which are all involved in the dynamic association with actin filaments. Integrins are found in several complex structures including dot-like complexes ($0.5 - 1 \mu\text{m}$) at the edge of lamellipodia known as focal complexes and elongated ($3 - 10 \mu\text{m}$ in length) streak-like structures (focal contacts or focal adhesions) which are associated with actin- and myosin-containing stress fibers. The bundles of actin filaments lie adjacent to the adhesion complexes, oriented parallel to the membrane [8]. The actin is connected to an extensive trans-cellular network. This network can contract with the help of myosin motor proteins during processes such as cell motion or cell division.

The detailed molecular architecture of focal contacts remains unknown, although several interaction pathways have been identified.

Focal complexes are thought to be the precursors for most focal contacts. Their formation is induced by the small Rho-family* G-protein Rac [59], [60]. It is possible that the attachment to the ECM induces binding of activated Rac to the membrane [61], where it can stimulate actin polymerization and

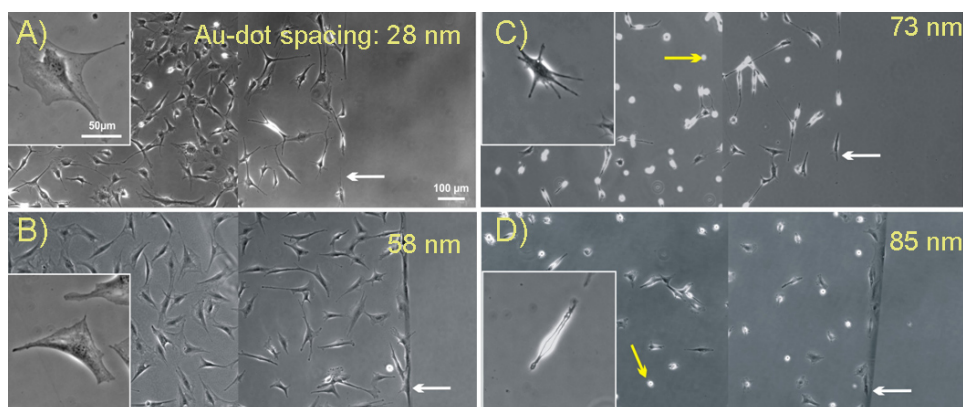


Figure 2.11. Gold nanostructures functionalized with an RGD-motif that is recognized by integrins on the cell surface. The distance between two gold dots varies, 28 nm, 58 nm, 73 nm, 85 nm. No nanostructures are located on the right side of the images. Cells mark the borderline (white arrows) between nanostructured areas and areas entirely passivated by PEG. Yellow arrows indicated quiescent cells. The insets show magnification of a typical cell attached to the indicated surface. From [54].

branching*. Rapid actin flow in turn promotes integrin clustering. There are three partners of Rac mediating these effects: 1) type PIP 5-kinase α which catalyzes PIP_2 production, leading to uncapping of actin filaments, 2) IRSp53 protein activating WAVE/Scar, which in turn activates actin filament nucleation via Arp2/3 complex and 3) the serine-threonine kinase PAK. These details are mentioned above to illustrate the multitude of proteins involved in the process and underline the complexity of focal complex formation. However they shall not be commented upon in further depth. Transformation of focal complexes into focal contacts requires the activation of Rho, but the mechanism is still poorly understood [60], [62]. Active Rho has multiple targets which modulate some functions of the actin cytoskeleton, but it appears that the combined action of just two of them, ROCK and mDia1 is sufficient to substitute for Rho in the process of focal contact assembly [63] (see figure 2.12).

The main function of the ROCK-dependent pathway is to activate myosin-II-driven cell contractility through the augmentation of phosphorylation* of myosin II regulatory light chain (MLC). The level of MLC phosphorylation is controlled by balanced phosphorylation by MLC kinase (MLCK) and dephosphorylation by MLC phosphatase (MLCP). This induces a conformational change of ROCK. In addition, ROCK can directly activate contractility by phosphorylating MLC just like MLCK [64], [65]. The mDia1-dependent pathway includes activation of actin polymerization (both locally, in the proximity of the growing focal contact, and globally, in distal regions) and possibly target-

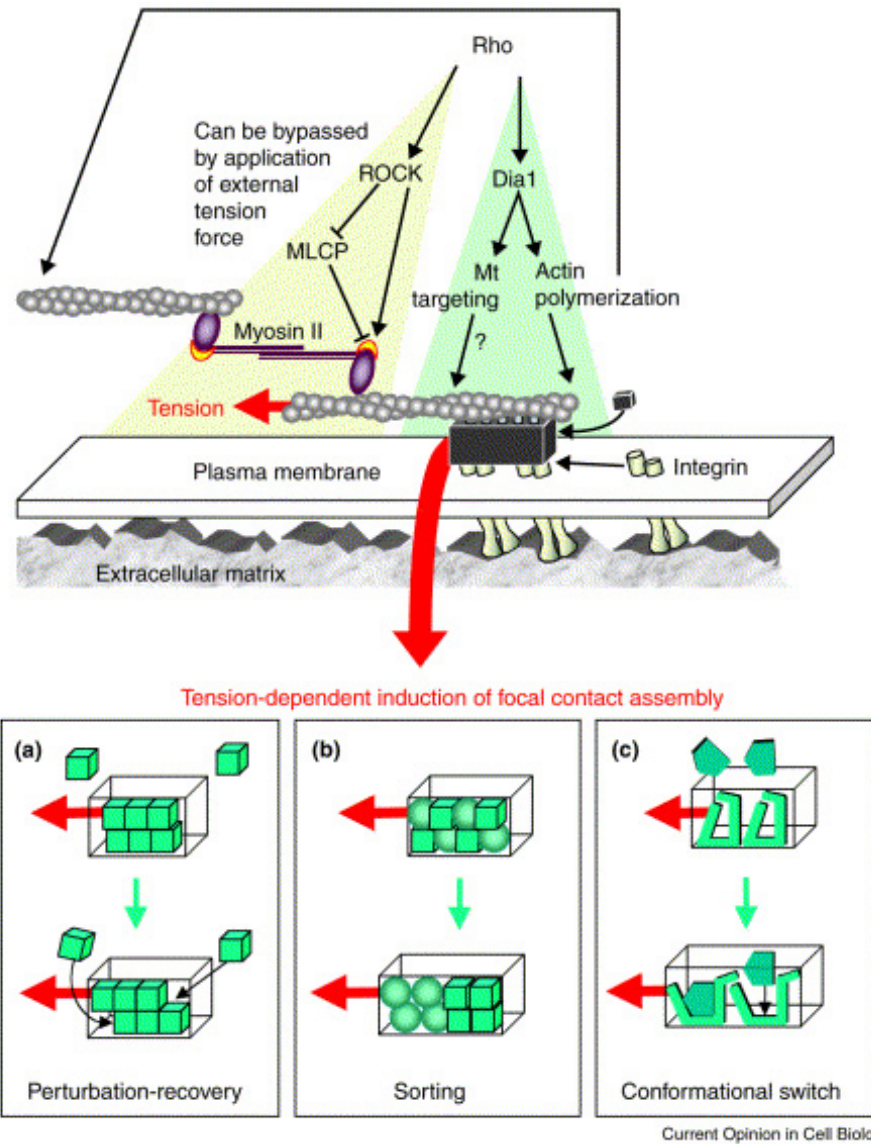


Figure 2.12. *Rho-dependent growth of focal contacts. Rho induces formation of the focal contacts by activating two essential pathways: ROCK dependent (shown in yellow) and mDia1-dependent (shown in green). IN the presence of active mDia1, the application of a force triggers the growth of the focal contact (black box). Three hypothetical models are suggested: a) The "perturbation-recovery" model, b) the "sorting" model, c) the "conformational switch" model. ROCK and mDia1 are sufficient to substitute for Rho in the process of focal contact assembly. All are explained further in the text. Mt=microtubule. From [63].*

ing of microtubules and subsequent microtubule-dependent delivery of certain components. As for ROCK, this includes a conformational change, activating the protein for interaction with various downstream targets (see figure 2.12). Other possible targets for Dia action are microtubules. Thus it is possible that microtubule-dependent processes regulated by Dia might affect focal contact assembly [66].

The formation and stability of focal contacts depends strictly on myosin-II-driven contractility. For example, chemical inhibitors of MLC phosphorylation suppress focal contact and stress fiber formation. This sensitivity to myosin II inhibition is a characteristic feature of focal contacts discriminating them from other types of actin-integrin adhesion complexes.

The phosphorylation pathway for ROCK can be bypassed if a force is applied externally, if mDia1 is active, application of tension force triggers the growth of the focal contact [67]. The molecular mechanism of the force-induced focal contact growth is not clear, but experiments with force application by micropipette showed that force-dependent regulation of focal contact assembly is a local process. In non-motile cells it was shown that the size of the contact depends on the force applied to it, and the force per unit area remained constant (about $5 \text{ nN}/\mu\text{m}^2$). Microtubule ends are often inserted into regions of leading lamella where focal contact formation occurs [68], [69]. Disruption of microtubules increases tension and promotes focal contact growth, whereas growth of microtubules in the proximity of contact sites induces local relaxation of tension and suppresses focal contact growth [69], [70]. Thus a correlation between applied tension and protein recruitment seems to exist.

Three hypothetical models suggesting how such a "mechanosensory switch" might work to induce focal contact growth are depicted in the bottom part of figure 2.12. (a) The "perturbation-recovery" model suggests that force applied to focal contacts perturbs the integrity of the protein meshwork associated with the adhesion sites, creating spaces that can accommodate new subunits. (b) According to the "sorting" model, force might selectively displace some components from the adhesion site, changing their molecular microenvironment. (c) The "conformational switch" model suggests that force applied to specific adhesion-associated molecules might induce conformational changes, leading to their transition into "active conformation". Several detailed theoretical models have been proposed [71], [72].

D Glossary

Some terms that might not be familiar to the reader are briefly explained in this glossary.

CHAPTER 2. CELL ADHESION MOLECULES AND INTEGRINS D

α actinin:

Actinin is a microfilament-binding protein. α -Actinin is necessary for the attachment of actin filaments to the z-line membrane (the borders that separate and link sarcomeres (see below) within a muscle) in muscle cells. The functional protein is an anti-parallel dimer, which cross-links the thin filaments in adjacent sarcomeres (A sarcomere is the basic unit of a muscle's cross-striated myofibril (cylindrical organelles, found within muscle cells)), and therefore coordinates contractions between sarcomeres in the horizontal axis.

Actin Filaments:

Actin is an abundant protein that forms filaments in all eukaryotic cells. It is the major constituent of the cytoskeleton of all eukaryotic cells and part of the contractile apparatus of skeletal muscle.

Branching morphogenesis:

Branching morphogenesis is the process in which epithelium invades embryonic connective tissue (mesenchyme) to form a composite organ (the lung is a typical example). Complex dynamic interactions between mesenchymal and epithelial tissues are involved. ECM turnover and cell proliferation occur at the tips of the buds, while ECM accumulates in the clefts where there is little growth.

Cnidaria Cnidaria is a phylum containing some 9,000 species of animals found exclusively in aquatic, mostly marine, environments. Despite their early appearance in the evolutionary history of animals and their simple morphology, the modern forms are genetically sophisticated and biochemically complex. There are four main classes of Cnidaria: 1) Class Anthozoa (anemones, corals, etc.), 2) Class Scyphozoa (jellyfish), 3) Class Cubozoa (box jellies), and 4) Class Hydrozoa (Obelia, Aequorea, Portuguese Man o' War, etc.)

Cytokine:

Cytokines are proteins and peptides that are used for cell signaling. They are produced by animal and plant cells to communicate with other cells. Cytokines act on cytokine receptors located on the surface of cells. The cytokine family consists mainly of small, water-soluble proteins and glycoproteins (proteins with an added sugar chain) with a mass of between 8 and 30 kDa.

Cytoplasmic plaque proteins:

Cell adhesion receptors associate with cytoplasmic plaque or peripheral membrane proteins. Cytoplasmic plaque proteins serve to link the adhesion systems to the cytoskeleton, to regulate the functions of the adhesion molecules, and to transduce signals initiated at the cell surface by the adhesion receptors.

Endothelium:

The endothelium is the thin layer of cells that line the interior surface of blood

and lymph vessels, the heart, and the serous cavities of the body to form an interface between circulating blood in the lumen and the rest of the vessel wall. Endothelial cells line the entire circulatory system, from the heart to the smallest capillary. These cells reduce the friction from the blood flow allowing the fluid to be pumped further.

Epithelium:

The epithelium is a tissue composed of layers of cells that line the cavities and surfaces of structures throughout the body. It is also the type of tissue of which many glands are formed. Epithelium lines both the outside (skin) and the inside cavities and lumen of bodies such as intestine. The outermost layer of our skin is composed of dead, stratified, squamous, keratinized epithelial cells.

Gap junctions:

Gap junctions are connections between two cells' cytoplasm. The Gap junction allows ions and small molecules to pass from one cell to the other.

Fibrinogen:

Fibrinogen (also called factor I) is a 340 kDa soluble plasma glycoprotein synthesised in the liver. It contains the tripeptide sequence RGD (Arginine-Glycine-Aspartic acid), which is a ligand to integrin. In its natural form, fibrinogen can form bridges between platelets, by binding to their GpIIb/IIIa surface membrane proteins ($\alpha_{IIb}\beta_3$).

Focal adhesion:

A type of anchoring cell junction, forming a small region on the surface of a cell that is anchored to the extracellular matrix. Attachment is mediated by transmembrane proteins, such as integrins, which are then linked through other proteins to actin filaments in the cytoplasm. Focal adhesion sites serve as signaling platforms to transduce information from the outside to the inside of the cell and vice versa.

Homophilic, heterophilic interaction: In this chapter, these terms describe interactions between adhesion molecules. **Homophilic** interaction exists between two molecules of the same type (e.g. cadherins) while **heterophilic** interaction means that the adhesion molecule recognizes a different molecule (e.g. integrin-RGD-interaction).

Intermediate Filament:

The intermediate filament is a fibrous protein filament (about 10 nm in diameter) that forms ropelike networks in animal cells. It is one of the three most prominent types of cytoskeleton filaments, besides actin filaments and microtubules.

Leukocyte:

White blood cells, or leukocytes, are cells of the immune system defending the body against both infectious disease and foreign materials. Several different types of leukocytes exist, but they are all produced and derived from multipotent cells in the bone marrow known as a hematopoietic stem cells. Leukocytes are found throughout the body including the blood and lymphatic system.

Margination:

Margination is the process in which free-flowing leukocytes exit the central blood stream and initiate leukocyte-endothelial interactions by close mechanical contact. The underlying mechanisms of margination involve the interaction of leukocytes with erythrocytes flowing in the same microvessel, whereby deformed erythrocytes push leukocytes to a marginating position due to their smaller cross section and higher flow velocity.

Mesenchyme:

Immature, unspecialized form of connective tissue in animals, consisting of cells embedded in a thin extracellular matrix. Mesenchymal tissue is made up of clusters of cells grouped together but not closely adherent to one another. The cells compose a highly hydrated gel, rich in salts, fluid, and fibres, known as the **interstitial matrix**.

Phosphorylation:

Phosphorylation is the addition of a phosphate (PO_4) group to a protein molecule or a small molecule. Another way to define it would be the introduction of a phosphate group into an organic molecule. It is often involved in the regulation of proteins or small molecules.

Platelet:

Platelets are fragments of megakaryocyte cells that do not contain a nucleus (but do contain actin filaments and other cell organella). They are released from the bone marrow into the blood. They assist in blood clotting by adhering to other platelets and to damaged epithelium – also called blood platelet, thrombocyte.

Protein kinase:

A protein kinase is a kinase enzyme that modifies other proteins by chemically adding phosphate groups to them (phosphorylation). For example, serine/threonine protein kinases phosphorylate the OH group of serine or threonine (which have similar sidechains).

RGD

RGD is a tripeptide, RGD standing for the aminoacid sequence arginine-glycine-aspartic acid in the one letter code system.

Rho family The Rho family of GTPases is a family of small (~21 kDa) signaling G proteins (more specifically GTPases), and is a subfamily of the Ras superfamily. The members of the Rho GTPase family have been shown to regulate many aspects of intracellular actin dynamics, and are found in all eukaryotic organisms as well as in yeasts and some plants. Described as "molecular switches", the Rho family members play roles in cell proliferation, apoptosis, cell division, gene expression, and several other common cellular functions

von Willebrand factor:

Von Willebrand factor is a blood glycoprotein involved in hemostasis (blood coagulation).

A Biological Membranes: Components and Characteristics

Cellular membranes have diverse functions in the different regions and in the different organelles of a cell. The cell as well as its internal compartments are enclosed by membranes. These isolate the interior from the outside both passively due to limited permeability of the membrane (to ions or small molecules) and actively via certain transmembrane proteins which consume energy (e.g. to maintain ion gradients). Cellular membranes contain a variety of lipids, proteins and carbohydrates, and can be linked to the cytoskeleton (see figure 3.1).

However, despite of their various functions and constituents, all biological membranes consist of **a lipid bilayer** [8].

Typical compositions of biological membranes can be found in figure 3.2.

A.1 Lipids and Organisation in Lipid Bilayers

A lipid is an amphiphilic molecule, which has a polar hydrophilic head and one or several non-polar hydrophobic tails with a typical length of 2-3 nm. The surface of the hydrophilic head is about 0.5 nm^2 .

the major types of lipids that predominate in eukaryotic membranes are the phosphoglycerides (or phospholipids), the sphingolipids, and cholesterol (see figure 3.3).

The lipid molecules self-assembled because of their amphiphilic character. They usually assemble into a bilayer made of two lipid leaflets. In the lipid

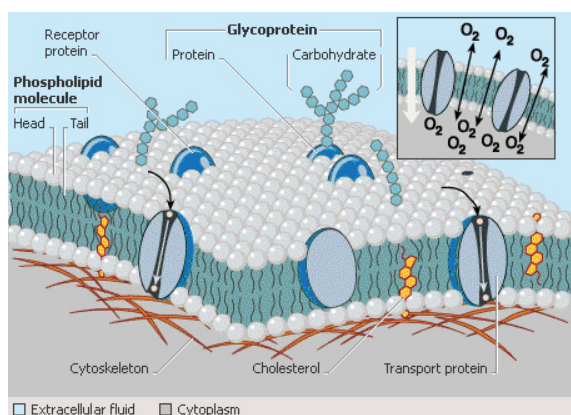


Figure 3.1. Schematic representation of a cell membrane and its principal components: the lipid bilayer and some transmembrane proteins. From [73].

Membranes	Protein	Lipid	Carbohydrate
Plasma membranes:			
red blood cells	49	43	8
liver cells	54	36	10
amoeba	54	42	4
myelin	18	79	3
Nuclear envelope	66	32	2
Endoplasmic reticulum	62	27	10
Golgi complex	64	26	10
Mitochondrion			
outer membrane	55	45	trace
inner membrane	78	22	---
Chloroplast inner membrane	70	30	---

Figure 3.2. The weight composition of various membranes found in cells by protein, lipid, and carbohydrate content. From [8]

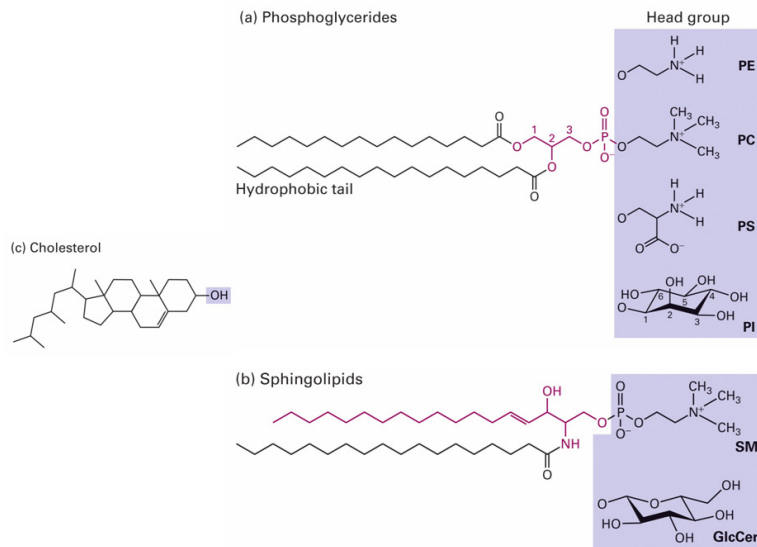


Figure 3.3. Major types of lipids in biological membranes a) phosphoglycerides (or phospholipids), b) the sphingolipids, and c) cholesterol. From [8].

bilayer, the hydrophilic heads are oriented towards the aqueous solution and shield the hydrophobic chains from water.

The geometry of the molecule is the crucial factor in determining the local shape of the membrane. For instance, quasi-cylindrical molecules prefer to arrange in flat or curved bilayers, whereas cone-like molecules form spherical micelles [74]. The lipid membrane in a biological system can be considered as a two-dimensional fluid that is held together mainly by non-covalent interactions [75]. The lipids are arranged in a bilayer with a thickness of 5-7 nm.

In contrast to the artificial membranes studied in this work, biological membranes are asymmetric, meaning the lipid distribution in the two leaflets of the membrane is not the same [76], [77]. Sphingolipids, for example, are always found on the outside of the plasma membrane. In human erythrocytes, as well as in many other cell types, lipids with PC heads are essentially found on the outer membrane of the cell, whereas the inner membrane also contains PE and PS lipids. Since PS lipids are negatively charged, a significant charge difference between the two leaflets can exist.

Above their transition temperature T_c , the lipid molecules can move freely in the bilayer, and the bilayer has the property of a two dimensional fluid (see figure 3.4). The lateral diffusion coefficient is very fast in a monolayer: typically, the diffusion coefficient is of the order of a few $\mu\text{m}^2/\text{s}$ in a membrane in the disordered liquid phase. Lipid diffusion coefficients have been measured with the help of several techniques including NMR [78], single-particle tracking [79], Fluorescence Recovery After Photobleaching (FRAP) [80], and Fluorescence Correlation Spectroscopy (FCS) [81]. The diffusion coefficients depend

on the nature of the lipids [75].

The lipid molecules can also rotate around their own axis, with a rotational diffusion coefficient of the order of $D \sim 10^8 \text{ s}^{-1}$ [82]. Since the polar head group has to pass through the non-polar region in the center of the lipid bilayer, transversal diffusion (flip-flop or transfer between the two lipid leaflets) occurs only at a rate of $D \sim 10^{-8} \text{ s}^{-1}$ for phospholipids and is a very improbable process in a model membrane [8]. It is faster for lysolipids (with only one chain) [75]. In biological membranes, this process can be accelerated by proteins present in the membrane, called flippases [77].

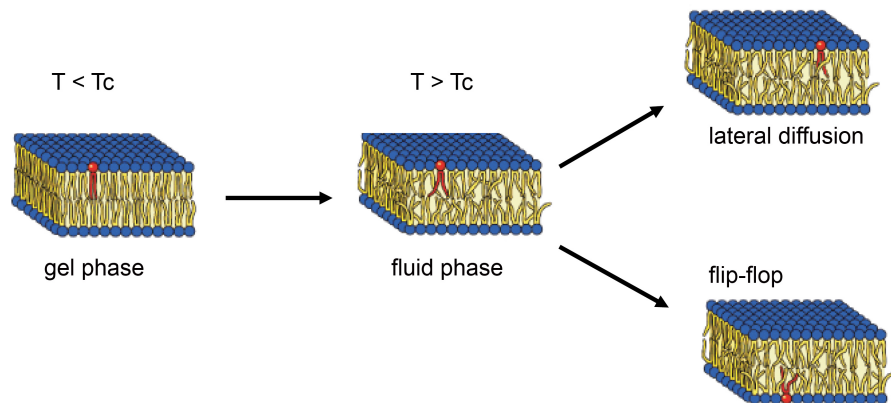


Figure 3.4. Lipid behavior in a bilayer depending on the temperature. T_c is the transition temperature of the lipids. From [75].

A lipid membrane has variable permeability, meaning that some molecules can diffuse freely through the membrane even in the absence of specialized proteins like transporters, channels or pumps. Molecules diffuse at differing rates depending upon their ability to enter the hydrophobic interior of the bilayer. The bilayer is virtually impermeable to large molecules, relatively impermeable to charged ions such as Na^+ and K^+ , (for phosphatidylcholine bilayers: Na^+ : $\Lambda_P = 10^{-14} \frac{\text{m}}{\text{s}}$, K^+ : $\Lambda_P = 3 \times 10^{-14} \frac{\text{m}}{\text{s}}$) [83] but quite permeable to lipid soluble low molecular weight molecules such as ethanol. The layer is much more permeable to water molecules: for an EPC membrane, a permeability coefficient $\Lambda = 40 \times 10^{-6} \frac{\text{m}}{\text{s}}$ was measured [84], [85]. Because free edges of a membrane have a very high free energy, any breaks or ruptures of the cell membrane can spontaneously be repaired provided that the pore radius does not exceed a critical value [86].

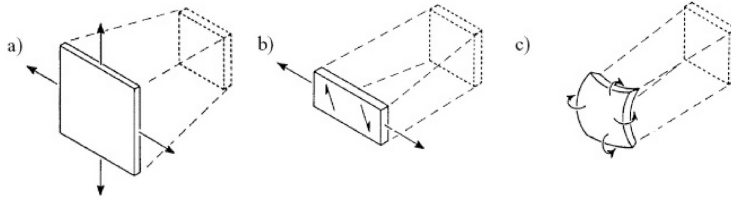


Figure 3.5. The three possible deformation modes: a) compression-extension mode, b) shear mode, and c) curvature mode. From [91].

A.2 Mechanical Properties of Lipid bilayers

On a mesoscopic level, membranes can be described by the geometric properties and physics of elastic fluids. Classical descriptions have been given by Canham [87], Helfrich [88], and Evans [89] and [90]. The elastic energy results from three deformation modes - a) compression-extension mode, b) shear mode, and c) curvature mode. All deformations can be formed from a combination of these three basic deformations (see figure 3.5).

- The first type, the compression-extension mode, is an elastic deformation characterized by a compression modulus, χ (in J/m²) (see figure 3.5a). The associated energy per surface, H_{ext} , depends quadratically on the variation of the surface area,

$$H_{ext} = \frac{1}{2}\chi \left(\frac{\Delta A}{A} \right)^2 \quad (3.1)$$

where χ is the compression modulus (about 0.2 J /m² for vesicles, as estimated by micropipette aspiration technique [92], [93]) and $\Delta A/A$ is the relative variation of the surface area associated with the deformation. This variation never exceeds 8 % as beyond this point, pores open and the vesicle lyses at a critical tension around 10⁻³N/m. Built-in tensio-active molecules can slow down the lysis of the membrane [94].

- The shear mode is a deformation in the plane of the membrane at constant area (see figure 3.5b). The associated energy per unit surface area, H_{shear} , is obtained from Hooke's law and gives:

$$H_{shear} = \frac{1}{2}\mu(\lambda^2 + \lambda^{-2} - 2) \quad (3.2)$$

where $\lambda = (L_0 + \Delta L)/L_0$ is the lateral extension rate and μ the shear modulus. In the case of fluid membranes, the energy is negligible: with constant area, the lipids can diffuse freely and do not resist shearing. This deformation becomes important however in the case of more complex systems such as when the membrane is associated with the cytoskeleton.

- The curvature term combines all deformations which are not in the plane of the membrane or which do not occur on a constant surface (see figure 3.5c). It is the dominant deformation of the three:

$$H_{curv} = \frac{1}{2}\kappa(c_1 + c_2 + c_0)^2 + \kappa_G c_1 c_2 \quad (3.3)$$

where $c_1 = 1/R_1$, and $c_2 = 1/R_2$ are the principal curvatures of the membrane, and R_1, R_2 are the two principal radii in perpendicular direction. c_0 is the spontaneous curvature; that is the local curvature of the membrane without mechanical constraint. This term corresponds to a possible asymmetry of the membrane due to differences in the lipid composition in the two leaflets of the membrane. The product $c_1 c_2$ is the Gaussian curvature. The Gauss-Bonnet theorem shows that the integrated product over the surface of the vesicle is a topological invariant. Deformations applied to the surface of the vesicle generally do not alter the topology. Therefore, the term characterized by the Gaussian curvature κ_G is frequently neglected. κ is the bending rigidity modulus of the curvature. It depends on the temperature and the composition of the membrane. Numerous techniques to measure this modulus exist, such as by Fourier analysis of the vesicle shape [95], [96], [97], [98]. Other methods study the elastic behavior of the membrane after mechanical deformation by electrical [99] or magnetic fields [100], or by micropipette aspiration [90], [92], [101]. For vesicles made of the same lipid type, some dispersion of the bending rigidities is observed. This can be explained by the sensitivity of different techniques to different wavelength ranges. For instance, contour analysis is sensitive to larger length-scales than micropipette aspiration.

The energy associated with the integrated curvature over the whole membrane is given by the following hamiltonian [87], [88]:

$$H = \oint H_{curv} dA = \oint \left(\frac{1}{2}\kappa(c_1 + c_2 + c_0)^2 \right) dA \quad (3.4)$$

To a first approximation, this hamiltonian is sufficient to describe membrane deformations and additional corrections were later added to take into account the asymmetry of the bilayer and its thickness. However, this hamiltonian does not allow for the existence of structure within a bilayer, nor the fact that two monolayers can have two different surface areas, which could induce an additional curvature [102]. These effects will be discussed below together with the area difference elasticity model (ADE) [103].

Some typical values for the compression modulus, the shear modulus, and the curvature modulus are given in table 3.1 and compared to standard materials.

Material	Compression Modulus χ (J/m ²)	Shear Modulus μ (J/m ²)	Curvature Modulus κ (J)
Steel	100	100	10^{-15}
Poly-Ethylene	5	5	5×10^{-17}
Red blood cell	10^{-5}	6×10^{-6}	$2-70 \times 10^{-20}$
Lipid bilayer	$100-700 \times 10^{-3}$	0	$4-40 \times 10^{-20}$

Table 3.1. Some typical values for the compression modulus, the shear modulus, and the curvature modulus. From [104].

- The lateral tension, σ , is an intensive parameter associated with the vesicle area, $\sigma = \partial F / \partial A$ where F is the free energy of the membrane. Two regimes can be defined as a function of the extension: the *enthalpic* and the *entropic* regime. The enthalpic regime corresponds to large extensions whereas the entropic regime corresponds to small extensions. In the enthalpic regime, the membrane has already undergone a large extension, and so further stretching increases the average surface area per lipid. When the membrane is expanded, its area increases with ΔA , which increases the elastic term, H_{ext} . If the shear mode is neglected, the elastic energy per surface area can be written as follows:

$$H = H_{ext} + H_{curv} = \frac{1}{2}\chi \left(\frac{\Delta A}{A} \right)^2 + \frac{1}{2}\kappa (c_1 + c_2 + c_0)^2 + \kappa_G c_1 c_2 \quad (3.5)$$

The total elastic energy of the membrane is therefore HA . The tension is then

$$\sigma = \frac{\delta(HA)}{\delta(\Delta A)} \quad (3.6)$$

For a flat membrane, this gives

$$\sigma = \chi \frac{\Delta A}{A} \quad (3.7)$$

The origin of this tension is *enthalpic*. However, this equation is only valid for tensed membranes (figure 3.6b), when vesicle area and projected area are equal (figure 3.6c).

Experimentally, vesicles are often not tensed and can then undergo large thermal fluctuations because of their low bending modulus κ (see figure 3.6a). In aqueous solution, collisions with water molecules make the membrane fluctuate around an average position. These fluctuations (in the case of red blood cells) have been observed already about a century

ago by T. Browicz [105] and called flickering and have been explained by F. Brochard and J.-F. Lennon in terms of thermal fluctuation in 1975 [106]. Hence, the observed area (e.g. by microscopy) does not correspond to the real surface of the vesicle.

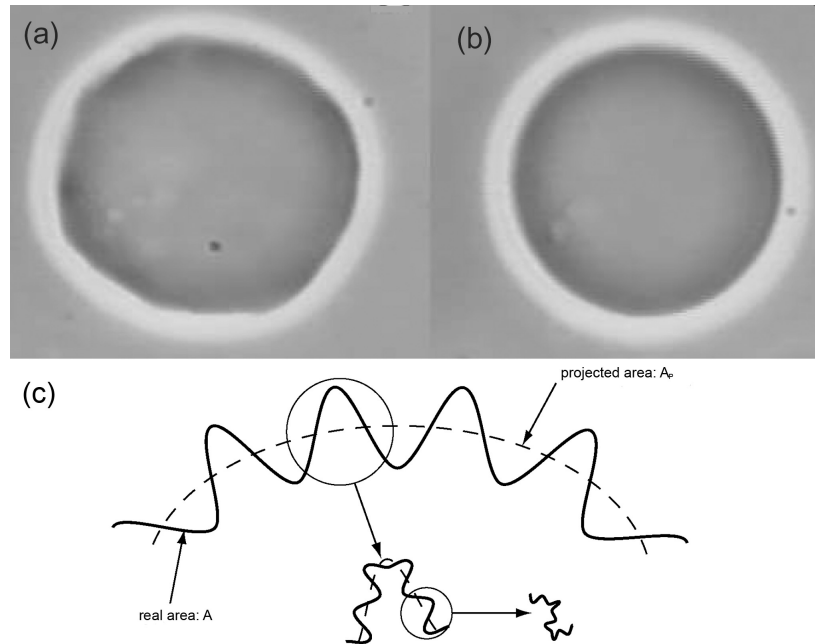


Figure 3.6. *GUV under light microscope A) Floppy vesicle: The membrane fluctuations are optically visible. B) Tensed vesicle: The vesicle appears perfectly round and no fluctuations are optically detected. C) Schematic representation of a fluctuating membrane. A represents the real area, while A_P represents the projected area. From [107]*

In this case, an increase in the projected membrane area can be achieved by reducing the size of membrane fluctuations. However, reducing the membrane fluctuations decreases the entropy of the membrane and so it increases the free energy of the membrane. If the real surface area of the vesicle doesn't change, the surface energy density can be described with the help of a Lagrange multiplier associated with the area dA , corresponding to the local membrane tension. Since the surface is fluid, the tension is homogeneous along the membrane, and this multiplier is just the global tension of the membrane, σ . The total energy is then given by:

$$H = \frac{1}{2}\kappa(c_1 + c_2 + c_0)^2 + \sigma \left(\frac{\Delta A}{A} \right) \quad (3.8)$$

The tension of the membrane can then be calculated by applying the energy equipartition theorem to give :

$$\sigma = \sigma_0 \exp\left(\frac{-8\pi\kappa}{k_B T} \left(\frac{A - A_P}{A}\right)\right) \quad (3.9)$$

where σ_0 is the membrane tension related to a microscopic "cut-off" associated with the lipid size [108], k_B is the Boltzmann constant and T the temperature. This tension has an entropic origin. The higher the difference between projected and real area is, the more the vesicle fluctuates and the lower its membrane tension is.

In the general case, it was shown experimentally [92] and theoretically [109] that the area excess $\Delta A/A$ can be expressed as a function of the membrane tension by adding the two contributions of the fluctuations (entropic, low stretching regime) and the elasticity (enthalpic, high stretching form). The variation of the surface excess area $\frac{\Delta A}{A}$ between an initial state with zero tension and a final state with a tension σ , $\Delta\alpha = \alpha^0 - \alpha$, results from both the flattening of membrane fluctuations and the extension of the membrane [92]:

$$\Delta\alpha = \frac{k_B T}{8\pi\kappa} \ln(1 + cA\sigma) + \frac{\sigma}{\chi} \quad (3.10)$$

where $c = \frac{1}{24\pi}$ and A is the area of the vesicle (if we suppose that area and volume remain constant). This expression frequently used to describe micropipette experiments in which the vesicle is aspirated into a micropipette to produce a controlled membrane tension [90]. At low tension ($\sigma < 10^{-5}$ N/m) only the first term is taken into account. This technique was used to measure the bending rigidity of membranes [92], [101] (see also figure 3.7). Tension generally ranges between 10^{-8} to 10^{-3} N/m and the bending rigidity around 10^{-20} to 10^{-19} J. Using the data given in table 3.1, it can be shown that surface area excess cannot exceed 8 % for these tensions.

J.-B. Fournier et al. [109] were able to give a definition for tension which accounts for the entropic and enthalpic terms without simply adding the two. For this, they distinguished between the microscopic area (which was here called the real area A), the area L^2 (before called the projected area), and the optical area $A^<$ which corresponds to the area visible in the microscope, and differs from the simple projected area L^2 (see figure 3.8).

The "coarse-graining" is related to the resolution limit of an optical microscope. The tension is then an intensive variable associated with

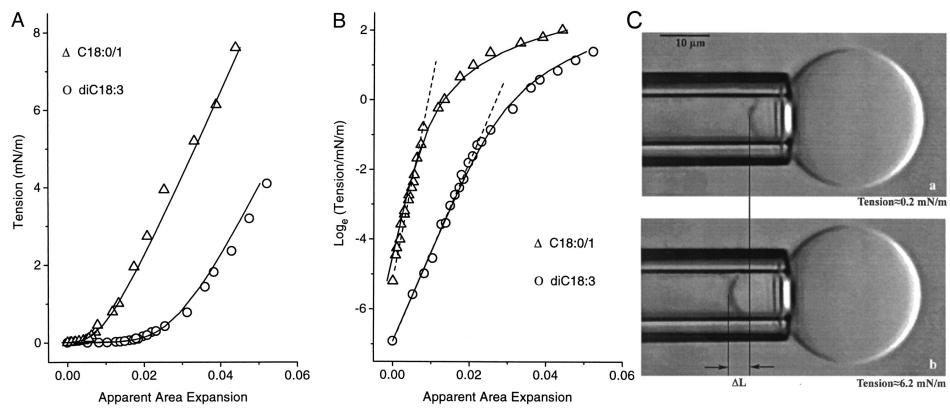


Figure 3.7. Examples of apparent area expansion measured over tensions ranging from 0.001 to 8 mN/m for two vesicles of different lipid composition. A) Linear plot of tension versus apparent area expansion. Using equation 3.10 the characteristic parameters of the membrane (membrane rigidity κ and compressibility modulus χ) can be obtained. (B) Semilog plot of tension versus apparent area expansion. Slopes of the linear fits (dashed lines) in the first part of the curve applied to the range of very low tensions yield the elastic bending modulus κ . The second part of the curve corresponds to the enthalpic regime. C) Video micrograph of a vesicle area expansion test. (a) The vesicle at low tension. (b) The vesicle at high tension. The change in projection length ΔL_p is proportional to the change in apparent surface area ΔA . From [92]

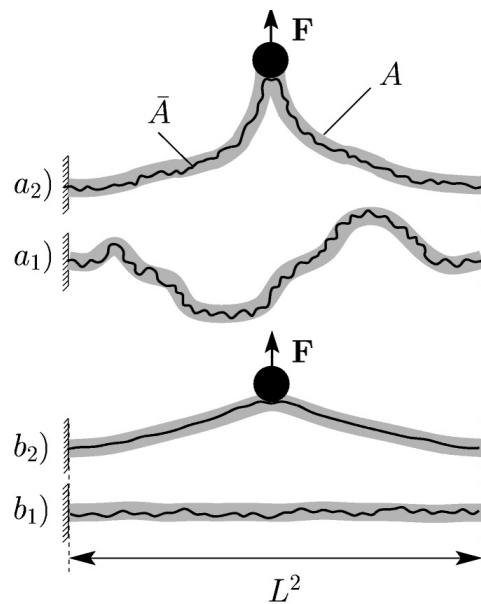


Figure 3.8. Membranes with a microscopic area A and an optically visible area $A^<$, attached to a fixed frame of area L^2 . The effective, optically measurable tension of an initially "flat" membrane (b_1), can be further increased by an external perturbation (b_2). Similarly, an initially "floppy" membrane (a_1) can be externally driven into a tense regime (a_2). From [109].

the observed area $A^<$, and not to A . In the non-tensed state, the tension can be written as

$$\sigma = \sigma_0 \exp\left(-\frac{8\pi\kappa}{k_B T} \left(\frac{A - A^<}{L^2}\right)\right) \quad (3.11)$$

which can be compared to equation 3.9. In the general case, the tension-surface area excess relation has the same form as equation 3.10.

A.3 Vesicle Shapes

The shape of vesicles can be obtained by minimizing their energy. Even though a spherical form often corresponds to the equilibrium shape, other shapes can be found by varying the characteristic parameters of the vesicle - volume, surface, spontaneous curvature, or temperature [75]. The obtained phase diagrams depend on the complexity of the model that is used:

- The simplest model consists only of minimizing the curvature energy of the vesicle (given by the Canham-Helfrich hamiltonian, equation 3.4):
 - * Without spontaneous curvature ($c_0 = 0$), the equilibrium shape only depend on the dimensionless volume $v = V / (\frac{4}{3} \pi R^3)$, where R represents the radius of the vesicle. Ellipsoids, prolate dumbbells, oblate discocyte, stomatocytes, and finally spheres are obtained when increasing v .
 - * When including the spontaneous curvature ($c_0 \neq 0$), the phase diagram depends on the dimensionless volume and the dimensionless curvature c_R . In the case of $c_0 > 0$, pear-shaped vesicles are observed, while $c_0 < 0$ favors the oblate shape.

However, this simple model is not capable of describing all experimentally observed shapes, for example the starfish shape [110]. One reason is that the model does not take into account the asymmetry between the two leaflets.

- The Area Difference Elasticity model (ADE model) includes this asymmetry between the two leaflets. When the membrane is positively curved, the inner leaflet is more compressed than the external leaflet. Therefore, the two leaflets do not have the same total surface. This asymmetry is also present if the two leaflets do not contain the same number of lipids. The ADE model takes this into account via a non local elasticity model $\bar{\kappa}$ [102], [112]. A term for the energy which represents the stretching of one bilayer relative

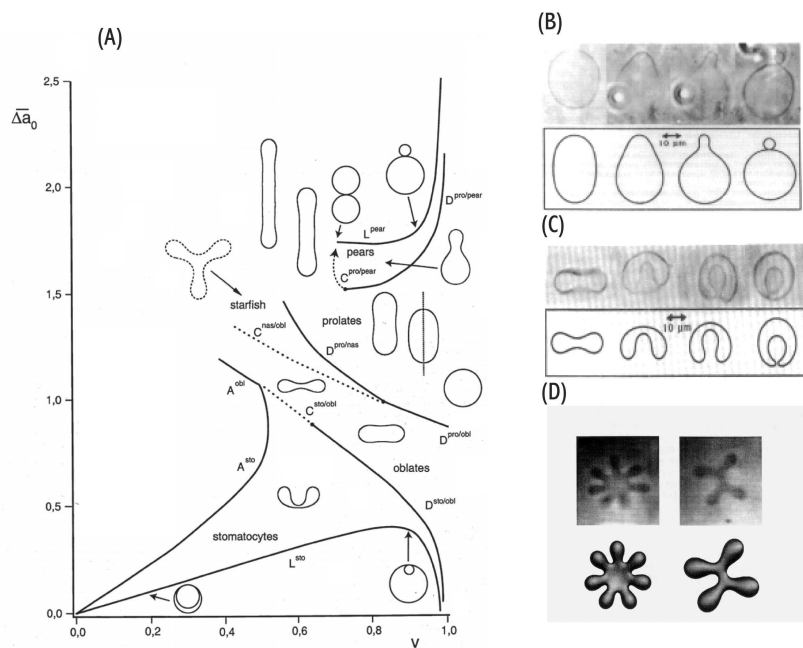


Figure 3.9. A) Phase diagram of possible vesicle shapes in the ADE model, parameters are the reduced volume v and the area difference between the two leaflets $\overline{\Delta a_0}$. From [103]. B) Transition prolate - pear during, increasing temperature leads to the formation of a daughter vesicle. From [111]. C) Transition discocyte-stomatocyte through increasing temperature, From [111] D) Starfish-shaped vesicle. From [110].

to the other is added to the Canham-Helfrich hamiltonian [113] (equation 3.4 without spontaneous curvature nor gaussian curvature). This is a non local term (it results from integration over the whole surface), unlike the other terms listed above (extension, curvature, etc.) The total energy integrated over the whole surface of the vesicle can be written as:

$$H = \oint \left(\frac{1}{2} \kappa (c_1 + c_2)^2 \right) dA + \frac{\pi \bar{\kappa}}{2Ad^2} (M - M_0)^2 \quad (3.12)$$

where d is the bilayer thickness, M is the area difference between the two leaflets ($M = d \oint (c_1 + c_2) dA$) and M_0 is the area difference only due to the different number of lipids in the two leaflets. M_0 (integrated quantity over the whole vesicle) reflects the asymmetry between the two leaflets and illustrates the tendency of the membrane to curve but is different from the spontaneous curvature which is a local factor. An estimation for non-local curvature is given by $\bar{\kappa} = 4\kappa/\pi$, corresponding to typically 10-100 $k_B T$ [114], [115].

The obtained phase diagram depends on three parameters: 1) the dimensionless volume $v = \frac{V}{(4/3)\pi(A/4\pi)^{3/2}}$ which describes the swelling state of the vesicle. The denominator would be the volume of the vesicle if it were spherical. 2) the ratio between the two elastic moduli $q = \bar{\kappa}/\kappa$ [116]. 3) The dimensionless area difference between the two leaflets: $\Delta a_0 = \frac{M_0}{8\pi d(A/4\pi)^{3/2}}$. Figure 3.9A shows a phase diagram resulting from varying only parameters, v and $\overline{\Delta a_0}$. $\overline{\Delta a_0}$ is the dimensionless effective area between the two leaflets given by the sum of spontaneous and area difference curvature ($\overline{\Delta a_0} = \Delta a_0 + \frac{1}{2\pi q} c_0$).

Some transitions have been studied in more detail, such as the prolate-oblate transition [116], [117], [118] or the prolate-pear transition [119]. The latter explains theoretically the experimental results of J. Käs and E. Sackmann who had observed the formation of a daughter vesicle from an initial mother vesicle by increasing the temperature progressively [120] (see figure 3.9B). It is also possible to vary the other parameters to observe the variation of the shape of the vesicle. An osmolarity difference between the outer and the inner medium of the vesicle is commonly used to vary the ratio between surface and volume. Formation of daughter vesicles and fission is also observed in this case [121]. It is also possible to add lipids to one of the leaflets [122]. The average forms obtained theoretically are all axisymmetrical, but it is also possible to obtain non-axisymmetrical shapes numerically with the help of the ADE

model or the curvature model including a spontaneous curvature term which is non-zero [117], [123]. If the vesicles are sufficiently deflated, the ADE model allows starfish shaped vesicles (see figure 3.9D). The different models have been summarized by U. Seifert in [113].

B Model Membranes: Giant Unilamellar Vesicles

Because of the complexity of biological membranes, simplified and reproducible model systems composed only of lipids were developed to permit comparison to theory. Various examples for model membrane systems exist (for a review see [124]) including the lamellar phase (bilayer stacks), suspended bilayers (including black lipid film), supported lipid bilayers and vesicles. Different types of vesicles exist, which can be distinguished according to their size:

- **SUVs** are small unilamellar vesicles with a size smaller than 100 nm in diameter.
- **LUVs** are large unilamellar vesicles with a size ranging between 100 nm and 1 μm .
- **GUVs** are giant unilamellar vesicles with a size larger than 1 μm .

GUVs were used in this project and will therefore be described in detail.

B.1 General Characteristics

GUVs are composed of a single bilayer, and have, most frequently, a spherical topology. In general, they have a diameter ranging between 5 and 100 μm and as their size is similar to cells, they can be observed with optical microscope (see figure 3.10). Because they consist of a single lipid bilayer, they are therefore called unilamellar (in comparison with multilamellar vesicles, also called "onions"). Since the end of the 1970s, GUVs have been used to study the physical properties of lipid bilayers.

B.2 Standard Methods for the Preparation of GUVs

Giant Unilamellar Vesicles (GUVs) can be prepared using several techniques. Only the first technique presented here was used in this study.

B.2.1 Electroformation

In the presence of an AC electric field, the swelling of lipid bilayers in aqueous sugar solution yields GUVs with a homogeneous population of spherical and

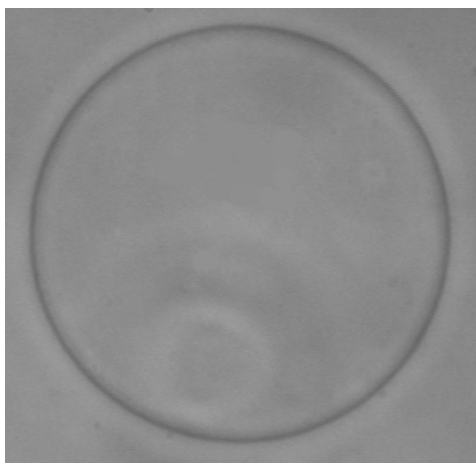


Figure 3.10. A defect-free vesicle of about $20\ \mu\text{m}$ in diameter, unilamellar and spherical, observed in phase-contrast microscopy.

unilamellar vesicles [125], [126]. A theoretical explanation for the growth process of giant unilamellar vesicles has been developed [127]. For the application of the AC electric field, two types of electrodes can be used. Either the lipid solution is applied to conductive wire [125], [128], or to glass slides coated with a thin conductive indium tin oxide layer (ITO) [126].

During application of the voltage a progressive increase in size of the vesicles can be observed [figure 3.11]. Classically, the typical AC electric field is $\sim 1\ \text{V}$ (RMS), applied for 3hrs with a frequency of 10 Hz.

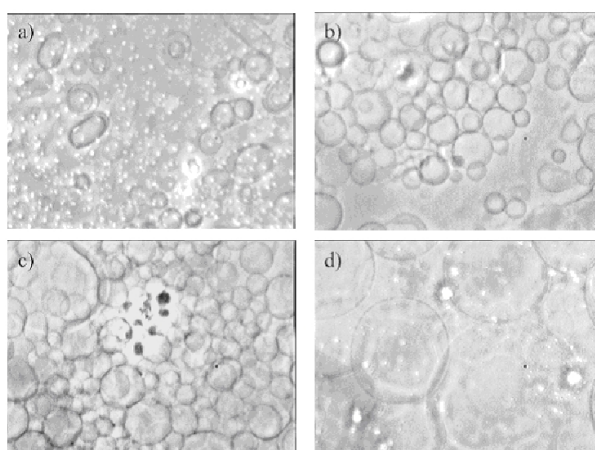


Figure 3.11. Growth of giant unilamellar vesicles with electroformation a) after 30 minutes, b) after 55 minutes, c) after 95 minutes, d) after 120 minutes, phase contrast microscopy. From [129].

The small vesicles that are initially formed fuse to reach a maximum di-

iameter of about 30 to 60 μm [figure 3.11]. A drawback of this method is that it only tolerates very low ion concentrations ($< 3 \text{ mM}$). However, recent publications show that ionic strength similar to cellular concentrations can be used, if high frequency voltage is applied during GUV preparation (see below) [128], [130]. Another possibility is the use a spontaneous swelling technique (see below). Our detailed experimental protocol is described in appendix D.

B.2.2 Spontaneous Swelling

Swelling a film of lipids for long time ($\sim 10\text{-}20 \text{ h}$) in aqueous solution typically produces giant vesicles. This technique allows encapsulating of a variety of objects (e.g. polymers, proteins, or magnetic colloids). However, the size of the encapsulated objects is limited to a maximum of 10 nm in diameter. Various swelling solutions with different conditions can be used, and the method works with pure water as well as with physiological buffer with high salt content. However, reproducibility is a problem. The size distribution is often large and multi-lamellar objects can form. Typically only a few percent ($\sim 5 \%$) of unilamellar vesicles are obtained with this technique [131], the majority being multilamellar.

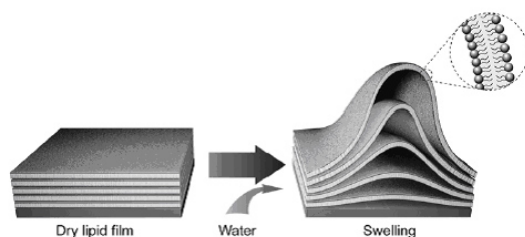


Figure 3.12. Swelling of the lipid bilayer in presence of water. From [132].

B.2.3 Electroinjection Technique

A fairly recent development to obtain giant unilamellar vesicles is the electroinjection technique. The method is a combination of spontaneous swelling and electroporation. This was initially developed by O. Orwar's group [133] and later by Nicolas Biais [134]. A lipid film is dried and re-hydrated in the desired buffer solution. After a few minutes a combination of multi- and unilamellar vesicles develops (see figure 3.13).

A thin graphite electrode is placed onto the membrane. A second electrode is positioned in a micropipette against the vesicle and a short electric pulse is applied to open a pore. The pore closes rapidly, and the membrane seals around the micropipette. Buffer can then be injected with the help of the micropipette. The unilamellar liposome is filled with more buffer solution until

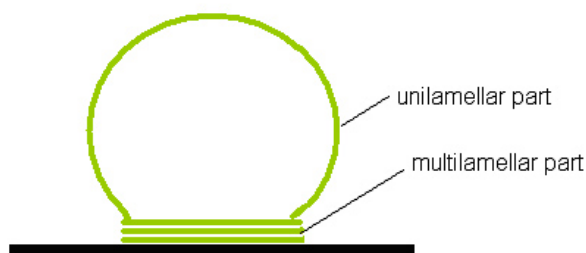


Figure 3.13. Typical vesicle prepared by the electroinjection method, consisting of a multilamellar and a unilamellar part.

the desired size is reached. This is possible since the liposome can recruit more lipids from the multilamellar reservoir. The obtained giant vesicle is detached from the multilamellar part with the help of the carbon electrode. With this technique the size of the giant unilamellar vesicles as well as their content can be controlled. Buffer of larger osmolarity or larger objects (size of a few microns) can be introduced in these vesicles [134].

B.3 Functionalized Giant Unilamellar Vesicles

Giant Unilamellar Vesicles are useful models for biological systems, since they consist of a closed lipid bilayer with a diameter of a biological cell. They can be further functionalized by using functionalized lipids or by introducing charges [135]. Formation of macroscopic domains has been observed [figure 3.14] [136], [137], and different lipids or lipid mixtures with different functions can be used [138]. Phase separation in GUVs has been extensively studied during the recent years stimulated by the observation of small lipid domains in the cell membrane ("rafts").

Proteins can also be incorporated [3], [139] or attached to the membrane [140] to mimic the properties of biological systems. In addition, cytoskeleton elements can be incorporated inside the GUVs to further resemble biological cells [141], [142] (see also figure 3.15). Microtubules trapped inside giant unilamellar vesicles produce shapes reminiscent of living cells, and their mechanical properties can be compared to biological systems (figure 3.15) [143], [144]. Giant unilamellar vesicles are very well adapted for adhesion studies. Cell adhesion molecules (CAMs) can be fixed to a substrate, their (simpler) receptors can be incorporated in the membrane and the adhesion of the membrane on the functionalized substrate can then be studied. This system represents a significant step towards mimicking the process of cell-extracellular matrix adhesion [140], [145].

The electroinjection method and the spontaneous swelling method described above are powerful methods to fill GUVs with the desired content. Recently, other techniques have been developed including one based on an adaption of

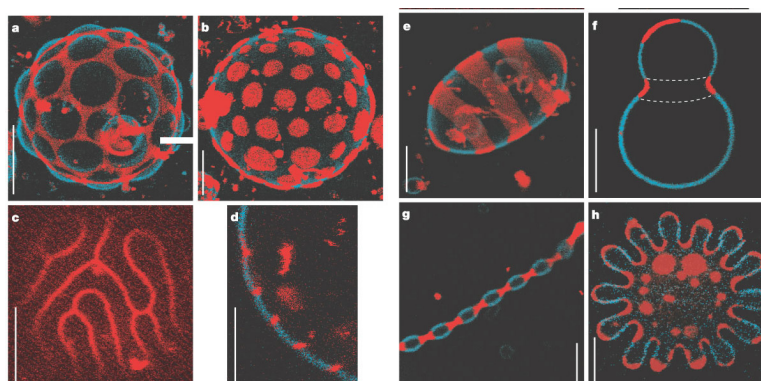


Figure 3.14. Giant unilamellar vesicle containing sphingomyelin, cholesterol, and DOPC, as well as two dyes showing lipid phase separation; all images are superpositions of red and blue channels, except c (red channel only). d, Scale bars, 5 μm . From [136].

the Langmuir-Blodgett technique using emulsions [146], [147], and another one using microfluidic jetting [148]. These methods also allow for a control of the internal content of the GUV.

The ultimate goal of all of these techniques is to create a simplified model cell.



Figure 3.15. Bending microtubules inside of lipid vesicles. From [143].

B.3.1 Methods to Reconstitute Membrane Proteins into GUVs

The cell membrane is a highly complex structure containing transmembrane proteins. In order to reproduce this complex structure in a model system, the group of Patricia Bassereau developed a new and general method for the reconstitution of membrane proteins into GUVs [3]. They systematically analyzed the reconstitution of two radically different membrane proteins - the sarcoplasmic reticulum Ca^{2+} -ATPase and the H^+ pump bacteriorhodopsin. The first step of the method involves a detergent-mediated reconstitution of solubilized membrane proteins into proteoliposomes of 0.1-0.2 μm in size. In a second step, these preformed proteoliposomes are partially dried under con-

trolled humidity followed, in a third step, by electroswelling of the partially dried film to give GUVs. The reconstitution process was further characterized by analyzing protein incorporation and biological activity. Both membrane proteins have been homogeneously incorporated into GUVs at lipid/protein ratios ranging from 5 to 40 (w/w). After reconstitution, both proteins retained their biological activity as demonstrated by H^+ or Ca^{2+} pumping driven by bacteriorhodopsin or Ca^{2+} -ATPase, respectively.

Doeven et al. [139] have shown that adding small amounts of sucrose to the proteolipid mix prevented denaturation of proteins (four distinct membrane proteins were tested) during the dehydration process. The amount of sucrose was optimized (minimal amount of 0.02 g sucrose/g lipid) such that the proteins retained 100 % biological activity. The proteoliposomes could be dried in vacuum without losing membrane activity. Proteo-GUVs were then reproducibly obtained. Furthermore, they showed that the presence of negatively charged lipids (DOPS) helped to reconstitute the membrane proteins into liposomes. This result was later used in our project.

B.3.2 GUV Formation under Physiological Conditions

As mentioned above, the classical electroformation only works in ionic strength up to a few mM, which is far below the physiological level. However, in order to come closer to biomimetic systems, GUVs have to be prepared in buffers with high ionic strength. With the help of the protocol developed in the Bagatolli lab [128], this problem was recently solved. It was shown that GUVs can be prepared either from native membranes or lipid mixtures at physiological strength using an electroformation method that uses 500 Hz AC fields and conductive wires. Additionally, for GUVs composed of native membranes, the membrane proteins and glycosphingolipids preserved their natural orientation after electroformation.

Bagatolli et al. suggested that it might be important to revisit a variety of experiments performed with GUVs under low or no salt conditions. Model systems containing proteins are likely to be affected by the amount of salt present in the solution. This might also apply to the results presented in our study.

C Interactions between Membranes

Two types of interaction between objects (here lipid bilayers) in aqueous solution will be discussed in this section:

1. The non-specific or generic interactions
2. The specific interactions

While non-specific interactions are always present between two objects (here lipid bilayers) in aqueous solution, specific interactions depend on the presence of special molecules which recognize each other (often compared to a lock and a key). These specific interactions correspond to the specific recognition of two proteins located on the two facing lipid bilayers.

C.1 Generic Interactions

Non-specific interactions are mediated by the generic intermolecular forces, such as van der Waals forces, electrostatic forces, solvation and steric forces.

C.1.1 Van der Waals forces

The van der Waals interaction energy per unit area between two planar surfaces at distance D is attractive and is given by [74]

$$W(D) = -\frac{A}{12\pi D^2} \quad (3.13)$$

where A is the non-retarded Hamaker-constant.

The van der Waals contribution between bilayers is fairly weak and has an effective range of less than 15 nm. Beyond this range Van der Waals forces are too weak to be significance.

C.1.2 Repulsive Forces

For interacting bilayers there can be up to four different types of repulsive steric forces that are independent of the solvent [74]. These are the undulation force, the peristaltic force, the protrusion force and the steric overlap force between surface-anchored polymer brushes or head groups. The two most important are the undulation force [88] and the steric overlap force. Only the undulation force is expected to be long-range; the other three forces will decay rapidly to zero beyond a certain distance roughly equal to the lengths of the lipid molecules. However, at small separations below about 2 nm, the protrusion and head group overlap forces are expected to dominate the undulation repulsion. The role of electrostatic interactions in the adhesion of biological systems is complex. Charges are present in physiological solutions in form of ions as well as on surfaces (surface proteins, lipids,...). Theoretical details can be found in [149].

C.2 Specific Adhesion

Even though generic forces are always present, cells do not always stick to each other which is essential for cell migration or flow (e. g. in the blood stream). A system is therefore necessary that can prevent cells from sticking

to each other through generic interactions, but allow them to adhere to each other when needed. The first system to *prevent non-specific interactions* is the hyaluronic acid present on the outer cell membrane. The hyaluronic acid forms a polymer brush and shields the cell membrane from generic interactions while also mediating weak long distance interactions [150]. To *mediate specific adhesion*, proteins on the cell surface interact with other proteins (e.g. on the membrane of a second cell or in the extracellular matrix) like a lock and a key. Only an appropriate receptor-ligand pair can recognize each other [8]. The receptors are either an integral part of the lipid membrane, attached to the periphery of the lipid bilayer or anchored via polymers. They are highly specific and allow cells to selectively bind to a neighboring cell or the extracellular matrix that expresses the appropriate receptor.

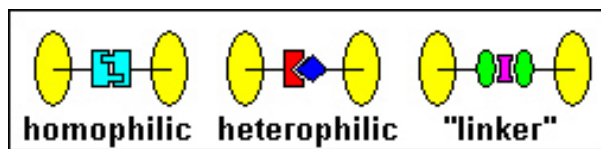


Figure 3.16. Three possibilities for receptor-ligand interactions. From [151]

Describing the adhesion of a biological cell to another cell or to the extracellular matrix requires elements from cell biochemistry, structural mechanics, and surface bonding. As described in figure 3.16, interaction between a ligand and a receptor is mediated via a homophilic interaction, a heterophilic interaction or a connection through a linker molecule.

While the function of adhesion molecules at the molecular level follows this scheme (see figure 3.16), the adhesion of cells also depends on how these adhesion molecules assemble into ordered structures, such as focal contacts. Moreover, cascades of signaling pathways leading to interactions with the interior of the cell, such as the cytoskeleton, have been identified [67]. Eventually, the cytoskeleton may organize to form stress fibers in response to adhesion. Adhesion molecules can also be up- and downregulated, as occurs when they become more "sticky" by activation. The biochemistry of adhesion and the sequence of reorganization in cell spreading is discussed in chapter 2.

A first step to characterizing cell adhesion is to study protein-protein interactions on the single molecule level. Combining molecular cell biology with single molecule techniques (biomembrane force probe, AFM) has given considerable insight into the complexity of cell adhesion. Studies have focused on understanding how cell signaling processes strengthen adhesion bonds and how forces applied to cell-surface bonds act on intracellular sites to catalyze chemical processes. This approach can reveal important links in the communication between mechanical and chemical circuitry of a cell and has been actively pursued by many biophysics groups.

The physical role of a cell adhesion bond is to attach a cell to another cell or surrounding tissue while supporting the forces involved in cell function. However, a single adhesion bond effectively resists force only for time periods less than that needed for its spontaneous dissociation under thermal activation. Indeed, mechanical force applied to a bond between two interacting proteins decreases the activation energy barrier along kinetic pathways, or switches biochemical pathways that lead to dissociation (figure 3.17).

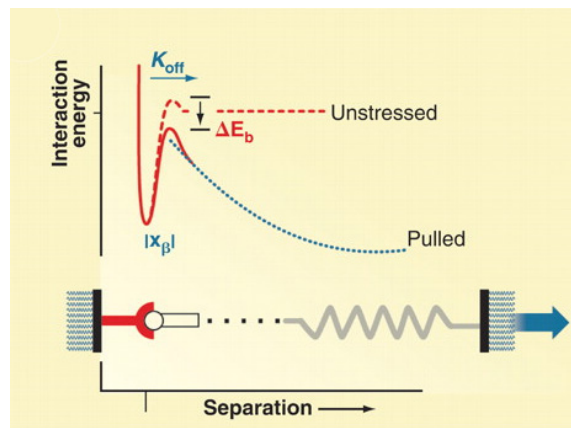


Figure 3.17. Conceptual view of force propagation to a bond and its impact on the chemical energy landscape governing bond kinetics. From [152].

Pulling on a molecular bond creates a mechanical "springlike" potential (dashed blue curve in figure 3.17) that alters the chemical energy of interaction or "landscape" (solid and dashed red curves in figure 3.17) along the reaction coordinate defined by the pulling direction [152]. The slope of the spring potential at the origin of interaction is the pulling force f , i.e. the product of the effective spring constant κ_s of the structural linkages with the increase in their separation $x_{separation}$ under pulling. The dissociation energy depends on the velocity through the loading rate [153]. Of greatest impact on bond survival, the spring potential reduces the height of the activation energy barrier governing the off-rate kinetics located at x_β by $\sim -fx_\beta$. First described by Bell in 1978 [154], the change in Arrhenius factor predicts a large exponential-like reduction in bond survival time, $t_{off}(f) \approx t_{off} \exp(-f/f_\beta)$, relative to its apparent unstressed lifetime t_{off} (For adhesive interactions relevant in soft tissues and organs of eukaryotic cell systems, the average times t_{off} reported for spontaneous dissociation of ligand/receptor bonds range from a fraction of a second to 100 s or more).

C.2.1 Techniques

At least three different methods [155] have been developed to monitor the rupture of individual ligand-receptor bonds subjected to applied forces in the piconewton range. These have shown that non-covalent associations between biomolecules can be rapidly ruptured with forces ranging between a few tens and hundreds of piconewtons.

- **Hydrodynamic flow** This method was used by the group of P. Bongrand [156] to determine the detachment kinetics of single bonds formed by E-selectin and its ligands by flowing leukocytes. A particle of radius a coated with ligands is bound to another particle or a macroscopic surface coated with receptors. If the fluid has a viscosity of μ with a locally varying shear flow rate G then the particle is subjected to a force of the order of $\mu a^2 G$. If bonds are ruptured, particles will then be transported in the flow with a velocity of order of aG . Thus, if we consider a cell-size particle of $10 \mu\text{m}$ radius in a fluid of $0.001 \text{ Pa}\cdot\text{s}$ viscosity such as water, a shear rate of 10 s^{-1} may generate a hydrodynamic drag of order of 0.1 pN and a relative velocity of $100 \mu\text{m s}^{-1}$. Therefore, the mere observation of the particle with a conventional microscope may, in principle, allow a detailed examination of single-bond rupture with a time resolution of a few tens of milliseconds.
- **Biomembrane force probe (BFP) technique** This approach was pioneered by Evans et al. [153], [157]. A typical experiment consists of using a red blood cell (RBC) aspirated at controlled tension as the force transducer. As BFP tip, a glass microbead is chemically glued to the membrane, which is functionalized with one type of ligand. A second bead held by a second pipette and functionalized with the receptor is brought into contact by precision piezo control (see figure 3.18). After allowing bonds to form, a pipette is pulled out under microscopic control. The applied force results in RBC membrane deformation, and a spherical shape is recovered when the last bond is ruptured. Thus, the experimental result is the *unbinding force* rather than the bond lifetime. As emphasized by the authors, the power of this approach is that the surface tension of the red blood cell may be varied over a wide range by controlling the aspirating pressure applied through the pipette. RBCs can indeed be subjected to a distractive force ranging between less than 1 and 100 pN . Different loading rates are accessible as the pipette approach velocity can be varied over a large range. With fast video ($\approx 1,000$ frames per s) processing, image tracking of the bead is possible, which yields a resolution of $8\text{-}10 \text{ nm}$ for transducer deflection. The deformation of the membrane may be analyzed in order to calculate the force.
- **Atomic force microscopy (AFM)** The principle consists of moving a

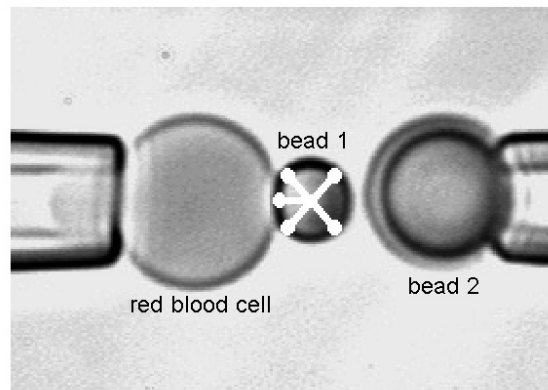


Figure 3.18. *BFP. Studying individual ligand-receptor bonds with the biomembrane force probe. A typical experiment uses a red blood cell aspirated at controlled tension in a micropipette as the force transducer. As the BFP tip, a glass microbead is chemically glued to the membrane which is operated on the stage of a microscope. The BFP (on the left) is kept stationary and the microbead test surface (on the right) is translated to/from contact with the BFP tip by precision piezo control. From [153].*

ligand-coated surface towards a very thin receptor-bearing tip mounted on a very soft cantilever (a typical spring constant is about 100 mN m^{-1}) (see figure 3.19). The surface is then pulled out, resulting in continuous increase of the force, with continuous monitoring of the cantilever deformation. The rupture of the last bond between surfaces results in a sharp jump of the cantilever, allowing experimental measurement of the unbinding force. The cantilever position may be monitored with ångström accuracy with optical techniques. The optical limit set by thermal fluctuations to the force sensitivity is about $(kT/\lambda)^{1/2}$, where λ is the spring constant. The reported force sensitivity is of the order of 10 pN in liquid medium (Erlandsson and Olsson in [155], and [158]).

C.2.2 The example of the Streptavidin-biotin pair

The ligand-receptor pair streptavidin-biotin is a standard system which has been studied using the above methods.

- **AFM** Chronologically, the AFM technique was used first to study the avidin-biotin system. A tip was coated with biotinylated albumin and brought into contact with soft agarose beads bearing streptavidin binding sites [158]. Using the force scan mode, multiple approach-retract cycles were performed and hundreds of unbinding events could be visualized as sharp jumps of the cantilever. The distribution of unbinding forces displayed quantized peaks that appeared as multiples of $160 \pm 20 \text{ pN}$.

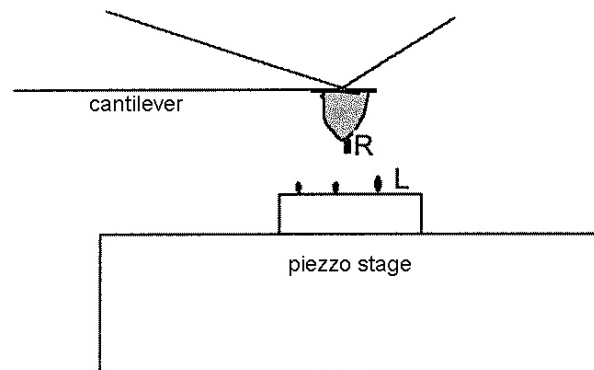


Figure 3.19. Studying individual ligand(L)-receptor(R) bonds with an atomic force microscope. A receptor-bearing tip (a few nanometer thickness) mounted on a very soft cantilever is brought in contact with a ligand-coated surface. The unbinding force is then measured.

This was considered as representative of the detachment force of a single bond. Further, when biotin was replaced with iminotiotin, an analogue with 25 000-fold lower affinity to streptavidin, the unit separation force was reduced to 85 ± 15 pN.

- Hydrodynamic flow** Pierres et al. [159], [160] used the flow chamber technology to study the high affinity interaction between biotin and streptavidin. The lifetime of interactions between biotinylated surfaces and streptavidin-coated spheres was of the order of several seconds, i.e. 5-50-fold higher than determined on selectin/ligand or CD2/CD48 models [161]. Further, this lifetime was not decreased when the shear rate was increased from 10 to 40 s^{-1} . However, it was concluded that the flow chamber was not well suited to the study of strong interactions, since (i) the chamber floor was rapidly filled with definitively attached particles, which made it difficult to follow a sufficient number of trajectories in a single experiment, and (ii) it was somewhat difficult to obtain a reliable distribution of arrest durations, since the computer-assisted apparatus was not adapted to the monitor very long arrests.
- Biomembrane Force Probe Technique** Evans et al. [153], [162] reported a study of biotin-streptavidin association. When bonds were subjected to a loading rate of 100 pN s^{-1} , the unbinding force was about 50 pN. The force was reduced when streptavidin was replaced by avidin. The measured value was 4-5-fold lower than that measured with atomic force microscopy (see above), but the loading rates were probably differ-

ent in these two cases. The group of Evans was the first to emphasize the importance of the loading rate and probe the dependence of the unbinding force on the loading rate.

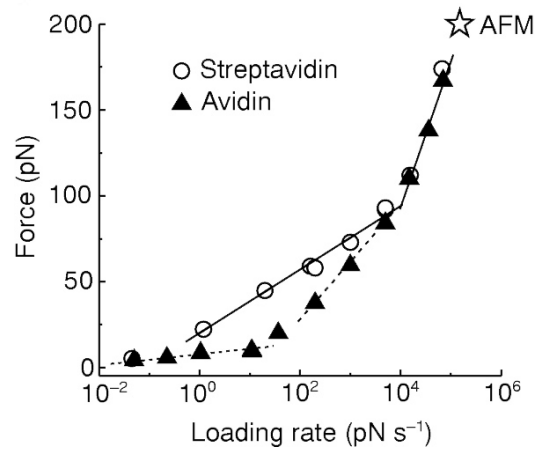


Figure 3.20. Force vs. loading rate diagram measured with BFP, showing the behavior when streptavidin is replaced by avidin. From [153].

Indeed, it is very interesting to note that very different values were obtained for the same ligand-receptor pair. This suggests that the results from these three techniques may only be comparable if the same **loading rate** is used in the experiment. This is not emphasized in the first two publications.

It is important to note, however, that cellular adhesion is a collective phenomena, involving many different types of cell adhesion molecules which are present in large numbers on cell surfaces and the extracellular matrix. It is therefore necessary to study the behavior of ensembles of cell adhesion molecules.

A Basic Principles

Quite a few systems for modeling cell adhesion have been studied both theoretically and experimentally, and these studies have shown the importance of specific interactions and the involvement of the cytoskeleton and other cellular structures. Nevertheless, the shape of a water droplet wetting a surface, a model cell (vesicle), and a cell adhering to a surface show remarkable similarities (see figure 4.1).

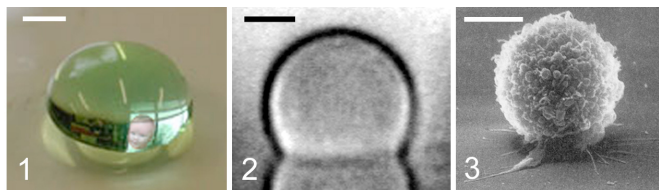


Figure 4.1. Similarities in shape between 1) A water droplet 2) A giant vesicle 3) A cell, spreading on a surface scale bar: 1) 1 mm 2) 10 μm , 3) 5 μm . From [163].

Indeed, the behavior of a water droplet deposited on a surface illustrates many of the important concepts in surface adhesion.

A.1 Water Droplet on a Surface

The shape of a water droplet on a surface depends both on its size (a semi-spherical cap in the capillary regime or flattened in the gravity-dominated

regime) and on the difference between its surface tension and the surface energy of the solid substrate [164], [165]. On clean glass (high surface energy, hydrophilic) the droplet wets the surface and forms a thin water film across the entire surface (total wetting situation).

If the surface energy of the substrate is lowered, the droplet spreads out into the shape of a truncated sphere (partial wetting situation).

The spreading parameter, S , which is the difference between the surface energy of the dry and wet surface determines whether or not a water droplet spreads on a surface. It is given by

$$S = E_{dry} - E_{wet} \quad (4.1)$$

which is equal to

$$S = \gamma_{SA} - (\gamma_{SL} + \gamma_{LA}) \quad (4.2)$$

where γ_{SL} is the surface tension between the solid and the liquid phase, γ_{SA} is the surface tension between the solid and the gaseous phase (air), and γ_{LA} is the surface tension between the liquid and the gaseous phase (air) (see figure 4.2). If $S > 0$, the liquid completely wets the surface (total wetting) forming a thin film on the surface, while partial wetting occurs when $S < 0$.

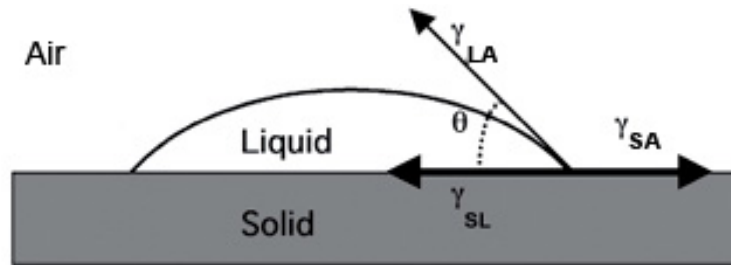


Figure 4.2. Partial wetting of a liquid on a solid substrate defining the contact angle θ at the contact line.

The static contact angle θ can be obtained by balancing forces balance at the contact (see figure 4.2) to give

$$\gamma_{LA} \cos \theta = \gamma_{SA} - \gamma_{SL} \quad (4.3)$$

for the contact angle θ : This can be expressed as the Young - Dupré equation by

$$S = \gamma_{LA}(\cos \theta - 1) \quad (4.4)$$

The greater the value of θ , the less the liquid wets the surface. The range $-1 \leq \cos \theta \leq 1$ corresponds to partial wetting, while $(\cos \theta > 0)$ corresponds to a total wetting situation.

A.2 Adhesion of Vesicles : Static Approach

The adhesion of vesicles depends upon the nature of the interaction between the substrate and the vesicles. For instance, electrostatic interactions between a poly-lysine-coated glass slide and a vesicle made from phosphatidylcholine lipids lead to spreading of the vesicle on the surface. If the surface density of poly-lysine is high enough, the vesicle will rupture to form a lipid bilayer [86]. When the surface is passivated (coated with casein, a BSA layer, or a hydrophilic polymer like PEG), the vesicle can settle on the surface, but does not adhere [153], [166], [167]. For intermediate cases, the vesicle can bind to the substrate and assumes a truncated spherical shape, very similar to the water droplet described above (see figure 4.1).

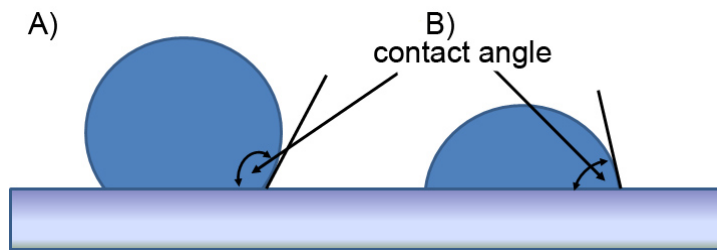


Figure 4.3. A) A vesicle sitting on a passivated surface with a contact angle greater than 90° . B) A vesicle adhering to a surface covered with a low density of poly-lysine and a contact angle smaller than 90° .

In the case of strong adhesion mediated by long-range interactions, the vesicle assumes the shape of a spherical cap characterized by a contact angle θ . The point of contact can be described by the Young - Dupré equation which in this case links the adhesion energy W per unit area, the membrane tension γ and the contact angle θ (see equation 4.5).

The adhesion energy W is defined as

$$W = \gamma(1 - \cos\theta) \quad (4.5)$$

In principle, knowing the membrane tension and measuring the contact angle, the adhesion energy can then be deduced [168], [169], [170].

Seifert et al. have also modeled the adhesion of vesicles theoretically [171]. The attractive adhesion energy (e. g. van der Waals interactions, electrostatic forces,...) is partially compensated by the bending rigidity κ and the volume of the vesicle is not assumed to be constant. In the model the competition between adhesion and bending is described by the dimensionless parameter, $w = \frac{WR^2}{\kappa}$, where R is the radius of the vesicle. $w > 1$ characterizes a strongly adhering vesicle, while $w \sim 1$ corresponds to a weak adhesion state.

The **initial tension** of the membrane also has to be taken into account. For floppy vesicles, this is described by the reduced volume of the vesicle $v =$

$\frac{V}{\frac{4\pi}{3} \times (\frac{A}{4\pi})^{\frac{3}{2}}}$, where V is the volume and A is the area of the vesicle. For floppy vesicles, $v < 1$. Using w and the reduced pressure p ($p = PR^3\kappa$ where P is the osmotic pressure difference between the outside and the inside of the vesicle.), a phase diagram for bound vesicles was calculated by minimizing the associated free energy via Monte Carlo simulations [171], [172], [173]. An example of the vesicle deformation due to changes in interaction (w) and in the reduced pressure p (i.e. in membrane tension) is given in figure 4.4.

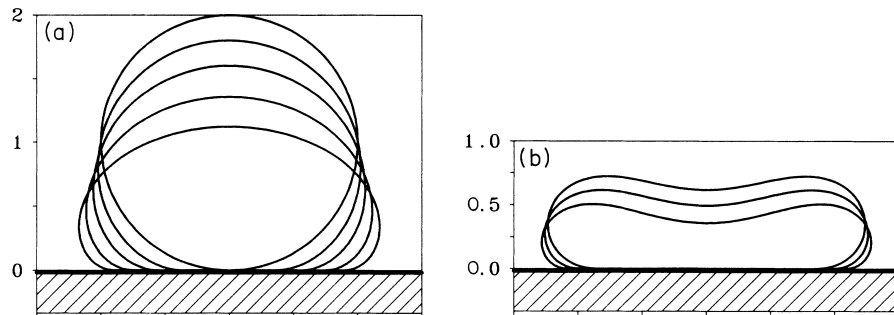


Figure 4.4. Shapes of bound vesicles that all have the same area $A = 4\pi$ a.) for reduced pressure $p=0$ and reduced contact potential $w = 2.0, 2.9, 4.1, 6.4, 10.2$ with increasing contact area A^* . Shapes for $p < 0$ look similar. b.) $(p,w) = (14.6, 2.0), (14.0, 6.1), (14.1, 12.9)$ with increasing A^* . From [171].

For the case of strong adhesion, Tordeux et al. [174] found analytic descriptions for the shape of the contact zone and the contact angle of an adhered vesicle. They assumed that the volume V and the area A of the vesicle are constant and defined a number of geometrically measurable parameters ($L =$ adhesion disk radius, $\lambda_d = \sqrt{\frac{\kappa}{\sigma}}$ = extrapolation length, $\theta =$ contact angle, $R =$ the vesicle radius, $H =$ height of the vesicle measured on the revolution axis z) (see figure 4.5). A parameter to describe adhesion was introduced, which for strong adhesion was defined as

$$\epsilon = \frac{1}{L} \sqrt{\frac{\kappa}{W}} \ll 1 \quad (4.6)$$

Figure 4.6 depicts the geometry of the contact between the vesicle and the substrate. The membrane curves up from the actual point of contact such that at distances greater than λ_d it approaches the limiting value of θ (see also figure 4.6) [166]. The authors also discussed the effect of the adhesion energy on the height, H , of the adhered vesicle.

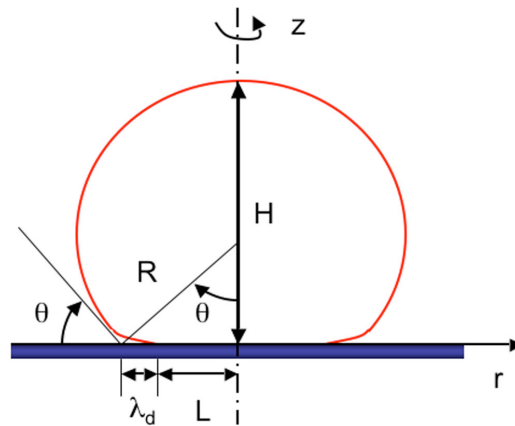


Figure 4.5. Analytical description of a strongly adhered vesicle using geometrically measurable parameters: L = adhesion disk, the extrapolation length $\lambda_d = \sqrt{\frac{\kappa}{\sigma}}$, θ = contact angle, R = the vesicle radius, H = height of the vesicle measured on the revolution axis z . From [174].

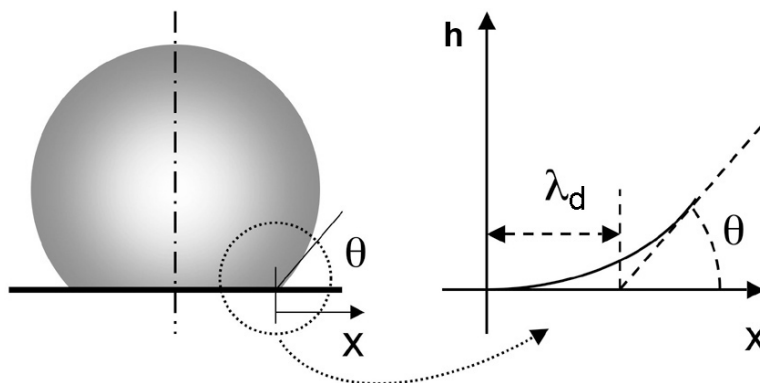


Figure 4.6. Geometry of the contact. A) The contact angle θ defines the contact between vesicle and substrate on a macroscopic scale. B) The profile close to the contact line is actually not the vertex of the contact angle θ . Due to the curvature of the membrane, the angle increases from 0 to θ over a characteristic length, λ_d , the extrapolation length. [166]. From [163].

A.3 Comparing Water Droplet and Vesicle Spreading

In recent years, specific adhesion of vesicles (mediated by proteins on the vesicle surface and the substrate to which the vesicle adheres) has been studied both theoretically and experimentally. In general, specific adhesion of vesicles is more complicated than the case of wetting of a simple fluid droplet on a surface. This is because some parameters change during the adhesion process. First,

- While the surface energy of a liquid is constant, the *membrane tension* of a vesicle can increase during vesicle adhesion. The transition from a sphere to a truncated sphere induces an area increase that reduces membrane fluctuations. If the vesicle gets too tense, pores can open [175], and the vesicle can eventually rupture [86].
- Secondly, the *ligands* on the membrane bilayer can *diffuse freely*, and can therefore aggregate at the adhesion zone, thus influencing the adhesion energy.

We have mentioned above some studies of vesicle shape under static conditions. In recent years, only a few theoretical and experimental studies of the adhesion kinetics of vesicles have been published and these will be described in section B.

B Theory: Adhesion Kinetics of Model Membranes Mediated by Specific Interactions

The results of several theoretical and experimental studies are briefly summarized.

B.1 Simulations

B.1.1 Numerical Simulations on Spreading of a Model System for Cell Adhesion

Hodges et al. [176] modeled cell adhesion via numerical simulations. The cell was treated as an extensible membrane under tension containing fluid of constant volume. Assuming rapid binding kinetics, molecular binding forces were described through a contact potential that was attractive at long ranges but repulsive at short ranges. Using lubrication theory to describe the thin-film flow between the cell and the plane, they modeled the sedimentation of the cell onto the plane under adhesive forces. They then studied the removal

of the cell from the surface under the action of an external force. The authors calculated the adhesion dynamics by averaging numerous dimensionless molecular parameters. For these numerical simulations, adhesion and detachment events were dominated by quasi-steady spreading and peeling motions, which could be described using an asymptotic analysis. The analysis was then extended to model a cell tank-treading over an adhesive wall under the influence of an external shear flow. The relation between cell rolling speed and shear rate was determined. At low speeds it was linear and independent of the viscosity of the suspending fluid, while at higher speeds it was nonlinear and viscosity-dependent.

B.2 Analytical approaches

B.2.1 Kinetics of membrane adhesion mediated by ligand-receptor interaction (Boulbitch et al. approach)

This work employed both experimental and theoretical techniques. The first model for specific ligand-interaction mediated adhesion was proposed by A. Boulbitch [140]. For the experimental work, vesicles were prepared carrying RGD-anchored lipids, representing the ligand, and PEG-polymer, mimicking the cell glycocalyx. Their adhesion onto a surface covered with the integrin $\alpha_{IIb}\beta_3$, (a receptor for the RGD-peptide) was then studied. The experiments are presented in detail in section C.4 Their theoretical study distinguished two situations: 1) a diffusion-dominated regime when the vesicle is covered by a low density of ligands. For this case the diffusion of the ligands to the adhesion zone limits the adhesion. 2) a regime of high ligand density dominated by the kinetics of ligand-receptor association. The spreading of the vesicle is then limited by the reaction time between ligand and receptor.

The authors showed both experimentally and theoretically that at low ligand concentrations, the kinetics of the displacement of the front of tight adhesion followed the square root law, which can be expressed as $R \sim t^{1/2}$ (R being the radius of the adhesion zone). At high ligand concentrations, a linear law $R \sim t$ was found. In the first case, the scaling law was obtained by choosing adequate boundary conditions and by combining the diffusion equation with the conservation of the total number of molecules. For the high ligand concentration, the characteristic time for displacement of the adhesion front was controlled by the bond formation kinetics corrected by a Boltzmann factor taking into account the fluctuation energy imposed by the PEG polymer brush. For this case, the adhesion zone increases with a constant velocity and $R \sim t$.

The proposed model introduced a large number of parameters that could not be easily measured. However, the model gave an excellent fit to the experimental data presented in [140].

B.2.2 Growth and Shape Stability in an Adhesion Plaque in the Diffusion-Mediated Regime (Shenoy et al.)

A more recent theoretical approach was published by Shenoy et al. [177]. The authors focus on the process of expansion of an adhesion zone with a low density of ligands, as is typical in cellular adhesion. The recruitment of new ligands at the edge of the adhesion zone was modeled through a gradient of chemical potential between the adhesion zone and the rest of the non-adhering membrane.

The evolution of the circular adhesion front in the diffusion-limited regime varies with $R \sim \alpha\sqrt{Dt}$, where D is the diffusion constant and α a prefactor that is discussed in detail and compared to [140]. The evolution of the radius $R \sim \sqrt{t}$ is in agreement with Boulbitch et al.. The authors insist furthermore on the existence of an original instability of the circular shape of the adhesion zone.

B.2.3 A More General Approach: de Gennes and Brochard-Wyart

F. Brochard-Wyart and P.-G. de Gennes proposed several theoretical scenarios to explain the adhesion of a vesicle on a variety of substrates [165], [178], [179].

As in the approaches described above, they considered a vesicle carrying on its surface a small number of mobile "stickers". When facing a substrate with suitable receptors for the stickers, the vesicle builds up an adhesion patch. They analyzed the patch growth dynamics under a variety of situations. They took into account the variation of surface preparation (mobile or immobile receptors on the surface), the presence or absence of non-specific interactions, the preparation of vesicles (i.e. "heavy" vesicles due to osmolarity difference with the surrounding medium), the influence of the membrane tension, the competition of diffusion of the ligands and the reaction time, and the distribution and accessibility of the receptors in the adhesion zone. The authors showed that each parameter can have a significant influence on the growth rate of the adhesion zone. We will later discuss the theory in detail, as we will use this approach to analyze our experimental data in chapter 6.

Even though the approaches described above find similar power laws for $R(t)$, this agreement might be coincidental as the underlying mechanisms differ.

Our results will be analyzed with the theoretical approach by F. Brochard-Wyart, as this approach uses the smallest possible number of unknown physical parameters. We will carefully compare our experimental data to the results obtained by P.-H. Puech for floppy biotinylated vesicles adhering to streptavidin covered supported lipid bilayers, and the corresponding theoretical explanation by de Gennes and Brochard [179] (see also chapter 6). Our vesicles were

floppy just like the vesicles studied in [179]. Most parameters in the model could be obtained independently of the current experiments which allowed a simple comparison of the theoretical predictions to our experimental data.

C Experiments: Functionalized GUVs Mimicking Cell Adhesion

Several experimental systems have been developed using functionalized GUVs to mimic cell adhesion. Even though not all of them have been used to study adhesion *dynamics*, all the systems will be presented to characterize the state-of-the-art in adhesion model systems involving GUVs.

C.1 Adhesion Dynamics of GUVs mediated by Biotin-Streptavidin Systems

The biotin-streptavidin pair is a very popular receptor-ligand pair (used in in-AFM, Biomembrane Force Probe, Hydrodynamic Flow studies, see also chapter 3) and has also been used in adhesion studies of functionalized GUVs. Studies have been done both for immobile ligands on the substrate and with mobile ligands incorporated into a supported lipid bilayer.

C.1.1 Immobile Receptors on the Substrate

Cuvelier et al. [180] studied the kinetics of giant vesicle adhesion mediated by the receptor-ligand pair biotin-streptavidin. Two types of substrates with immobile ligands (biotin) were prepared that differed in their chemical preparation and it was found that substrate preparation had a large impact on the resulting adhesion dynamics. Egg phosphatidylcholine (EPC) vesicles were doped with 0.05 to 5% in weight of biotinylated lipid. After electroformation, streptavidin was added to the vesicle suspension in order to bind to the biotinylated lipid. After binding, excess streptavidin was removed by centrifugation. As target surfaces, two kinds of biotinylated substrates were generated, referred to as 1) casein-biotin and 2) PEG-biotin surfaces. The former was obtained by adsorption of casein pretagged with a short biotin derivative, NHS-biotin. The latter was obtained by grafting a long and flexible SBA-PEG³⁴⁰⁰-biotin cross-linker (NHS ester of PEG butanoic acid) to an aminosilanized glass slide. Both had similar surface density of biotin groups available to streptavidin. The adhesion dynamics of streptavidin-functionalized vesicles spreading onto biotinylated substrates was in both cases followed by RICM (see figure 4.7).

The adhesion kinetics strongly depended upon the chemical preparation of the substrate. Vesicle adhesion was completed within a few seconds on PEG-biotin substrate although this could be slowed for vesicles with lower streptavidin density Γ_0 . In contrast, for casein-biotin substrates spreading took

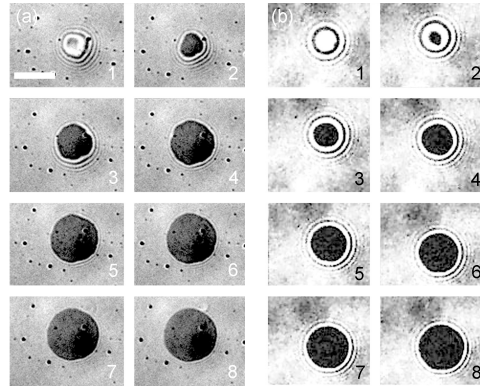


Figure 4.7. RICM image sequence of the contact zone of a vesicle at streptavidin coverage $\Gamma_{sat}/10$ a) on a PEG-biotin surface, Γ_{sat} = the saturated concentration of streptavidin in the adhesion zone; b) on a casein-biotin surface. The time interval between two images is 5s for a) and 30s for b), bar = 5 μ m. From [163].

more than 10 minutes and was not affected by Γ_0 (see figure 4.8). Since these differences cannot be attributed to a difference in biotin density on the surface, the theoretical modeling took into account differences in the chemical state of the two substrates. It was proposed that for the casein-biotin substrate, the accessibility of the biotin to streptavidin is reduced in comparison to the PEG-biotin surfaces. In this case, the limiting event is the reaction between the streptavidin and biotin. Adhesion to PEG-biotin gave a growth law of $R \sim t^{\frac{1}{2}}$, while the growth rate on the casein-biotin substrates followed $R \sim t^{\frac{2}{7}}$

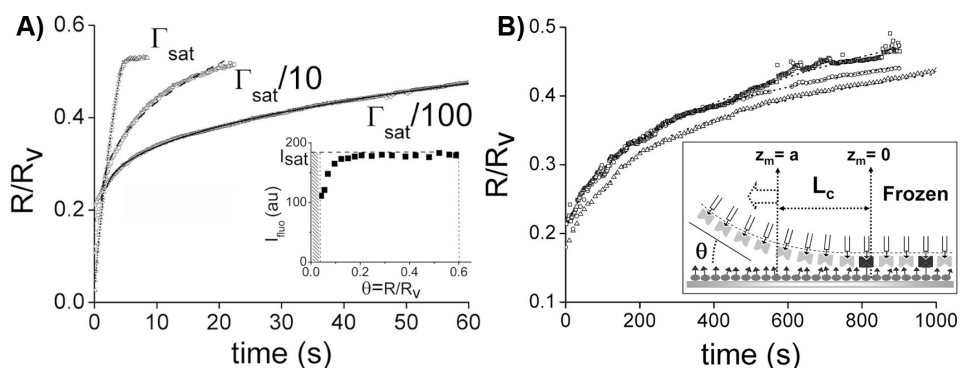


Figure 4.8. Typical time evolution of the patch normalized by the radius of the streptavidin vesicle with different streptavidin densities Γ_0 adhering onto different biotin surfaces. The dashed line shows the fits obtained from theoretical predictions. (A) PEG-biotin, B) casein-biotin) From [180].

C.1.2 Mobile Receptors on the Substrate

Puech et al. [179] studied the adhesion of a slightly different biotin-streptavidin system. Unlike the experiments by Cuvelier et al., the biotin-streptavidin receptors were mobile on the substrate, since streptavidin was attached to a lipid-anchored biotin incorporated into a fluid supported lipid bilayer. Vesicles made from 1,2-Dioleoyl-*sn*-Glycero-3-Phosphocholine (DOPC) containing 1 % of 1,2-Dioleoyl-*sn*-Glycero-3-Phosphocholine (DOPE) Cap biotin. Supported lipid bilayers were formed with the same lipid composition on clean glass substrates, and were incubated with streptavidin leading to a substrate with mobile streptavidin ligands. The adhesion kinetics of biotinylated GUVs adhering on the streptavidin substrate was followed with RICM.

The adhesion dynamics of 1) tense vesicles and of 2) floppy vesicles were studied separately.

1. **Kinetics of tense vesicles** For non-adhered vesicles the membrane tension varied from $\sim 10^{-7}$ to $\sim 10^{-4}$ N/m. Fairly tense vesicles appeared as a spherical object in light microscopy. When adhering via the streptavidin/biotin couple, the contact zone appeared as an almost perfectly circular dark shape in RICM as in the case described in section C.1.1. The contact zone grew slowly over several minutes. Extracting the power law of the area A versus growth time t gave $A \sim t^{0.4}$, and as the adhesion patch was circular, its radius varied as $R \sim t^{0.2}$ (see image 4.9). For the work of Cuvelier et al. the vesicles were tense. However, strikingly different growth laws were obtained. This shows the large influence of the mobility of the stickers on the growth rate.
2. **Kinetics of floppy vesicles** When one introduces a difference in osmolarity between the inside of the vesicle (-) and its surrounding media (+), water flows through the membrane to compensate this osmotic difference, leading to an increase of the surface to volume ratio. The membrane is then subjected to large amplitude thermal fluctuations [181].

As depicted in the first picture of the sequence of figure 4.10A and described in detail in [179], the contact zone was much larger than for the tense vesicles. (It is important to distinguish the contact zone and adhesion zone. While the contact zone is the zone where the vesicle is close to the surface (the whole circular area in figure 4.10A), the adhesion zone is the part where the membrane actually adheres (black areas within the circular area).) The gray levels in the contact zone were fluctuating, indicating fluctuations in the distance between the membrane and the surface. These fluctuations have been described theoretically, in particular by W. Helfrich [88]. Due to the relatively low bending rigidity of the membrane, thermally excited fluctuations occurred which had optically detectable amplitudes. As explained in [178], floppy vesicles sit on a

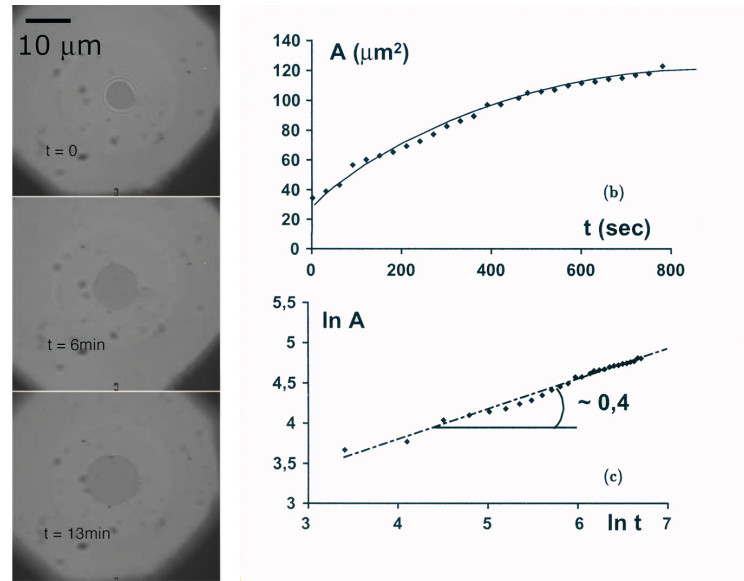


Figure 4.9. a) Adhesion of a fairly tense vesicle on a substrate with mobile stickers (image taken in RICM). The single adhesion patch grew from the middle and was almost circular. b) Area of the adhesion patch as a function of time. c) Log-log plot of the area A versus growth time t gives $A \sim t^{0.4}$. From [179].

liquid cushion. The adhesion process started when a membrane fluctuation pierced this cushion and the membrane bound to the complementary surface (black arrow on the first picture of the sequence). Usually, these events occurred at the edge of the contact zone and not in the center, probably because of the existence of a central dimple [178]. Then, over several seconds, multiple small adhesion spots grew in a rather circular manner and fused (white arrow in the second picture of the sequence, figure 4.10A). After a few minutes, almost all the individual adhesion patches fused. They formed a single, irregular shaped, adhesive contact that kept on growing but with a slowing rate (figure 4.10C). Because of the relatively rapid fusing behavior of the small adhesive spots it was difficult to follow them for a long time (usually this can be done from 1 second to 1 minute). The growth of the total contact area followed a power law for a single patch at short times (figure 4.10D), $A \sim t$ leading to $R \sim t^{0.5}$ for its radius (figure 4.10D), and $A \sim t^{1.9}$ leading to $R \sim t$ for an equivalent radius (figure 4.10E) at long times. These two regimes have been studied theoretically. The paper did not discuss whether the adhesion process continued (as in our experiments) or stopped after ring formation.

The theoretical explanations presented in the paper agreed well with the

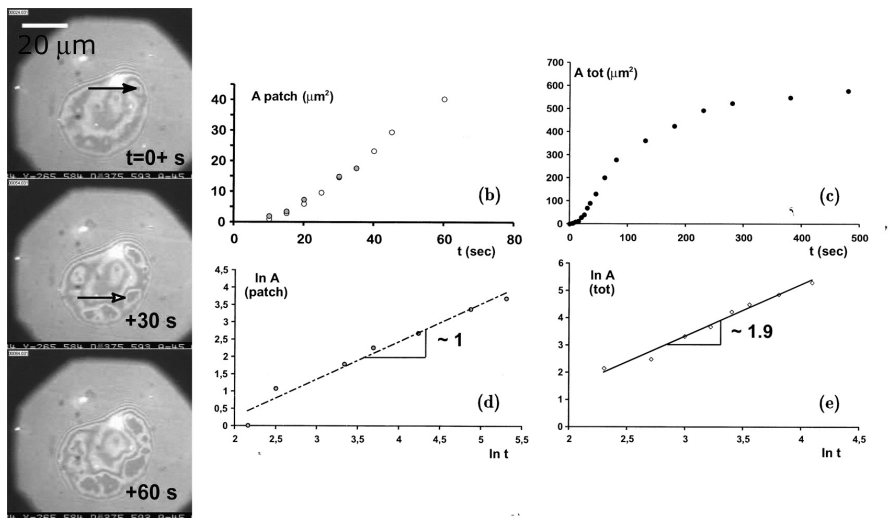


Figure 4.10. *a) Adhesion of a very floppy vesicle ($2R_v \sim 100 \mu\text{m}$) on mobile ligands as seen in RICM. Small adhesion spots appear (black arrow in image 1), grow and eventually fuse. The remaining non-adhering membrane is fluctuating (grey part). b) Area of two small spots as a function of time c) Plot of the total area of the spots versus time d) calculation of the power laws for a single patch $A \sim t$, leading to $R \sim \sqrt{t}$ e) Calculation of the power law for the total contact area, $A \sim t^{1.9}$ leading to $R \sim t$ for an "equivalent" radius. From [179]*

experimental data, as they matched the experimentally found power laws for the growth of the adhesion zones for both floppy and the tense vesicles. The theory of the floppy case will be discussed in chapter 6, as it closely corresponds to our experimental conditions.

C.2 The Homophilic Receptor Contact Site A from Dictyostelium Discoideum

The group of Prof. Sackmann at the TU Munich developed a system mimicking cellular adhesion using the homophilic (self-recognizing), lipid-anchored glycoprotein Contact site A from cells of the slime mold *Dictyostelium discoideum* [182]. This was one of the first attempts to build up a biomimetic adhesive system. The receptor was incorporated into giant vesicles as well as into a solid supported bilayer on the target surface. Additionally, lipopolymers PEG2000 were incorporated into the vesicles in order to form an artificial glycocalix. The interactions of the functionalized vesicles with the substrate were studied with RICM, and the adhesion strength was then evaluated. At low receptor concentrations, adhesion-induced receptor segregation in the membrane lead to decomposition of the contact zone into domains of strong (receptor-mediated) adhesion and regions of weak adhesion while at high receptor densities continuous zones of strong adhesion formed. Four different receptor concentrations in the giant vesicles were tested with protein-to-lipid molar ratio $r_{P/L}$ ranging from 4×10^{-6} , 8×10^{-6} , 4×10^{-5} to 8×10^{-5} (concentrations if 100 % of the proteins were incorporated). The protein-to-lipid molar ratio $r_{P/L}$ in the solid lipid bilayer was 2×10^{-3} . The RICM images of the four different conditions are shown in figure 4.11. With the help of contour analysis of the shape of the edge [183], the adhesion strength was described in terms of the spreading pressure S (=gain of energy due to the adhesion of the vesicle, [184]).

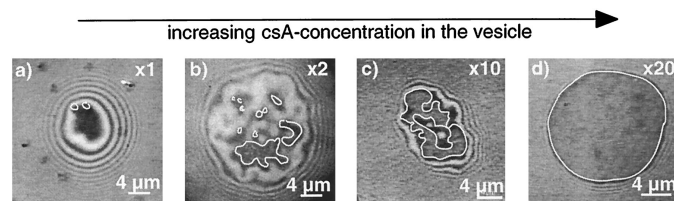


Figure 4.11. Effects of ligand concentration on vesicle adhesion. The csA-concentration was successively increased from the left to the right and span a range of 20x. The areas marked by white contours define the tight adhesion domains that are observed by time averaging of the intensity distribution to average out intensity fluctuations due to flickering. From [182].

The authors found that three states of adhesion could coexist at intermediate concentrations of csA. (see also image 4.11):

- The first was a state of weak adhesion, which was associated with strong flickering (4.11A). No bonds between csA pairs are found.
- The second was a state of intermediate adhesion strength (4.11B and C). Zones of tight adhesion (marked with white contours) coexisted with regions of weak adhesion. The weak adhesion zones fluctuated strongly.
- Third, a state of strong adhesion was observed (4.11D) forming an essential circular adhesion patch. No or small fluctuations were observed.

C.3 The Ligand- Receptor Pair Sialyl-Lewis^x - E-Selectin

Another system mimicking cellular adhesion was developed in the group of Prof. Sackmann using the weakly interacting ligand receptor pair sialyl-Lewis^x - E-selectin (the binding affinity is estimated to be between 5 and 7 $k_B T$) [185], [186]. As described in chapter 2, cells such as leukocytes or cancer cells depend on a selectin-based mechanism to establish weak, reversible adhesion that permit them to roll along vessel walls. Compared to the streptavidin-biotin model, the selectin system is of high biological relevance. In the developed model system, giant vesicles were functionalized with lipid-anchored sialyl-Lewis^x molecules and the substrate was coated with E-selectin. The vesicles also contain lipid-anchored PEG2000 molecules in order to mimic the cell glycocalix. The equilibrium state of adhesion was analyzed in detail using RISM technique. The authors found that the adhesion process relied purely on the formation of one or more adhesion domains within the vesicle-substrate contact zone. The adhesion was studied as a function of ligand concentration on the surface. It was found that the ligand content in the vesicle must be greater than 5 mol-% to establish specific contacts (in the absence of PEG). However, all concentrations for sialyl-Lewis^x above 8 mol-% provided a similar final state of adhesion. Finally, the size and shape of the adhesion domains strongly depended on both the concentration of E-selectin (0-3500 molecules/ μm^2) and PEG2000 (0 - 5 mol-%). At 3500 molecules/ μm^2 and small concentrations of PEG2000 (figure 4.12), the vesicle-substrate contact was maximized and consisted of a single adhesion domain. At concentrations of 5 mol-%, PEG2000 completely inhibited binding to the substrate. It should be noted that a concentration of 3500 molecules/ μm^2 of E-selectin corresponds to the typical concentration at cell surfaces.

C.4 The Ligand-Receptor-Pair Integrin- RGD

The group of Prof. Sackmann developed a third model system in which the surface was coated with the transmembrane protein integrin $\alpha_{IIb}\beta_3$, whose biochemical properties were presented before (see chapter 2). Giant vesicles were functionalized with a cyclic lipid-anchored RGD that is selectively recognized by integrin $\alpha_{IIb}\beta_3$ [140], [168]. In order to mimic the cell glycocalix, the

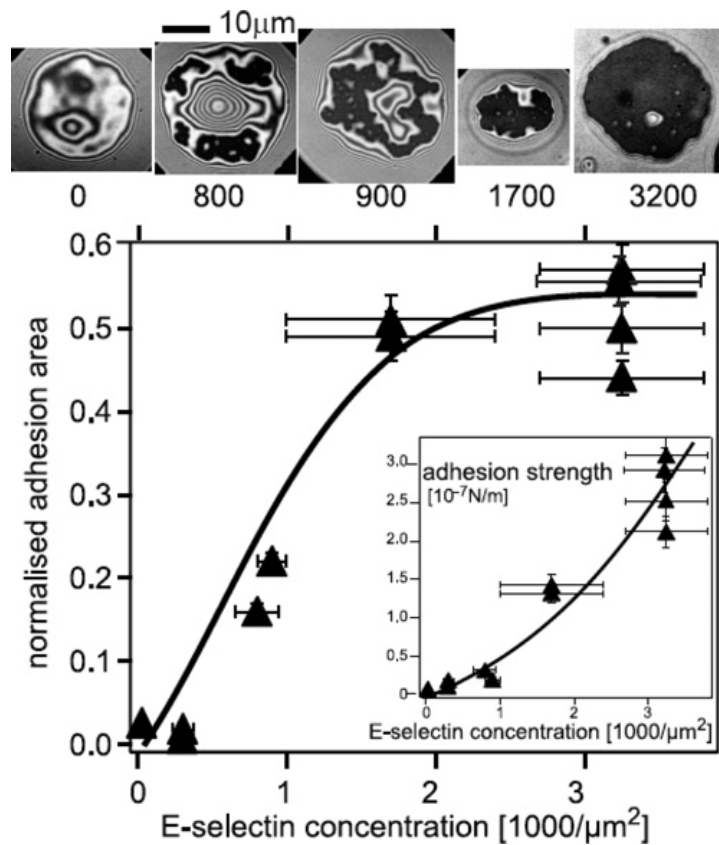


Figure 4.12. Adhesion as a function of E-selectin surface density at constant 1 mol % PEG2000 content. RICM images of the adhered vesicles are shown in the top row. The numbers underneath the micrograph denote the number of E-selectin molecules per square micrometer. The graph shows the normalized adhesion domain area as a function of the surface coverage. A strong increase at low coverage is followed by saturation at high coverage. (Inset) Adhesion strength increases over the whole observed range of surface density. From [186].

vesicles were also doped with PEG-polymer-carrying lipids. Although this geometry is the inverse of a biological situations, this work was essential for the implementation of our own model system as we benefitted from the expertise of the Sackmann group in membrane protein purification and handling.

The adhesion of these functionalized vesicles onto the integrin-covered surfaces was studied. Two different versions of the systems were developed with a) the integrin immobilized on the surface (physisorbed integrin) and b) the integrin able to diffuse over the surface (integrin incorporated into a supported lipid bilayer).

a) **Physisorbed Integrin**

The integrin was solubilized with the help of a detergent (Triton) and was fixed on glass substrates by physisorption [168]. This decorated surface played the role of a target cell (see figure 4.13).

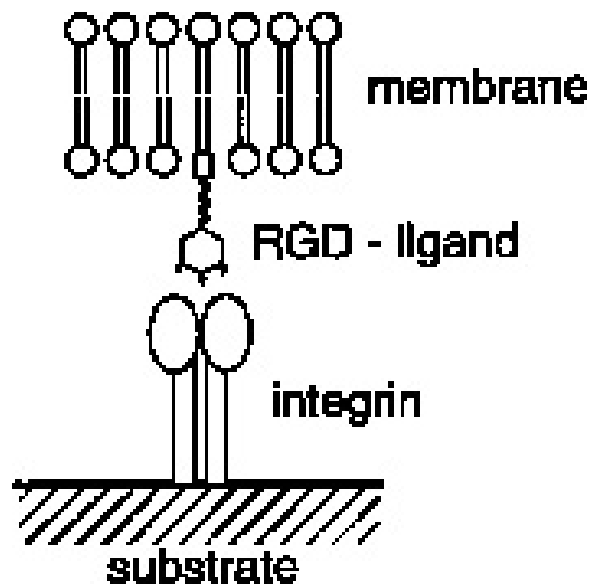


Figure 4.13. Vesicles carrying lipid-anchored RGD adhere to immobilized physisorbed integrin receptors. From [168].

This system was used to study several aspects of the interaction of the RGD-covered vesicles with the integrin-functionalized surfaces.

First, the unbinding forces of the RGD-integrin couple was measured by pulling on magnetic beads attached to the top of an adhered vesicle. Force was generated with magnetic tweezers while de-adhesion was monitored with RICM (see figure 4.14) [168]. RICM images showed that the adhesion zone was heterogeneous, which was explained as a result of the mobile ligands in the vesicle membrane. Pinning sites of a radius of the order of 100 nm (triangular shapes in RICM image when force is

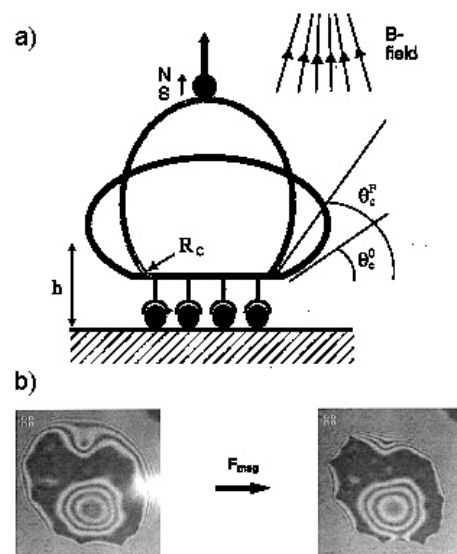


Figure 4.14. Pulling on a RGD vesicle adhering on an integrin surface with magnetic tweezers. a) The force transducer consists of a magnetic bead (acting as a tweezer) which is coupled to the membrane at the top of the vesicle and pulled in vertical direction with the help of magnetic tweezers. b) The development of the de-adhesion of the vesicle due to the applied force is followed by RICM technique. The black area shows the adhered part of the vesicle and is decreasing when force is applied. From [168].

applied, image 4.14B) were observed which contained large numbers of ligand-receptor pairs. In general, it was possible to unbind these pinning centers with applied force of order of 1 pN or less. Single-molecule force studies of ligand-receptor pairs report rate-dependent unbinding forces in the range of 50 pN or more. The authors interpreted these results as fracturing of the receptor-ligand pairs due to a torque on the edge of the adhesion disk. This torque was more important than the traction.

Furthermore, the kinetics of vesicle adhesion to an integrin-covered substrate was studied experimentally [140]. The theoretical part of this work was already briefly described above in section B.2.1. The adhesion of the vesicle to the integrin-covered surface started with the spontaneous formation of a small (~ 200 nm) domain of tight adhesion, which then gradually grew until the whole adhesion area was a state of tight adhesion (figure 4.15). The time of adhesion varied from few tens of seconds to about one hour depending on the ligand and PEG-lipopolymer concentration.

The kinetics of adhesion of a single giant vesicle was controlled by the competition between membrane-substrate interaction (specific ligand-receptor interaction, gravitation, and Helfrich repulsion) and followed by RICM. At small ligand concentrations, the displacement of the front of tight adhesion followed the square root law $R \sim t^{\frac{1}{2}}$, whereas, at high concentrations a linear law $R \sim t$ was found. [140].

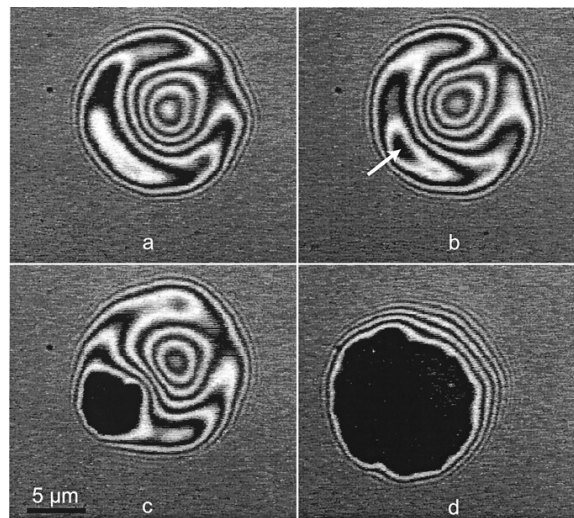


Figure 4.15. Adhesion area of a RGD-functionalized vesicle adhering to an integrin-covered surface. a) The vesicle in the weak adhesion state. b) Nucleation of the state of strong adhesion. c) and d) The strongly adhered patch grows. From [140].

Moreover, the segregation of RGD-ligands and enrichment within the adhesion patch was visualized by fluorescence (see figure 4.16). A fluorescently labeled RGD-lipid was synthesized which could be easily incorporated in giant vesicles. The adhesion of these vesicles was then studied simultaneously by RICM and fluorescence microscopy [187]. They observed the micro-segregation of RGD lipids in the contact zone during adhesion (see figure 4.16). It was shown that the fluorescent marker was only located in the contact zone indicating that strong adhesion was established via the RGD-integrin bond.

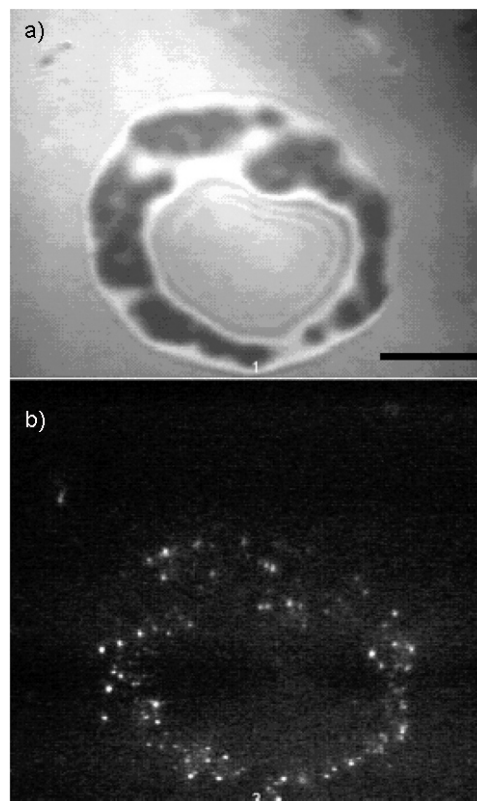


Figure 4.16. A vesicle labeled with the fluorescent RGD adhering onto a substrate coated with physisorbed integrin. a) RICM image of the vesicle. The dark part corresponds to the adhered part of the membrane. b) Fluorescence image: all fluorescent spots are localized in the contact zone. From [187].

b) Mobile Integrin incorporated into a Supported Lipid Bilayer

The experimental system was improved by spreading small vesicles bearing the integrin $\alpha_{IIb}\beta_3$ on ultrathin films of cellulose, forming a continuous supported lipid bilayer on the substrate [169]. Spreading the

integrin onto a cellulose cushion improved the protein functionality by reducing the contact between protein and surface. The functionality of the receptor on bare glass (system a) and on cellulose cushions was compared by measuring the adhesion strength of giant vesicles carrying the lipid-anchored RGD. The system was studied with fluorescence microscopy and RICM, and the free adhesion energy W was measured. The receptor-ligand binding energy was estimated to be $w_{I-RGD} \sim 10 k_B T$ under bioanalogous conditions. With a receptor density $n_I \sim 7 \times 10^{13} \text{ m}^{-2}$, the specific adhesion energy was then estimated to be $W_{ad} \approx n_I w_{I-RGD} \approx 3 \times 10^{-6} \text{ Jm}^{-2}$. According to figure 4.17, this is only 3 to 10 times larger than the largest spreading pressure Δg_{ad} found for vesicles containing 2 % and 3 % PEG lipids, respectively. It is 30 times larger than the largest value of Δg_{ad} found for vesicles containing 2 % of PEG on pure glass substrates (no cushion). (There is only a small discrepancy between Δg_{ad} and W_{ad} : $\Delta g_{ad} = W_{ad} - \Delta\pi_R - \Delta\pi_{Li}$, where $\Delta\pi_R$ and $\Delta\pi_{Li}$ are the osmotic pressure difference of the repellers and ligands, respectively. For details see [169].)

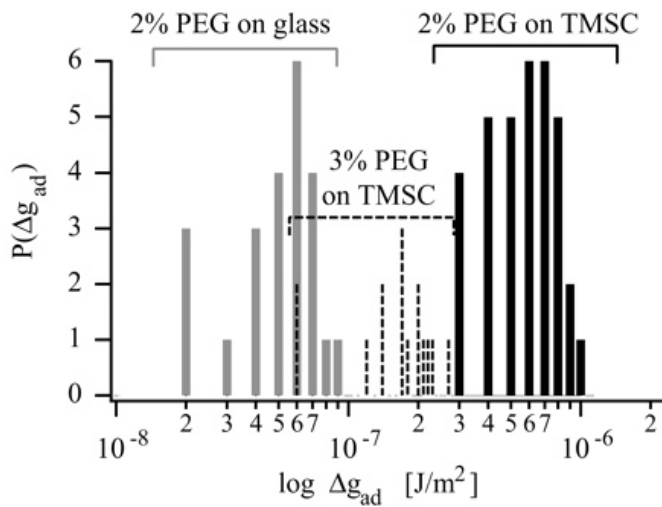


Figure 4.17. Histograms of measured values of free energies of adhesion Δg_{ad} of vesicles containing 2 and 3 mol % of repeller lipids (PEG lipids) on cellulose (black and dotted lines, respectively) and of vesicles containing 2 mol % PEG lipids on bare glass substrates (gray lines). The largest value correspond to regions of tight adhesion, whereas the lowest values correspond to the spreading pressures of the regions of weak adhesion. TMSC = trimethylsilyl cellulose. From [169]

Fluorescence microscopy showed heterogeneous and numerous dark patches in the case of physisorbed fluorescently labeled integrin, accounting for incomplete coverage of the surface (see image 4.18). In the improved

system with the cellulose cushion, the formed membrane was fluid and homogeneous and the integrin could diffuse over the surface.

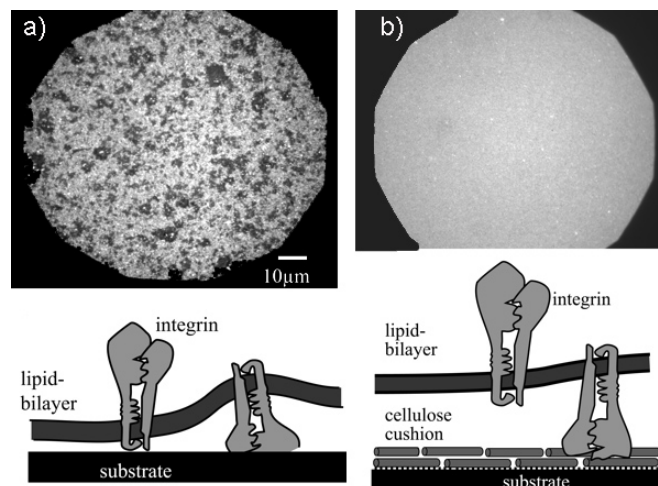


Figure 4.18. Fluorescently labeled integrin on the substrate a) Physisorbed integrin. The surface is heterogeneous with numerous dark patches are visible. b) Integrin incorporated into a SLB. The surface is homogeneous and the surface is fully covered by integrin. From [169].

The functionality of the integrin in the supported lipid bilayer (SLB) was tested with the help of RGD-binding tests. Fluorescently labeled RGD was incubated with the protein-containing SLB, rinsed, imaged with fluorescence microscopy to show that the RGD bound to the integrin in the SLB.

As mentioned before, the development of the RGD-integrin system in the group of Prof. Sackmann was crucial for the implementation of our own model system, as we benefitted from the group's expertise in membrane protein purification and handling. Their work inspired us to develop a system in which the integrin receptor was integrated in the vesicle membrane. This geometry more closely resembles the structure of a biological cell.

CHAPTER 5

The Minimal System

The group of Prof. Erich Sackmann at TU Munich developed the first experimental model systems using the transmembrane protein integrin to study cell adhesion [188], [168], [169]. From the vast family of adhesion proteins, they studied the specific interaction of the transmembrane protein integrin $\alpha_{IIb}\beta_3$ (described before, see chapter 2) with RGD. They decided to use this particular integrin since it is fairly easy to obtain, and most importantly, its biochemical and structural properties are very well characterized. To model the cell, giant unilamellar vesicles were employed as they comprise the basic structure of the cell envelope - the lipid bilayer. It is not easy to reconstitute transmembrane proteins into giant vesicles while preserving their biological functionality and at that time, the Sackmann group were unable to find a protocol for reconstituting integrin. Instead, they chose to functionalize the giant vesicle with RGD-lipids, and adsorbed the integrin to the surface (at first, directly and later via a 2D supported lipid bilayer - see figure 5.1). This provided an elegant proof of the functionality of the protein and experiments studying GUV spreading were then possible.

Nevertheless, their approach had several disadvantages:

- The integrin was in direct contact with the glass substrate, which altered its functionality.
- The geometry limited the range of possible experiments with the system. In a real cell, the integrin is not only in contact with the outside of the cell, but also receives signals from the inside and is directly connected to actin cytoskeleton via coupling proteins (see also chapter 2).

The experimental approach by the Sackmann group was a significant step towards the challenging goal of reconstituting integrin into GUVs. This goal was the first and most difficult objective of this thesis. More generally, this

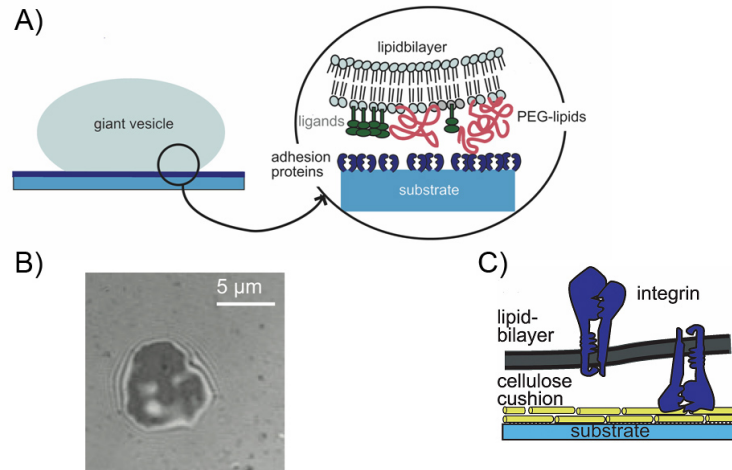


Figure 5.1. Model system of the Sackmann group, TU Munich. A) A schematic view of the system: A RGD-functionalized GUV adheres to an integrin covered surface. B) RICM image of the adhering vesicle. C) Schematic close-up of the integrin-containing bilayer. In the refined system, the integrin is protected by a cellulose layer from interactions with the glass substrate. From [189].

approach opens up numerous possibilities to bring model cells closer to the complexity of a biological system.

A Reconstitution of integrin $\alpha_{IIb}\beta_3$ into Giant Unilamellar Vesicles

A.1 General Scheme

Based on a method previously developed in the group of Prof. Bassereau [3], for the first time the transmembrane protein $\alpha_{IIb}\beta_3$ (described earlier) was successfully reconstituted into giant unilamellar vesicles (GUVs). First, the integrin $\alpha_{IIb}\beta_3$ was purified from human platelets (in collaboration with Dr. M. Bärmann, TU Munich, Germany) and then fluorescently labeled (for details see appendix C). The next step of the method involved the detergent-mediated reconstitution of solubilized membrane proteins into small proteoliposomes.

This process can be schematically summarized as follows (detailed protocols in appendix D):

a) Reconstitution of Integrin in SUVs The integrin is reconstituted into proteoliposomes following a general procedure described in references [190], [191]. The integrin is mixed with the lipid and a detergent (Triton). With the help of the detergent, which solubilizes the protein and the lipid, micelles

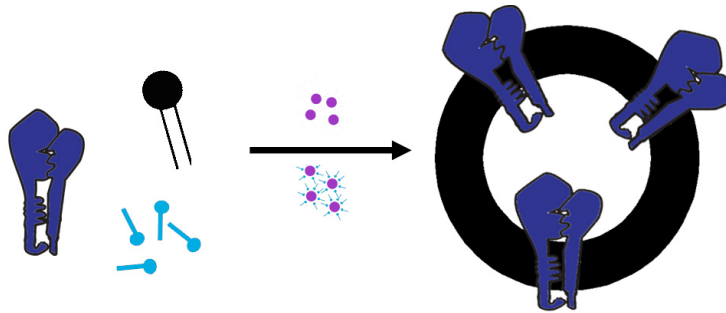


Figure 5.2. *The first step of the method involves the detergent-mediated reconstitution of solubilized membrane proteins into small proteoliposomes.*

containing all three components are formed. After removal of the detergent using biobeads®), vesicles form that contain only the integrin and the lipid. All reconstitution protocols used in the presented text require Biorad biobeads®) for detergent removal. These macroporous polymeric adsorbents of high surface area have to be activated by removing trapped air from the pores. This activation is crucial for correct functioning of the adsorbent. The use of these polystyrene beads to remove detergent is a highly reproducible way to generate unilamellar proteoliposomes. In addition, it allows quasicomplete removal (only traces of less than 1 % (sensitivity limit of the used technique, likely to be even less) can be found after treatment with biobeads®) of detergent [192]), which is important for GUVs since detergent destabilizes them [181]. When the detergent concentration diminishes, proteoliposomes consisting only of lipid and protein form spontaneously. The proteoliposomes are about 100 to 200 nm in diameter [188]. This technique for removing detergent from lipid-protein-detergent micellar solutions has been reported to be very efficient and suitable for the reconstitution of many membrane proteins [193].

With the help of electron microscopy, Hu et al. [188] showed that the integrin $\alpha_{IIb}\beta_3$ was indeed incorporated in the small proteoliposomes (see figure 5.3). Little is known about the orientation of the integrin in these small vesicles. In platelets, the sialic acid residues of integrin are oriented on the outside. Neuraminidase hydrolysis of sialic acid residues in intact and detergent-solubilized small vesicles showed that at least 55 % of the total sialic acid was accessible to neuraminidase in the absence of Triton X-100, indicating that 55% of the $\alpha_{IIb}\beta_3$ was oriented right-side out in the small vesicle, and, therefore, available for instance to bind to fibrinogen [194]. Methods like electron microscopy should provide further insight. It is probable that the majority are oriented in the "right way" (extracellular part outside) since the extracellular part of integrin is rather large and can induce curvature of the membrane. This has been shown in the case of other membrane proteins with a large extracellular portion (e.g. Ca^{2+} -ATPase for which ~ 80 % are oriented with their large cytoplasmic domain toward the outside [190]).

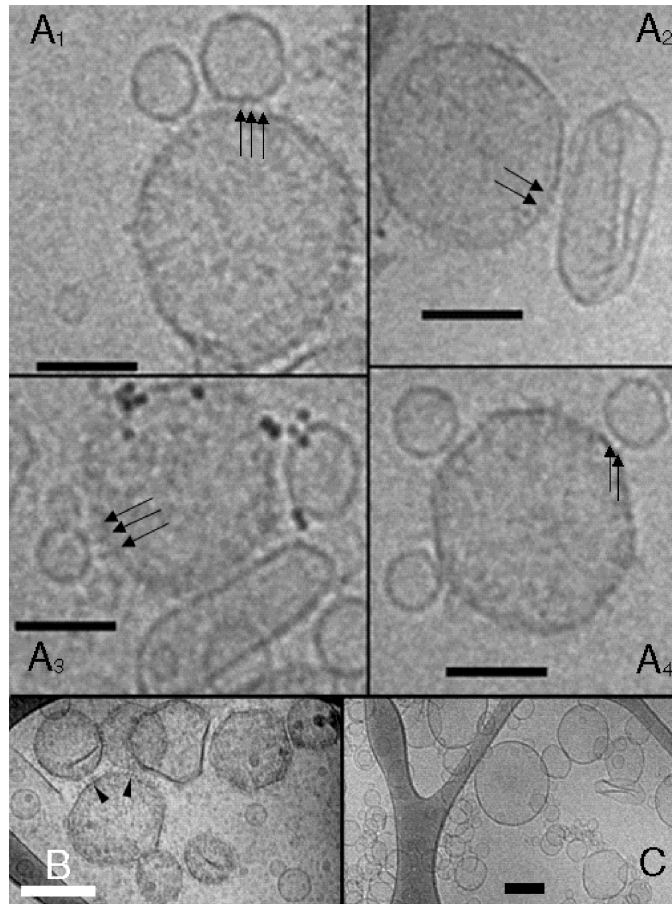


Figure 5.3. *A1 – A4: a series of cryo EM snapshots of a mixture of integrin vesicles and cRGD vesicles. Arrows point to integrin/RGD bridges between vesicles. Dark spots in panel A3: 5 nm gold particles. Magnification 31000 \times ; scale bars: 50 nm. B: a mixture of integrin vesicles with pure lipid vesicles (DMPC/DMPG = 1/1), scale bar: 200 nm. Arrowheads point to integrin/integrin attachments. C: a mixture of cRGD-vesicles with pure lipid vesicles as in B, scale bar: 200 nm. All but the 40 integrin-containing vesicles were produced by extrusion. Note that, for a better overview, B and C are shown at lower magnification than A1 –A4. The irregular dark objects in the upper right corner of B are artifacts of the preparation. From [188].*

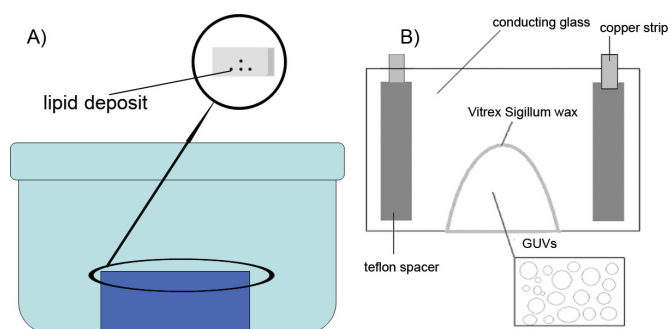


Figure 5.4. A) The droplets are dried under saturated atmosphere for up to 12h. B) Chamber for preparation of GUVs consisting of ITO-conductive glass slides, separated by a Teflon® spacer. A voltage is applied through two copper strips. GUVs form from partially dried droplets of proteoliposomes in contact with an aqueous sucrose solution.

b) Formation of Giant Unilamellar Vesicles (GUVs) using Electroformation In the second step, small droplets (1.5 μl each) of these preformed proteoliposomes are partially dried under controlled humidity on ITO treated glass slides. No vesicles grow from completely dehydrated (vacuum) droplets, probably because the integrin is denatured during the process. It has been shown that complete dehydration under high vacuum can have deleterious effects on the biological activities on other proteins as well [3]. Thus, it is essential to perform a partial dehydration of the proteoliposomes under controlled humidity (i.e. in the vapor from a saturated salt solution).

After the droplets have partially dried, the film is rehydrated in sucrose solution while exposed to an AC electric field (see figure 5.4, for detailed protocols see appendix D). The resulting are 10 - 100 μm in diameter.

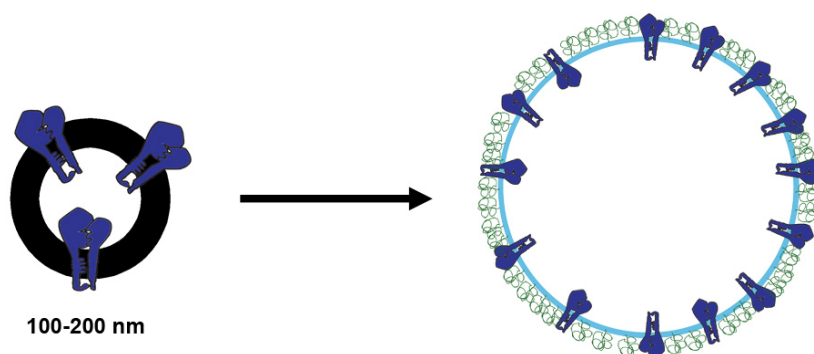


Figure 5.5. Integrin containing GUVs are formed from proteoliposomes by electroformation.

A.2 Challenges

A major challenge was to adapt the existing protocols to integrin $\alpha_{IIb}\beta_3$ so as to yield giant unilamellar vesicles larger than $15\ \mu\text{m}$. Two approaches existed:

1. Initial Paris Protocol

The general protocol developed by Girard et al. [3] for reconstituting other membrane proteins (bacteriorhodopsin and Ca^{2+} -ATPase) into GUVs.

2. Initial Munich Protocol

The protocol used in the Munich lab to prepare 2D-lipid bilayers containing integrin $\alpha_{IIb}\beta_3$ [188], [195].

(Proteo-GUVs and protein-containing lipid bilayers both use proteoliposomes for the initial step.)

These protocols did not produce vesicles, but rather multi-lamellar objects with non-spherical shapes and small size (see figure 5.6).



Figure 5.6. Phase contrast microscopy showing the multilamellar objects formed with the initial reconstitution methods (in this case the initial Paris protocol), bar = $10\ \mu\text{m}$.

After exhaustive testing and development, a *final protocol* was developed which led to large (larger than $15\ \mu\text{m}$ in diameter) unilamellar spherical vesicles.

The final, functional protocol as well as the two initial protocols are presented in the appendix D. Although, the differences between the final protocol and the initial ones may seem minor, these **small, apparently minor changes turned out to have a decisive effect on the effectiveness of the protocol.**

The parameters which appeared to be crucial for integrin reconstitution into GUVs are listed below:

1. The **lipid composition** of the vesicle was crucial for forming large, spherical, defect-free vesicles. In the original protocols, only zwitterionic lipids were used (phosphocholine, PC).
 - **Negatively charged** lipids have been reported to help in the protein reconstitution step [139] as well as in the activation of certain integrins [196]. Using L- α -Phosphatidic Acid (Egg, Chicken-Monosodium Salt, EPA) improved integrin incorporation as shown by adhesion tests. Control tests (same lipid composition without integrin) did not show unspecific adhesion under same conditions (see below). Note that using 1,2-dioleoyl-*sn*-Glycero-3-phosphoserine (DOPS), a negatively charged lipid, did not bring much enhancement (adhesion of vesicles in adhesion tests only rarely observed). Integrin GUVs were used in adhesion studies on biofunctionalized surface, as described below and in the next chapter.
 - **PEG-functionalized lipids** formed much larger vesicles and helped prevent unspecific adhesion. In the presence of divalent ions, vesicles without PEG lipids adhere with each other and with the surface, or burst (as visualized by RICM on the surface of the observation chamber). This result was previously shown by another group at Institut Curie,[197]. Steric repulsion due to the grafted PEG polymers is an efficient inhibitor of non-specific adhesion and helping prevent non-specific adhesion due to divalent ions [198]. PEG functionalized lipids have been used previously to mimic the glycocalyx of the cell [182]. Different PEG-lipids were tested and the length of the PEG-polymer (M.W. 2000, 3000, or 5000) was not found to be crucial. DOPE-PEG2000 (1,2-Dioleoyl-*sn*-Glycero-3-Phosphoethanolamine-N-[Methoxy(Polyethylene glycol)-2000]) lipid was replaced by DPPE-PEG2000 (1,2-Dipalmitoyl-*sn*-Glycero-3-Phosphoethanolamine-N-[Methoxy(Polyethylene glycol)-2000])lipid for its lower susceptibility to light and oxidation.

In order to distinguish specific adhesion events from non-specific interaction caused by divalent ions / negative charge on the lipids, all lipid compositions *without integrin* were tested under the same conditions (same buffers, same surfaces) as used later in the adhesion experiment. The adhesion of lipid vesicles was tested on a passivated surface (casein-covered cover slips) and an adhesive surface (fibrinogen-covered cover slips), in the presence of divalent ions, which are necessary for the functioning of the integrin.

Results for a range of lipid compositions are reported below:

Lipid	mol-%	Comment*
EPC	100	large vesicles, explosion and adhesion with divalent ions
EPC DOPE-PEG2000	95 5	very large vesicles, no or unfrequent explosion/adhesion with divalent ions
EPC DOPE-PEG2000	95 5	very large vesicles, no or unfrequent explosion/adhesion with divalent ions
EPC DOPE-PEG3000	95 5	very large vesicles, no or unfrequent explosion/adhesion with divalent ions
EPC DOPE-PEG5000	95 5	very large vesicles, no or unfrequent explosion/adhesion with divalent ions
EPC DPPE-PEG2000	95 5	very large vesicles, no or unfrequent explosion/adhesion with divalent ions
EPC EPA DMPE-PEG2000	85 10 5	very large vesicles, no or little explosion/adhesion with divalent ions

*EPC = L- α -phosphatidylcholine

explosion = vesicles explode, the membrane fragments can be observed on the glass surface by light microscopy

large = larger than 15 μm in diameter

adhesion = vesicles adhere to each other, or to the surface

Conclusion: As is evident from the table above, the composition 85 % EPC, 10 % EPA, 5% PEG2000 was best suited and was therefore used.

2. **The integrin/lipid ratio** proved to have a major influence on the GUV size and shape. Using high integrin (1 integrin per 1000 lipids or higher, equivalent to about 1000 integrins per μm^2) concentrations led to small (smaller than 10 μm in diameter) or non-spherical vesicles, often multi-lamellar in appearance as showed above (see figure 5.6). The initial Munich protocol uses about 20 times as much integrin as used in the initial Paris protocol (1 integrin per 1000 lipids) for other membrane proteins. However, even the concentration of the initial Paris protocol turned out to be too high.

The lipid/integrin ratio on platelets is 1000/1 while on other cell types 5.000-10.000 lipids are found per integrin [199]. Using a 1000/1 mixture yielded multi-lamellar object of different shapes.

Conclusion: Using a lipid/integrin ratio of 8000 lipids per integrin, equal to about 1000 integrins per μm^2 , (and within the biological range) yielded nice almost defect-free vesicles.

3. Furthermore, Munich and Paris protocols differ in the **reconstitution temperature**: (Munich: 15 and 37 °C, Paris: room temperature). Final reconstitution was performed at room temperature. As shown by Levy and Rigaud [190], [191], many proteins are stable at room temperature in the presence of detergent.

Conclusion: Reconstitution was performed at room temperature.

4. The **duration of exposure to biobeads** is another crucial factor (Munich: 1h, Paris: at least 3h). In the final protocol, this step was prolonged and biobeads® were stirred overnight to improve the removal of detergent. GUVs with a diameter of 20-70 μm were obtained, confirming the absence of detergent in the final state.

Conclusion: The reconstitution solution was exposed to biobeads overnight.

5. The **duration of the electroformation process** was lengthened from the 4h period of the initial Paris protocol to overnight (12h). Increasing the growth period mainly changed the size of the vesicles and larger vesicles could be obtained.

Conclusion: Electroformation was extended to an overnight process.

6. **Aging of the integrin solution** heavily influenced the quality of obtained GUVs. Reconstitutions with freshly purified integrin yielded almost defect-free vesicles, while aged integrin led to multilamellar non-spherical objects. Generally, six months after purification, no vesicles could be obtained. It was furthermore documented [200] that integrin $\alpha_{IIb}\beta_3$ showed heavily reduced activity as shown through the activity test ELISA. Storage temperature was also crucial. While -70 °C and 0 °C did not influence the integrin's activity, storage at -20 °C reduced its activity by 30% independent of previous shock freezing in liquid nitrogen.

Conclusion: Integrin was used only within 5-6 months after purification and stored at -70 °C.

Finally, it has to be noted that reliability of vesicle growth protocol was a major issue. Frequently, the protocol would not yield vesicles and this could last for a period of a few weeks. Detailed experimentation analysis of the likely factors did not reveal the cause of this variability.

A.2.1 Other Tested Procedures

A.2.1.1 Influence of Sucrose during Reconstitution Doeven et al. [139] reported that addition of sucrose during the dehydration step of the GUV-

formation process prevented four distinct membrane protein(s) (complexes) from inactivating. They optimized the amount of sucrose so that the proteins retained 100% biological activity, and many proteo-GUVs were obtained. Depending on the protein, as little as 20 mg sucrose/g of lipid was sufficient to retain full activity. In their protocol, sucrose is added to the SUV solution which is then dehydrated in vacuum. This protocol did not work for integrin containing GUVs and either no GUVs were obtained, or the small numbers of GUVs obtained did not adhere onto the surface in adhesion assays.

A.2.1.2 The Effect of Divalent Ions on the Growth of Vesicles

The biological function of the integrin complex $\alpha_{IIb}\beta_3$ (see chapter 2.1) depends on divalent ions, mainly Mg^{2+} , Ca^{2+} and Mn^{2+} and it would be desirable to add these ions to the sucrose solution in the growth chamber. However, the presence of divalent ions inhibited vesicle growth via electroformation.

The following growth buffer solutions were tested:

Composition	Buffer	Result
100 mol% DOPC	buffer A* 1mM Ca^{2+}	no vesicles
100 mol% DOPC	buffer A* 1mM Ca^{2+} 119 mM sucrose	no vesicles
100 mol%DOPC	180 mM sucrose 1mM Ca^{2+} 2 mM KCl	no vesicles
85 mol% EPC 10 mol EPA% 5 mol% DMPE-PEG2000	180 mM sucrose 1mM Mg^{2+} 1 mM Mn^{2+}	no vesicles
100 mol%DOPC	180 mM sucrose	unilamellar, spherical vesicles,
85 mol% EPC 10 mol EPA% 5 mol% DMPE-PEG2000	180 mM sucrose	large, spherical vesicles,

* buffer A:

pH 7.4

150 mM NaCl

10 mM Tris

A.3 Summary

A mixture of EPC, EPA and DMPE-PEG2000 lipid yielded spherical, mainly uni-lamellar vesicles (see figure 5.7.)

- EPA was introduced to improve integrin incorporation into vesicles.
- PEG2000 lipids were used to screen non-specific attraction induced by divalent ions.
- The integrin concentration was lowered, but was within biological concentrations found on cells.
- Biobeads® were incubated all night in order to fully remove the detergent.
- The electroformation process was prolonged in order to obtain larger vesicles.
- Integrin was used less than 6 months after purification

The following image shows vesicles obtained using the improved protocol:

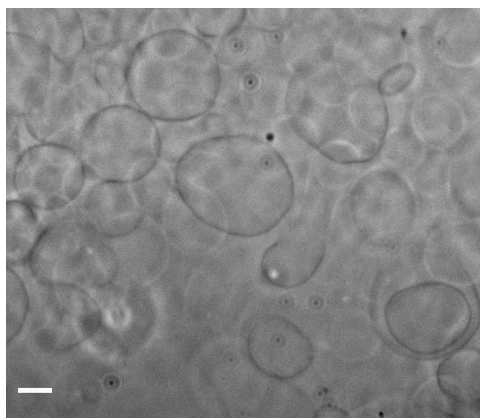


Figure 5.7. *Integrin proteoliposomes formed using a mixture of EPC, EPA and DMPE-PEG2000 were predominantly spherical and uni-lamellar. Phase contrast microscopy, bar = 10 μ m.*

A.4 GUVs from Native Membranes

A second approach to form GUVs containing integrin $\alpha_{IIb}\beta_3$ was also examined. Since integrin $\alpha_{IIb}\beta_3$ is the most abundant protein on platelets, the strategy was to purify the platelet membrane and to grow GUVs from this

natural lipid-integrin mix. For detailed protocol see appendix C. Such a membrane purification is also likely to preserve some of the proteins which link the integrin to the actin cytoskeleton (for details see chapter 2). These linking proteins could facilitate the extension of the model system (e. g. the incorporation of actin cytoskeleton into the GUVs).

Membrane was purified following a protocol by Smyth et al. [201]. Electroformation of the obtained membrane solution did not produce vesicles. However, by diluting the obtained membrane solution with the purification buffer, vesicles could be obtained (see figure 5.8).

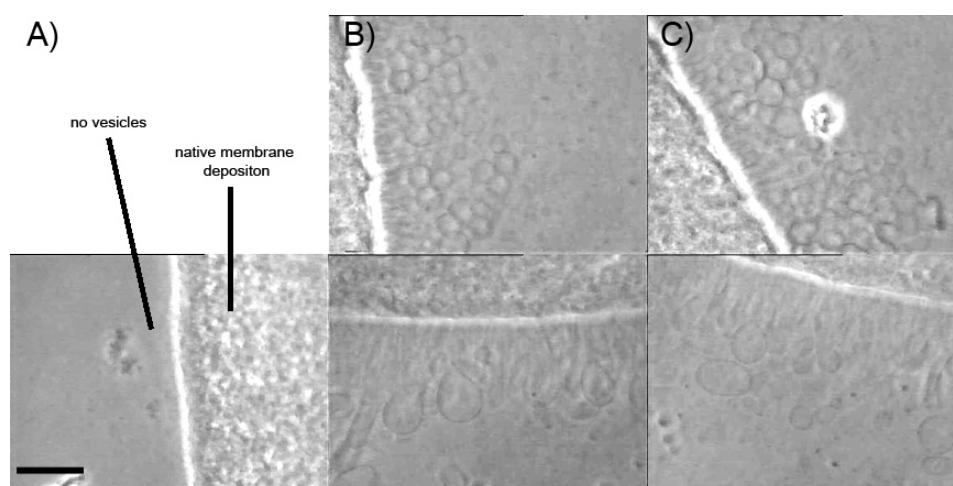


Figure 5.8. Formation of GUVs from native membrane (growth chamber). A) The undiluted membrane solution does not produce vesicles. B) diluting the obtained membrane solution before electroformation leads to vesicles (dilution with buffer 1:1 in volume). C) dilution with buffer 1:5 in volume. Phase contrast image, bar = 10 μm .

Despite these promising results, this approach was abandoned because there was no access to sufficient amounts of outdated* platelets in France as well as insufficient infrastructure for membrane purification at the Institut Curie. However, this approach seems to be a very promising way to obtain integrin- covered GUVs with a biological composition, especially since some of the linker proteins to the cytoskeleton might be retained.

*Outdated platelets are too old for transfusion. For experiments, platelets are used within 14-21 days after venipuncture.

B Incorporation and Functionality

The reconstitution process was validated by analyzing protein incorporation and biological activity.

B.1 ELISA-Test on Integrin-Containing SUVs

The activity of the integrin after reconstitution and after electroformation was tested with the help of qualitative Enzyme-Linked Immunosorbent Assay (ELISA). The test consisted of checking the capacity of a specific anti-human β_3 antibody to bind to integrin $\alpha_{IIb}\beta_3$, which then reacted with a second labeled antibody. A positive test, corresponding to active integrin, occurred when the final solution turned yellow. The detailed protocol can be found in appendix C. A solution of SUV reconstituted integrin was checked. Secondly, in order to obtain the same integrin concentration for ELISA after electroformation, the effect of electroformation was mimicked by exposing the same volume of integrin-containing SUVs to an electric field for 12 h (see figure 5.9). The results of the ELISA tests were compared. Qualitatively, no difference in activity was observed as both samples (before and after exposure to electrical field) showed approximately the same color intensity.

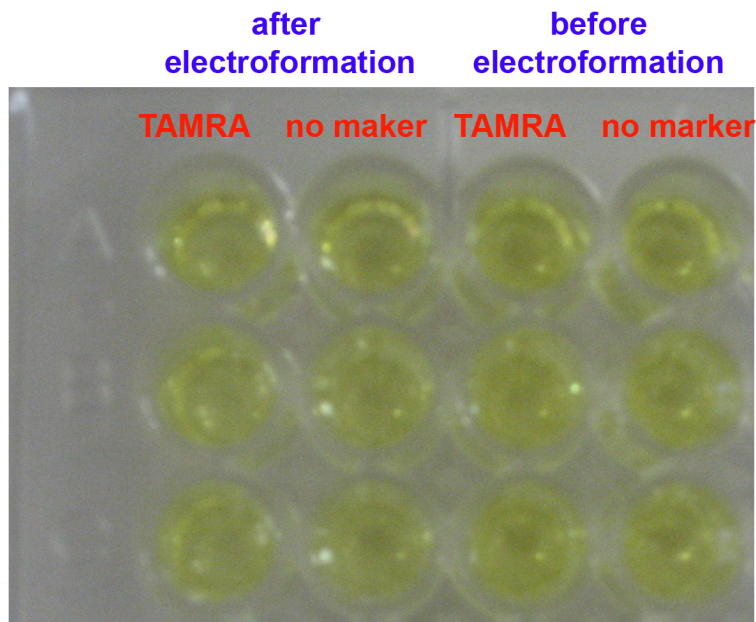


Figure 5.9. *ELISA test. Effect of electric field on the integrin activity.*

Conclusion: The integrin retains its activity after electroformation.

B.2 Confocal Microscopy

Confocal microscopy showed that the fluorescently-labeled protein were incorporated into the membrane.

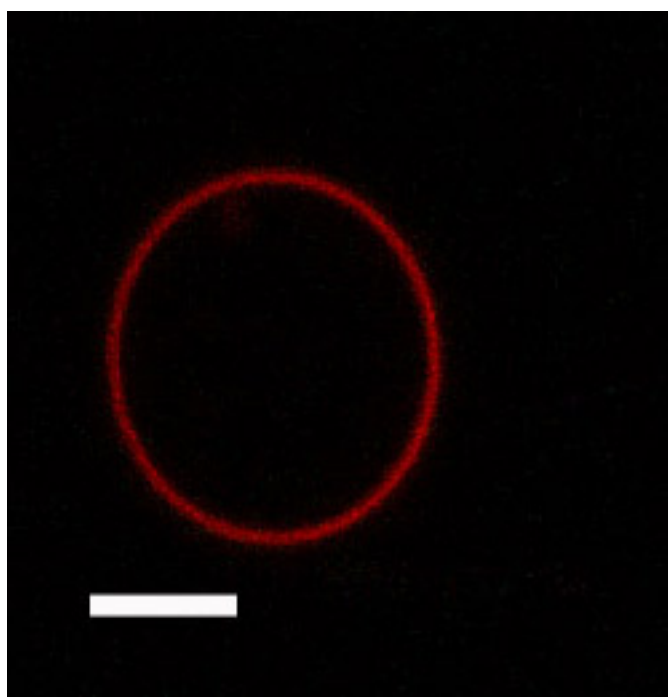


Figure 5.10. *Confocal image of the membrane of a GUV in which 5% of the integrins are labeled with a TAMRA-label, bar 10 μm . The elliptic shape of the vesicle is due to the scanning speed of the confocal microscope.*

Incorporation was homogeneous with no clustering of integrins (see figure 5.10). The integrin was labeled with 5(6)-TAMRA, a rhodamine derivate, which fluoresces at red wavelengths (emission maximum = 576 nm). 5% of the total integrins was labeled.

Conclusion: The integrin was present in GUVs as shown by confocal images.

B.3 Quantum Dots Assay

The activity of integrin $\alpha_{IIb}\beta_3$ was further tested through interaction assays with functionalized quantum dots (QDs) carrying an RGD- tripeptide or a PEG-sequence. Functionalized quantum dots were kindly provided by the group of V. Marchi-Artzner, University of Rennes.

Two types of PEG- functionalized QDs were provided. One type was terminated by a negative charge while the second was terminated with a zwitterionic endgroup. The QDs had an emission maximum wavelength of 603 nm

(red). The hydrodynamic diameter of the QDs was 15 nm (RGD), and 11 nm (EO₆D), respectively. The chemical formulas are shown in figure 5.11. QDs were stored in a borate buffer at pH 8.3.

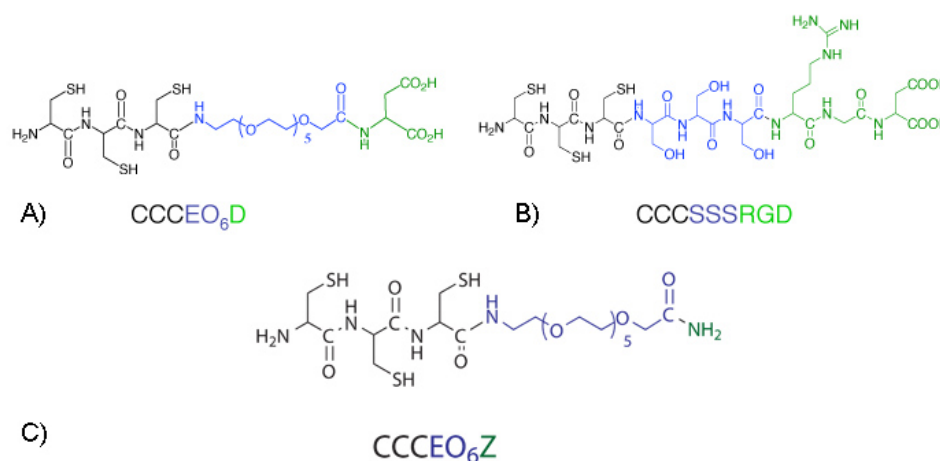


Figure 5.11. The functional group on the QDs - A) negatively charged PEG, B) RGD, C) the zwitterionic group. Private communication A. Dif / V. Marchi-Artzner.

To determine if the RGD-tripeptide was recognized by the integrin on the giant vesicle both fluorescence microscopy and spectrofluorimetry were performed. For fluorescence microscopy, only the results from platelets (Integrin $\alpha_{IIb}\beta_3$ is the most abundant protein on platelets) are shown here. The experiments on GUVs containing the integrin $\alpha_{IIb}\beta_3$ are still underway. For spectrofluorimetry, assays were performed on proteoliposomes and platelets.

B.3.1 Fluorescence Microscopy on Platelets

Two samples were prepared. Platelets were mixed with either RGD-QDs or negatively charged PEG-QDs and then observed in epifluorescence microscopy (A green filter ($\lambda_{exc} = 525$ nm, $\lambda_{em} = 565$ nm) was used.) (detailed protocol in appendix F). Fluorescence images showed that the RGD quantum dots rapidly bound to the platelet membrane (see figure 5.12). In contrast, the unexpected binding of the PEG-QDs could have resulted from nonspecific interaction between the negative charge on the PEG-group and the protein on the platelets.

Conclusion: These experiments show that the RGD-QDs are able to interact specifically with the integrin $\alpha_{IIb}\beta_3$ on platelets.

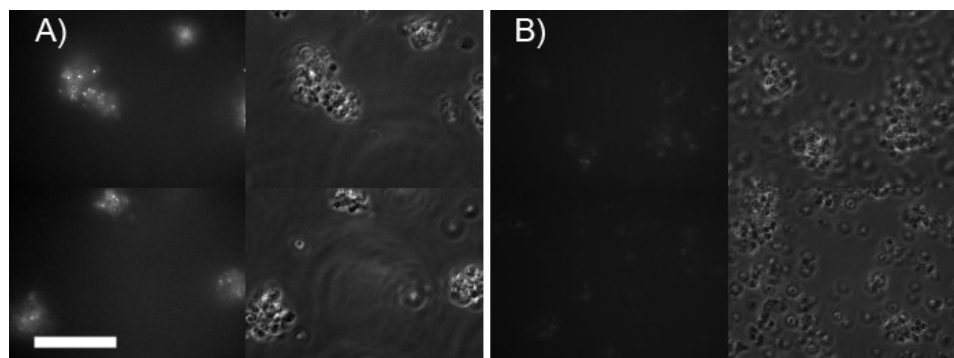


Figure 5.12. A) RGD-QDs (50 % RGD) are immediately visible on platelets, images after 5(left) and 20(right) minutes. B) Platelets incubated with PEG-functionalized QDs after 5(left) and 20(right) minutes. Epifluorescence image, bar = 10 μm .

B.3.2 Spectrofluorimetry on Platelets

As it was difficult to quantify the fluorescence on platelets and GUVs using epifluorescence microscopy, a second quantitative technique, spectrofluorimetry, was used. Platelets were incubated for 15 minutes with QDs (either PEG- or RGD-functionalized QD), unbound QDs were removed by centrifugation (for detailed protocols see appendix F) and the concentration of the bound QDs was then measured via spectrofluorimetry.

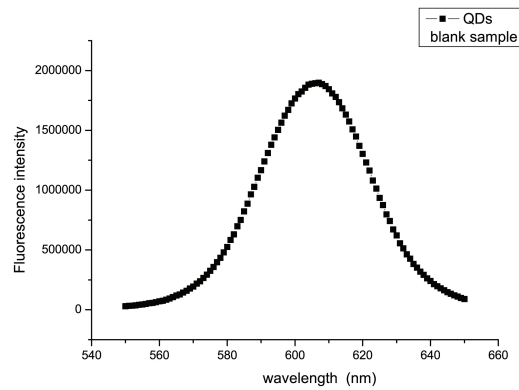
Several samples were prepared:

1. A blank sample containing only QDs in HEPES buffer
2. Platelets + RGD-QDs (50 % functionalized)
3. Platelets + negatively charged PEG QDs

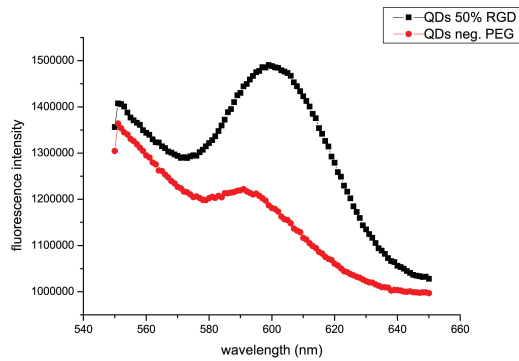
Fluorescence was excited ($\lambda_{exc} = 360 \text{ nm}$) and the fluorescence intensity was measured as a function of emission wavelength. Figure 5.13 shows fluorescence intensity as a function of wavelength for all three samples.

As can be seen from the graph, although the negatively charged PEG-functionalized QDs interact with the platelets, the fluorescence from RGD-carrying QDs is much stronger. This confirms the specific interaction between the RGD-carrying QDs and the integrins on the platelet surface.

Conclusion: The spectra showed that the interaction of platelets with RGD-functionalized QDs is much stronger than their interaction with PEG-functionalized QDs.



(a) Blank sample



(b) Platelets

Figure 5.13. A) Fluorescent spectrum from a blank sample of QDs (50 % RGD, 16 nM) in HEPES buffer. B) Fluorescence spectrum of platelets incubated with a) 50 % RGD QDs, b) neg. PEG QDs

B.3.3 Spectrofluorimetry on Proteoliposomes

Samples were prepared (200 nM QDs in solution) with:

1. A blank sample containing only QDs in HEPES buffer
2. Proteoliposomes (SUVs) + RGD QDs
3. Proteoliposomes (SUVs) + zwitterionic PEG QDs
4. Lipid mix w/o integrin (SUVs) + RGD QDs
5. Lipid mix w/o integrin (SUVs) + zwitterionic PEG QDs

The proteoliposomes or liposomes were incubated for 5 minutes with the QD solution. Unbound QDs were then removed via ultra-centrifugation on a sucrose gradient. First, the liposome / proteoliposome solution was mixed with a 60 % sucrose solution to a final volume of 1 ml. This was transferred to a centrifuge tube and a sucrose gradient prepared by carefully layering on top first 6 ml of 40 % sucrose solution, then 3.5 ml of a 5 % sucrose solution. After centrifugation (12 hrs, 4 °C (for detailed protocol see appendix F), a white band containing the proteoliposomes / liposomes formed at the interface of the 5 % and the 40 % solution. This fraction was extracted and the fluorescence emission spectrum measured ($\lambda_{exc} = 360$ nm).

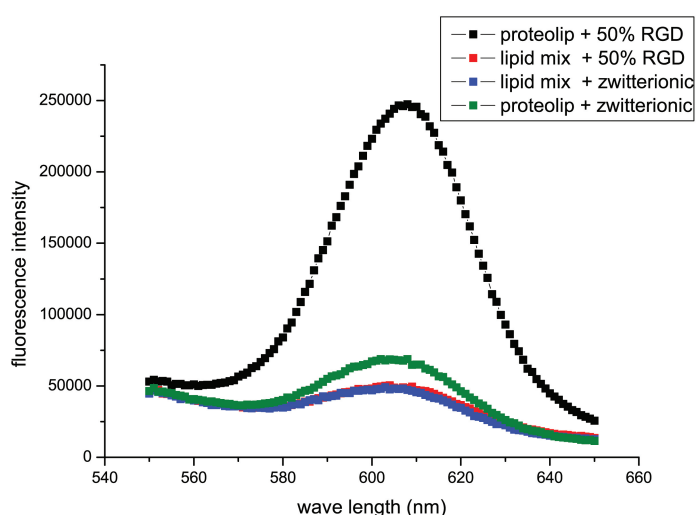


Figure 5.14. Fluorescence from the sample containing proteoliposomes + RGD-QDs is much higher than from the other prepared samples, indicating the specific recognition of the RGD-peptide by the integrin $\alpha_{11b}\beta_3$

As can be seen from the graph (figure 5.13B), the integrin in the proteoliposomes interacted with the RGD-functionalized QDs, while practically no fluorescence was observed in the proteoliposome- PEG-functionalized QDs mix. The PEG-functionalized QDs did not interact with either the pure lipid mix or with the proteoliposomes.

Thus the RGD-QDs specifically interact with the integrin containing proteoliposomes, confirming that the integrin is still active at this stage of the reconstitution.

Conclusion: QD assays using epifluorescence and spectrofluometry confirm that RGD-QDs specifically interact with the integrin on platelets and on proteoliposomes. The integrin was able to recognize the RGD motif, indicating that the protein was still active in the proteoliposome preparation.

B.4 Adhesion Tests

To further test the functionality of integrin $\alpha_{IIb}\beta_3$ after reconstitution and electroformation, adhesion studies were performed using passivated and bio-functionalized solid substrates.

B.4.1 Passivated Surfaces

As a control, two types of passivated surfaces were prepared

- a glass surface coated with grafted PEG polymers
- a glass surface coated with physisorbed casein

These two types of surfaces were used to limit protein interaction between the protein and the substrate [153], [202].

B.4.1.1 PEG-Coated Surfaces Glass substrates were silanized and PEG polymers grafted on top of them (detailed protocols in appendix E). Contrary to expectations, integrin-containing vesicles adhered to the surface (see figure 5.15).

As a control, vesicles without protein were prepared, and adhesion was again observed (see figure 5.16). Furthermore, vesicles containing neither integrin nor PEG lipids also adhered (see figure 5.17).

The same experiments were repeated in a buffer **without** divalent ions, and **no adhesion** was observed for both the integrin-containing vesicles and the pure lipid vesicles.

These results are somewhat surprising since PEG polymers are widely used to inhibit unspecific interactions and protein adsorption. However, other examples of ambiguous PEG behavior have been reported [203], [204], [205], although not for cell adhesion. It might be that cells in adhesion studies are less sensitive to electrostatic interaction with polymer-complex ions, because

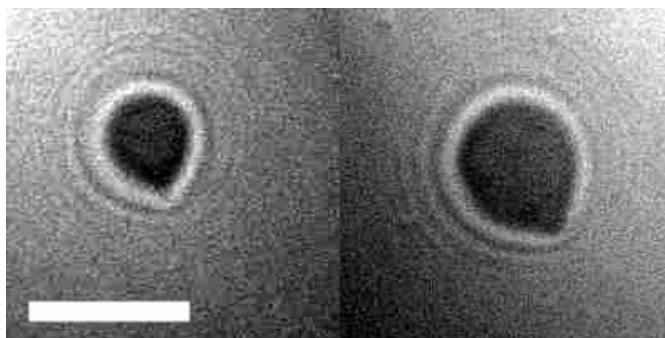


Figure 5.15. *Integrin containing vesicles adhering to a PEG-coated substrate in the presence of divalent ions. Bar = 10 μm , RICM image.*

cells are protected by their own polymer coat (glycocalix). Furthermore, in studies on biological *model* systems like GUVs "simple" buffers are often used which do not contain divalent ions. Therefore, electrostatic interaction with PEG-chains may not have been significant in earlier studies. However, it has been shown that PEG can become charged in the presence of mono- or divalent ions leading to interaction in biological systems (private communication B. Desbat and [203], [206]) It would be interesting to explore this question further in order to establish effective passivation techniques for sensitive model systems.

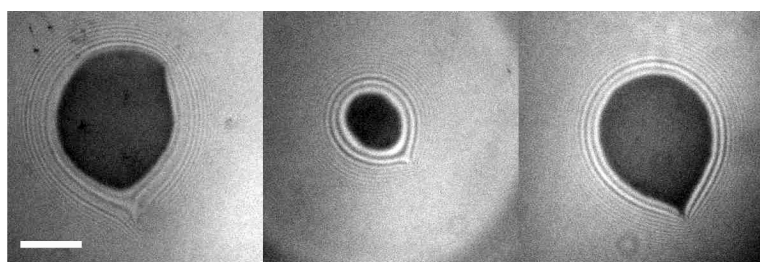


Figure 5.16. *GUVs containing PEG lipids, but no integrin, adhere to a PEG surface in the presence of divalent ions. Bar = 10 μm , RICM image.*

The following table summarizes the results of these adhesion studies.

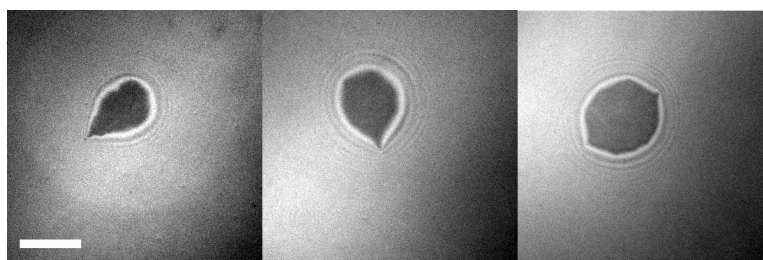


Figure 5.17. GUVs without PEG or integrin adhere to a PEG-coated surface in the presence of divalent ions. Bar = 10 μm , RICM image.

Lipid	mol-%	buffer composition	Comment
EPC DOPE-PEG2000	95 5	buffered glucose*	vesicles adhere to surface
EPC DOPE-PEG2000 integrin $\alpha_{IIb}\beta_3$	95 5	buffered glucose*	vesicles adhere to surface
EPC	100	buffered glucose*	vesicles adhere to surface
EPC DOPE-PEG2000	95 5	pure glucose	no adhesion
EPC DOPE-PEG2000 integrin $\alpha_{IIb}\beta_3$	95 5	pure glucose	no adhesion
EPC	100	pure glucose	no adhesion

buffered glucose

pH 7.4

180 mM glucose

10 mM TRIS

1 mM Mg^{2+}

1 mM Mn^{2+}

*buffered glucose:

As can be seen from the table, adhesion on PEG-coated surfaces is independent of the presence of integrin or PEG-lipids on the vesicle and depends only on the presence of divalent ions in the buffer solution. After making this discovery **PEG-coated substrates were no longer used in this study.**

B.4.1.2 Casein-Coated Surfaces Casein was found to be suitable for preparing passivated surfaces. First, an observation chamber with a casein-covered surface was prepared and the chamber was filled with HEPES buffer of pH 7.4, which has been proven to help the integrin to retain its functionality. Furthermore, divalent ions (2 mM Mg^{2+} , 2 mM Mn^{2+}) necessary for the correct functioning of the integrin were also present in solution [16]. Integrin-containing GUVs injected (for preparation details see appendix E).

RICM showed that integrin containing GUVs, even in the presence of divalent ions, did not spread onto the surface coated with casein.

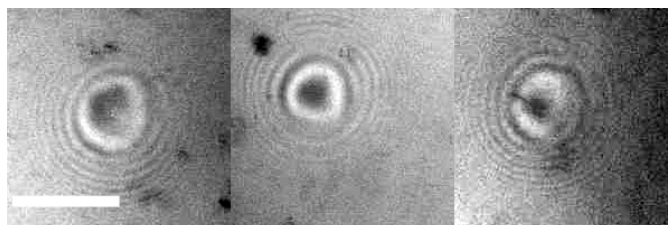


Figure 5.18. No adhesion was observed on casein-coated substrates, even in the presence of divalent ions. Bar = 10 μm , RICM image.

Conclusion: No unspecific adhesion was detected on casein-coated substrates. Casein-coated surfaces were therefore used as passivated substrates.

B.4.2 Adhesive Surface

Fibrinogen, an RGD-carrying protein, is the natural ligand to integrin $\alpha_{IIb}\beta_3$ in platelets and was therefore used to functionalize surfaces for adhesion tests. In principal, an active integrin correctly incorporated into the membrane of a GUV should be able to recognize its RGD-ligand on a surface. Accordingly, an observation chamber with a fibrinogen-functionalized surface was prepared and integrin-containing GUVs injected (for preparation details see appendix E). As for the studies with casein-coated substrates, the chamber was filled with HEPES buffer of pH7.4.

Integrin-containing vesicles adhered and spread on the fibrinogen-covered surfaces (see figure 5.19(a)), whereas no adhesion was observed on the passivated, non-adhesive surface coated with casein (see figure 5.19(b)).

Thus, **integrin $\alpha_{IIb}\beta_3$ retains its biological activity after reconstitution and electroformation as demonstrated by adhesion test onto surfaces covered with fibrinogen**, an RGD-carrying ligand of integrin $\alpha_{IIb}\beta_3$.

B.4.3 Adhesion Assay in the Presence of Soluble RGD

To prove that the adhesion of integrin-containing GUVs on RGD-covered surfaces originated from specific interactions with the fibrinogen coated surface, vesicles were incubated with soluble RGD before exposure to the fibrinogen surface. RGD in solution can interact with the integrin on the vesicle, thereby blocking interactions with the substrate. For these conditions, integrin was not able to adhere to the surface, indicating that a most of the integrin receptors were occupied by soluble RGD in solution (see figure 5.20)

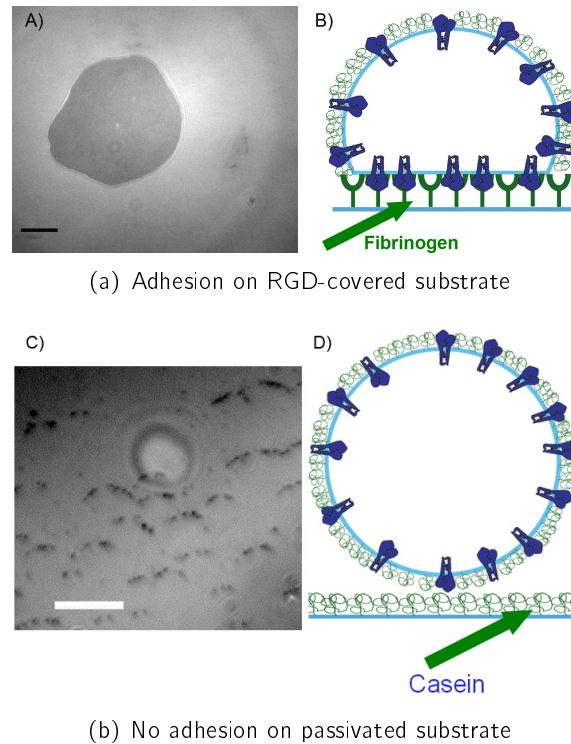


Figure 5.19. Adhesion tests. A) Adhesion of an integrin-covered GUV to an RGD-covered surfaces (fibrinogen). The vesicle was fully adhered after 22 minutes. Bar = 10 μm , RICM image. B) Schematic of the adhesion system. C) No Adhesion of integrin GUVs is observed on passivated surfaces (casein). Bar = 10 μm , RICM image. D) Schematic of the process.

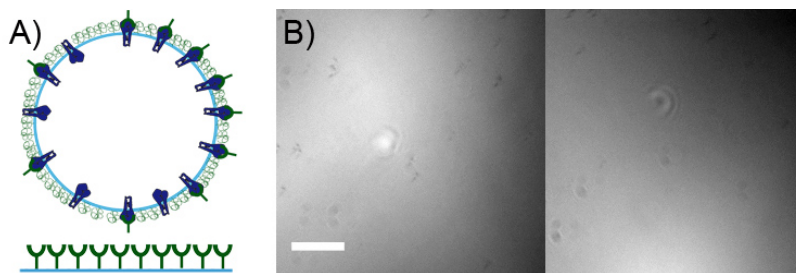


Figure 5.20. A) Schematic drawing: Integrin-GUVs are incubated with soluble RGD. Soluble RGD interacts with the integrin receptor on the GUVs, thereby inhibiting integrin interaction with the RGD on the glass substrate. Integrin-containing GUVs do not adhere to Fibrinogen-covered surfaces. B) Corresponding RICM image with free RGD in solution, bar = 10 μm .

Conclusion: RGD-containing GUVs adhere specifically to fibrinogen covered surfaces, while they do not interact with passivated, casein-coated surfaces. Furthermore, in the presence of soluble RGD, which should block the integrin receptors on the GUVs, the GUVs do not adhere to fibrinogen covered surfaces. Thus the integrin is still **biologically active after the electroformation process**.

C Conclusion

The developed preparation protocol efficiently reconstitutes integrin $\alpha_{IIb}\beta_3$ into giant unilamellar vesicles. **Incorporation** was proven by confocal microscopy. Integrin maintains its biological **functionality** as shown by

- spectrofluorimetry using RGD-functionalized quantum dots
- adhesion experiments on RGD-covered surfaces
- adhesion experiments on RGD-covered surfaces in the presence of soluble RGD

This is the first time that such a biomimetic system has been successfully prepared. In the next chapter, the spreading kinetics of these biomimetic GUVs on fibrinogen-coated surfaces will be discussed and compared to results of the biomimetic system studied by P.-H. Puech [179].

A Adhesion Dynamics: First Observations

Using the previously described reconstitution protocol, it was possible to prepare giant unilamellar vesicles containing integrin $\alpha_{IIb}\beta_3$ with diameters between 5 and 60 μm in diameter. Confocal microscopy showed that the fluorescently labeled integrin was **incorporated** and that the integrin retained its **functionality** (QD assays, adhesion tests).

The integrin-containing vesicles **specifically adhere** not only adhered to biofunctionalized substrates in adhesion tests (see figure 6.1), but also showed **reproducible adhesion dynamics**. This allowed us to study the **spreading mechanism** described in this chapter.

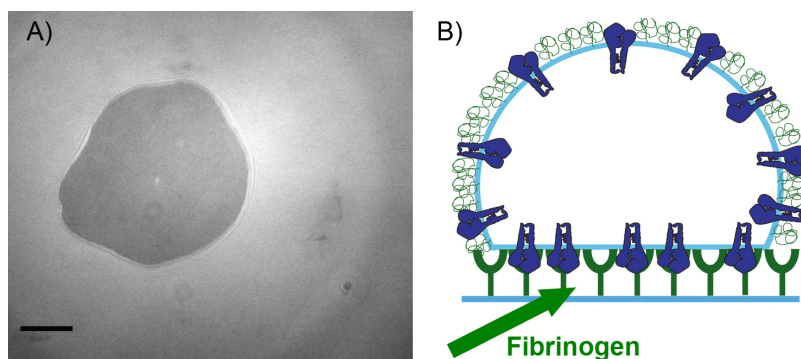


Figure 6.1. A) Adhesion of an integrin GUVs on an RGD-covered surfaces (fibrinogen). The vesicle was fully adhered after 22 minutes. Bar = 10 μm , RICM image. B) Schematic drawing of the adhesion process: The integrins on the GUV adhere to the fibrinogen adsorbed to the glass surface.

Figure 6.2 shows the sequence of steps during a typical adhesion event observed in reflection interference contrast microscopy (RICM):

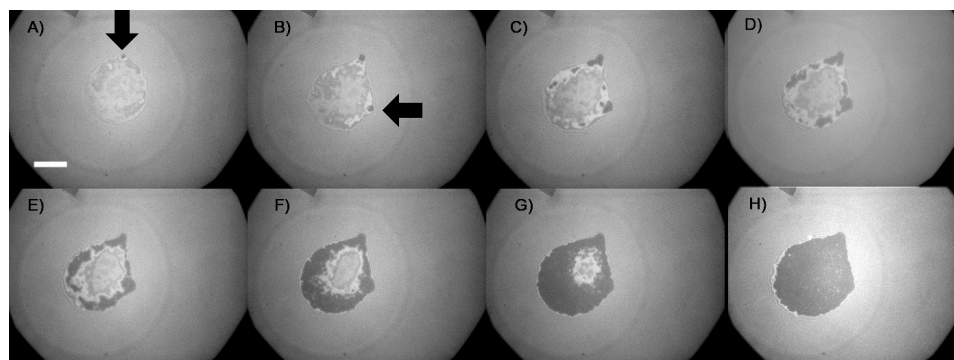


Figure 6.2. Image sequence of an integrin-containing vesicle adhering onto a fibrinogen covered surface. Images taken after A) 0, B) 1, C) 2, D) 3, E) 4, F) 7, G) 12, H) 22 minutes (RICM technique). Image A) and B): single adhesion patches appear. Image C)-E): the patches grow and fuse. Image F) and G): A ring-shaped adhesion patch is formed and grows toward the center until in Image H) the adhesion zone appears homogeneous. Bar = 10 μm

After injection, individual vesicles sedimented onto the fibrinogen surface. A circular region at the bottom of the vesicle then fluctuated within a distance of a few μm above the surface. This fluctuating circular region (see figure 6.2A) determined the part of the vesicle that was already fairly close to the surface (contact zone). A first contact was established at the rim of the contact zone (see figure 6.2B) as is evident in RICM. More attachment points followed which were all located in the same zone (figure 6.2C). These adhesion patches grew (figure 6.2D-E), eventually fused and formed a closed adhesion ring at the border of the contact zone (see figure 6.2F). The transition from adhering ring to homogeneous adhesion disk (figure 6.2I-H) typically took about 10 minutes although the exact rate depended on the size of the vesicle (small vesicles adhered faster). Interestingly, the adhesion dynamics went at a similar rate to the spreading dynamics of cells. Eventually, after longer times (30 - 60 minutes) blisters occasionally appeared in the middle of the (previously homogeneous) adhesion zone (see image 6.3). As this occurred infrequently, it will not be discussed further and the analysis concentrates on the spreading dynamics.

From the image sequence in figure 6.2, it is apparent that the adhesion dynamics can be separated into three essential steps:

1. Formation of single adhesion patches

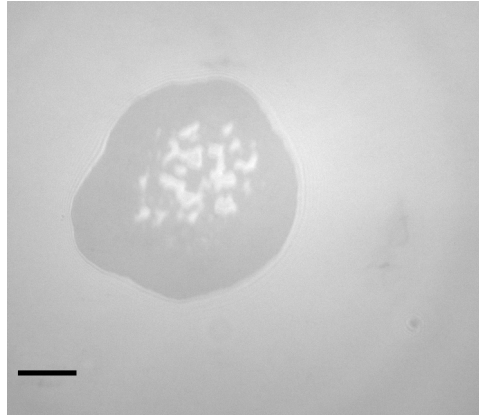


Figure 6.3. After longer times (30 - 60 minutes) blisters sometimes appear in the middle of the (previously homogeneous) adhesion zone. Bar = 10 μm , RICM image.

2. Coalescence of single patches and ring formation
3. Ring to disk transition

The variation of the total area with time (see figure 6.4) had a complex behavior due to the fusion of patches. The total area corresponds to the sum of the black area (= adhesion zone of each image). The three regimes cannot be clearly distinguished.

To resolve the individual steps during adhesion, the area of individual adhesion patches was analyzed as a function of time (see figure 6.5). The total area, representing the sum of the area of all the individual adhesion patches, was plotted for comparison. A systematic, approximately linear, increase is evident for each curve. This linear growth was hidden in the plot of the total area because of fusion events between patches.

After the individual patches fuse to form a ring, the adhered area continues to grow thereby converting the adhesion ring to an adhesion disk at longer times. To understand this change, the outer and inner perimeters of the adhesion ring were plotted as a function of time (see figure 6.6).

At the moment of ring formation, the outer perimeter is smaller than the sum of the perimeters of the single adhesion patches and it remains roughly constant at longer times. As soon as the ring formed, an inner perimeter could be defined. The inner perimeter decreased linearly with time as the adhesion zone extended towards the center.

The dynamics of the formation of single patches and the adhesion disk will be compared with theoretical predictions in the following section. The intermediate state, where some patches have fused and others have not is complex and will not be discussed.

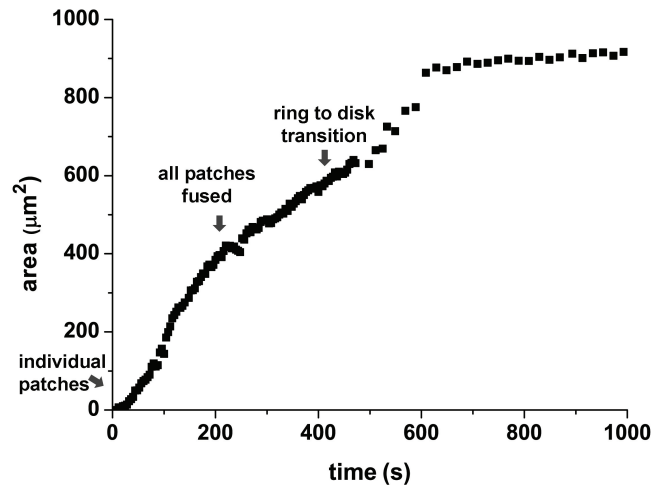


Figure 6.4. Growth of the total adhesion area with time. The three consecutive steps are depicted.

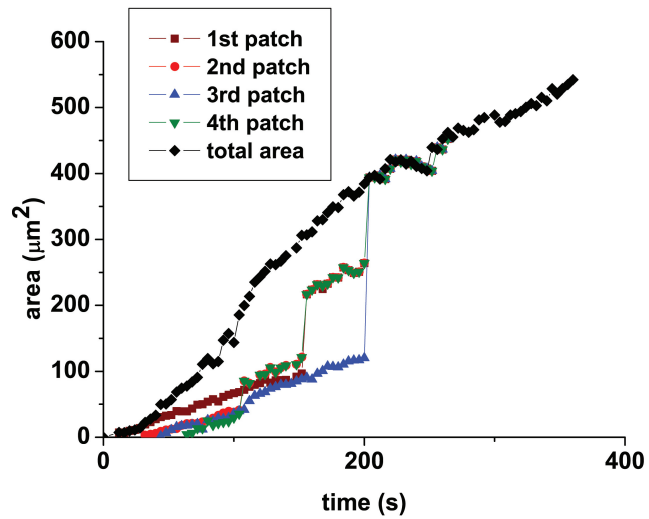


Figure 6.5. Growth of individual adhesion patches with time. The total area (grey) representing the sum of all individual adhesion patches is plotted for comparison.

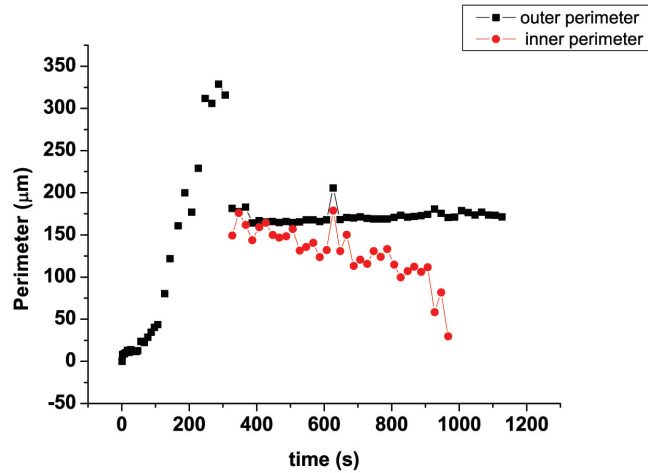


Figure 6.6. Variation of the outer perimeter and the inner perimeter of the adhesive zone with time.

Note that only large floppy vesicles (initial membrane tension $\sim 10^{-6} \frac{N}{m}$) were considered. In general, floppy vesicles underwent all three stages of adhesion. However, it was difficult to treat the data for small vesicles because they adhere to quickly and single patches not be distinguished clearly enough to be treated with imaging software.

B Adhesion Dynamics: Detailed Description

B.1 Formation of Single Adhesion Patches

As explained in reference [178], floppy vesicles sit on a liquid cushion. The adhesion process starts when a membrane fluctuation pierces this cushion and integrins on the vesicle membrane can bind to RGDs on the surface (figure 6.2A). Usually, this occurs at the border of the contact zone which is probably because of the existence of a dimple at the center of the contact zone [178]. The nucleation of an adhesion patch at the edge of the contact zone and the existence of a dimple have been observed in earlier studies of the adhesion of elastomers to a wet surface (mimicking a tire on a road) [207].

Subsequently, other adhesion patches appear and grow in a circular manner and within a couple of minutes these small adhesion zones fuse. The graph in figure 6.5 shows that the contacts appeared at different points in time. As expected, when two patches coalesce, the total area jumps. However, after fusion, the patch continued to grow with the same speed. This graph shows

that the growth velocity is the same for all patches.

Note that it was rather hard to follow these single adhesion patches in microscopy for a long time, since fusion was rapid.

B.1.1 Theoretical Predictions

Similar adhesion behavior was described by P.-H. Puech et al. [179] for the adhesion of biotin-carrying, floppy vesicles onto streptavidin covered supported bilayers. They also observed the development of small adhesion zones which fused during the experiment (see chapter 4). The first stage of the adhesion process can therefore be described by the same theory used in their work.

P.-G. de Gennes and F. Brochard-Wyart developed the following description of the adhesion process. They considered a vesicle covered with a surface concentration of stickers Γ_0 . The vesicle is adhering to a surface and in the adhesion patch the sticker concentration is Γ_{int} . The growth of the contact zone is essentially a dewetting process of the liquid cushion on which the vesicle sits [178] (see also figure 6.7).

For small adhesion patches $R^2 < Dt$ (D = diffusion constant of the ligand in the vesicle, t = time), the diffusion of the stickers (integrin proteins on the vesicle surface) to the adhesion zone is important. For immobilized stickers, the adhesion energy, W , per unit area is given by $W = \Gamma_0 U$, where U is the energy gain per sticker $\sim 10kT$. This corresponds to an equilibrium contact angle θ_E which is defined as [178]

$$W = \sigma(1 - \cos\theta_E) \sim \sigma\theta_E^2/2 \quad (6.1)$$

where σ is the membrane tension.

At time t the number of stickers that entered the adhesion zone is $\pi R^2(\Gamma_{int} - \Gamma_0)$ (Γ_{int} = sticker concentration in adhesion zone, Γ_0 = sticker concentration on the rest of the vesicle).

This has to be equal to the reduction of the number of stickers on the surface area Dt , which is $\Gamma_0 Dt$. From this, it follows that

$$R^2(\Gamma_{int} - \Gamma_0) \sim Dt\Gamma_0 \quad (6.2)$$

Using $W = \Gamma_{int} U = \sigma\theta^2/2$ gives

$$\theta^2 - \theta_E^2 = \frac{DtU}{R^2\sigma}\Gamma_0 \sim \frac{Dt}{R^2}\theta_E^2 \quad (6.3)$$

The equation for the dewetting speed at equilibrium is given by [165]

$$v_d \sim \frac{\sigma}{\eta}\theta_E^3 \quad (6.4)$$

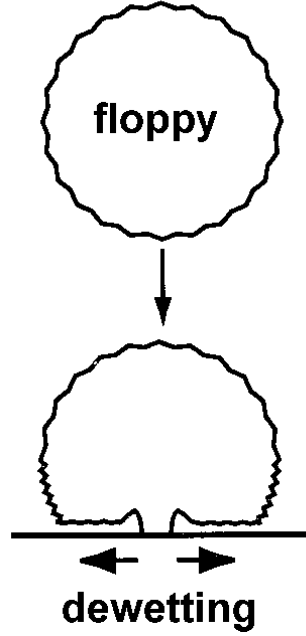


Figure 6.7. *The growth of the contact zone is essentially a dewetting process of the liquid cushion on which the vesicle sits. From [179].*

For $\theta \sim \theta_E$ (i.e. Γ_{int} is not much larger than Γ_0), the dewetting speed v_d is given by [179]

$$v_d = \frac{\sigma}{\eta} \theta_E^3 \left(1 + \frac{Dt}{R^2}\right)^{\frac{3}{2}} \quad (6.5)$$

If $R^2 < Dt$ (which is the case for $Dt \sim 60 \mu\text{m}^2$), from equation 6.5 one can obtain

$$\dot{R}R^3 \sim \frac{\sigma}{\eta} \theta_E^3 D^{\frac{3}{2}} t^{\frac{3}{2}} \quad (6.6)$$

which gives

$$R = \alpha t^{\frac{5}{8}} \quad (6.7)$$

with the prefactor α ,

$$\alpha \sim \left(\frac{\sigma}{\eta} \theta_E^3 D^{\frac{3}{2}}\right)^{\frac{1}{4}} \quad (6.8)$$

B.1.2 Comparison with Experimental Data

B.1.2.1 Fitting the Data As the theory predicts a growth of the radius R of the adhesion zone $\sim t^{\frac{5}{8}}$, the radius was calculated by assuming that

the shape of the individual patches were roughly circular. To compare several adhesion patches which appeared consecutively in time, the data was shifted to $t = 0$. The predicted scaling law $t^{\frac{5}{8}}$ fits the data very well, as shown in figure 6.8:

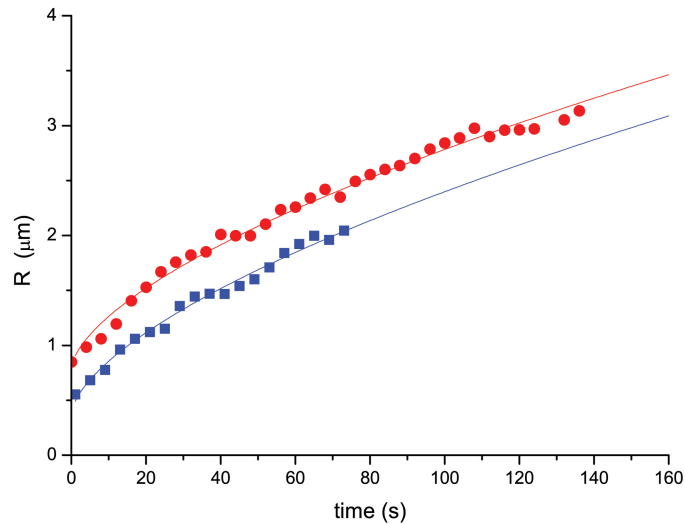


Figure 6.8. The growth of the radius R of two individual adhesion patches is plotted as a function of time, and fitted to a scaling law, $t^{\frac{5}{8}}$, with an off-set in time to shift the data to $t = 0$.

A \sqrt{t} -behavior has been predicted by other theoretical models described in chapter 4 so the data was also fitted to $R \sim \sqrt{t}$. As is evident from the log-log plot in figure 6.9, both ($R \sim t^{\frac{5}{8}}$ and $R \sim t^{\frac{1}{2}}$) fit the data very well and are hard to distinguish. A clear distinction between the two exponents would require more data than is currently available.

B.1.2.2 Discussion Fitting the data to $R = \alpha\sqrt{t}$ yields $\alpha = (0.22 \pm 0.05) \times 10^{-6}$ S.I. while fitting the data to the theoretically predicted power law $R \sim t^{\frac{5}{8}}$ yields the prefactor $\alpha = (0.12 \pm 0.01) \times 10^{-6}$ S.I..

To check if these values are reasonable, they were compared to calculated values of the prefactor. The integrin diffusion coefficient was measured by Gönnerwein et al. by Fluorescence Recovery After Photobleaching (FRAP) to be $D \sim 0.6 \frac{\mu\text{m}^2}{\text{s}}$ [169]. The viscosity of the liquid is $\eta = 10^{-3} \text{Pa}\cdot\text{s}$. The membrane tension σ is expected to be of the order of $10^{-6} \frac{\text{N}}{\text{m}}$. According to Cuvelier et al., θ_E is of the order of 0.2 rad. Substituting these values into equation 6.8 gives a value of the prefactor of 2.4×10^{-6} S.I. which is largely consistent with the experimental value. Thus, the PGG-Brochard-

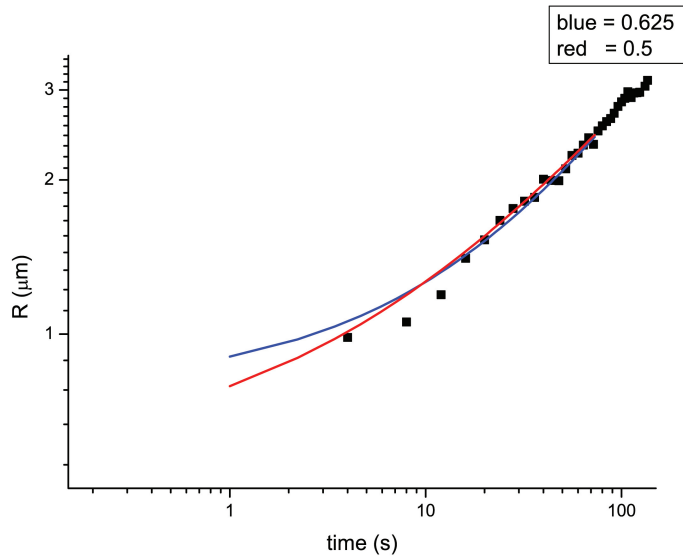


Figure 6.9. *The growth of the radius of an adhesion patch is plotted in a log-log plot and fitted by a power law with an off-set in time to shift the data to $t = 0$. blue line: the exponent = 0.625, as predicted by de Gennes and Brochard-Wyart [179], red line: the exponent = 0.5, as predicted by Boulbitch et al. [140].*

Wyart theory for the growth of adhesion patches of floppy vesicles is consistent with the experimental results.

B.1.3 Conclusion

The adhesion of the integrin-functionalized vesicles starts with several single patches which grow and eventually fuse. This section examined the initial growth of individual patches and compared the experimental data to the theory of de Gennes and Brochard-Wyart. They predicted a growth behavior of $R \sim t^{\frac{5}{8}}$. The experimental data was compared to this law and to the $R \sim t^{\frac{1}{2}}$ law proposed by other groups. Both models are consistent with the available data. The value for the prefactor α was $(0.22 \pm 0.05) \times 10^{-6}$ S.I. for the $R \sim \sqrt{t}$ -regime, and $(0.12 \pm 0.01) \times 10^{-6}$ S.I. for the $R \sim t^{\frac{5}{8}}$ -regime. The estimated value was $\alpha = 2.4 \times 10^{-6}$ S.I. which is reasonably close considering the uncertainty in θ_E . Thus the PGG-Brochard-Wyart theory for the growth of adhesion patches of floppy vesicles describes reasonably well the experimental data.

B.2 Disk Formation

As discussed in section B.1, the first stage of the observed adhesion dynamics was quite similar to the results of P.-H. Puech [179]. In both cases, individual adhesion patches appeared, grew and fused. However, in this system the adhesive patch with a ring-like shape at the rim of the contact zone grew further to eventually form a homogeneous adhesion disk. Interestingly, similar adhesion patches with a ring-like shape were observed in the "inversed" system studied by the group of Prof Sackmann (see also figure 4.16 in chapter 4) [187].

The evolution of the total perimeter (sum of the perimeter of each individual patch) as a function of time (figure 6.6) provides insight into the conversion of the adhesion patch from a ring to a disk. Initially, the total perimeter increased quickly as each of the individual patches grew. After the individual patches fused to form a ring, the total perimeter could then be divided into the inner and outer perimeter of the ring. While the outer perimeter stayed roughly constant, the inner perimeter decreased approximately linearly with time until the ring became a homogeneous adhesion disk.

In figure 6.10, a schematic view of the ring closure is shown. The outer perimeter R_0 stays roughly constant while the inner perimeter R_i reduces to form a disk (indicated by the red arrows). The area A of the adhesive ring can be expressed as,

$$A = \pi R_0^2 - \pi R_i^2. \quad (6.9)$$

Figure 6.11 shows the inner radius R_i as a function of time during disk formation. At short and intermediate times, R diminished linearly with time as

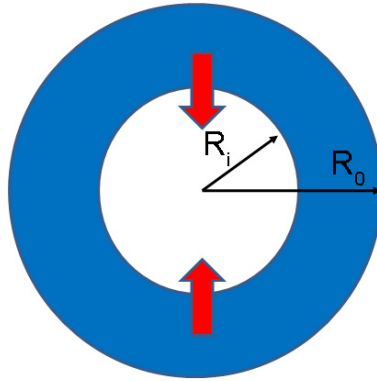


Figure 6.10. Schematic view of the disk formation: The adhesion patch has the shape of a ring in which the external radius R_o stays roughly constant while the inner perimeter R_i diminishes.

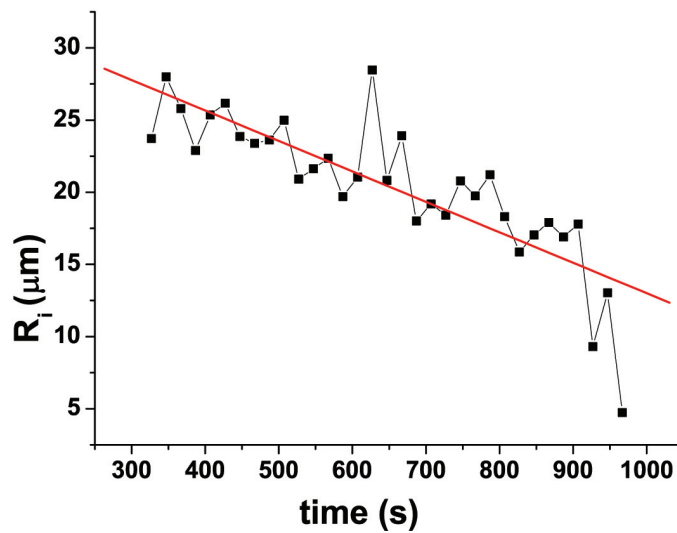


Figure 6.11. The inner radius R diminishes linearly with time as the ring-shaped adhesion patch extended toward the center.

the adhesion patch grew towards the center.

As shown by de Gennes and Brochard-Wyart [178], this last stage can also be described by a dewetting process (see figure 6.12). The liquid which

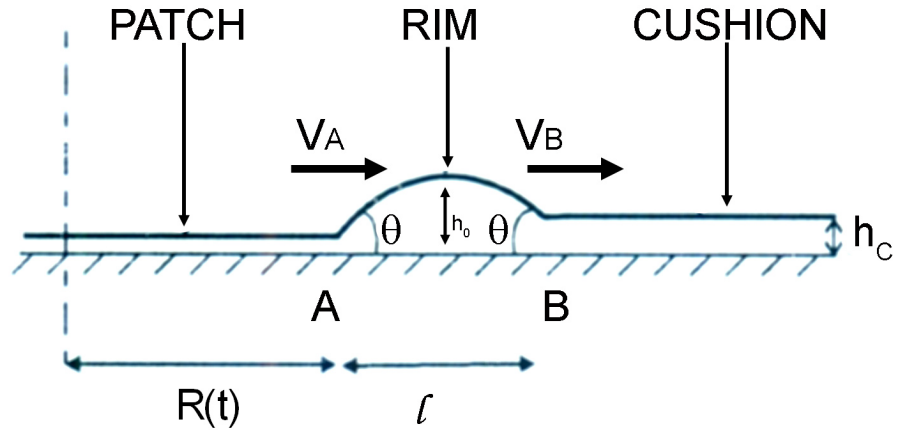


Figure 6.12. The ring-shaped adhesion patch grows toward the center via a dewetting process. The excess liquid is collected in a rim of height h_0 and diameter l . V_A and V_B are respectively the growth velocity of the patch and the retracting velocity of the cushion. h_c is the height of the cushion. From [178].

is pushed away during the spreading is collected in a rim of horizontal size l . According to Laplace's law, the curvature of the rim profile is constant and the angle θ at both ends (point A and B) is the same. The velocities V_A and V_B are nearly the same and are given by the scaling laws

$$\frac{\eta}{\theta} V_A \cong \sigma(\cos\theta - \cos\theta_E) \cong \frac{\sigma}{2}(\theta_E^2 - \theta^2) \quad (6.10)$$

and

$$\frac{\eta}{\theta} V_B \cong \sigma(1 - \cos\theta) \cong \frac{\sigma}{2}\theta^2 \quad (6.11)$$

Whenever the inner radius $R_i \gg h_0/\theta$ (h_0 being the height of the rim), it follows $l \ll R$ (l is the diameter of the rim) and it can be assumed that $V_A = V_B$. From equation 6.10 and 6.11 it follows that $\theta = \theta_E/\sqrt{2}$. The velocity V_A , which corresponds to the variation of the radius R_i with time, can then be described as follows

$$V_A = \frac{dR_i}{dt} = \frac{\sigma}{\eta}\theta_E^3 \quad (6.12)$$

Just outside of the patch there is a depletion of integrins and the concentration of integrin is $\Gamma_+ < \Gamma_0$. Far from the patch the concentration is Γ_0 .

The inward diffusion near the patch is,

$$J = kD \frac{\Gamma_0 - \Gamma_+}{l_D}, \quad (6.13)$$

where Γ_+ is negligible, k is a numerical constant of order unity [178] and the length l_D is the size of the outer diffusion region given by,

$$l_D = \frac{D}{V}, \quad (6.14)$$

where $V \cong dR_i/dt$ is the dewetting velocity.

The number of stickers in the patch is $\Gamma_{int}A = \Gamma_{int}\pi(R_0^2 - R_i^2)$ (A is the area of the patch) and the patch grows with the flux J , so that,

$$\frac{d}{dt} [\pi (R_0^2 - R_i^2) (\Gamma_{int} - \Gamma_0)] = -2\pi R_i J. \quad (6.15)$$

Thus,

$$(\Gamma_{int} - \Gamma_0) dR_i = -J dt. \quad (6.16)$$

Since $\Gamma_+ \ll \Gamma_0$, it then follows that the constant k in equation 6.13 is

$$k = \frac{\Gamma_{int} - \Gamma_0}{\Gamma_0}. \quad (6.17)$$

The concentration in the patch Γ_{int} is then expected to be a constant $\Gamma_{int} = \Gamma_0(1+k)$, and to be of order of Γ_0 .

Equation 6.12 shows that θ_E is constant, and thus the dewetting velocity must also be a constant. Since θ_E is constant, from equation 6.13 follows

$$R_i = -\varepsilon^{\frac{3}{2}} \frac{\sigma}{\eta} t \quad (6.18)$$

with $\varepsilon = \frac{2U\Gamma_0}{\sigma}$, as shown in [208].

B.2.1 The Dewetting Velocity

The inner perimeter of the adhesion zone shrinks with a velocity V , $R_i = Vt$ with $V = -\varepsilon^{\frac{3}{2}} \frac{\sigma}{\eta}$ according to equation 6.18. For the experimental data in figure 6.11, the radius diminished linearly (with $\Delta R \sim 10 \mu\text{m}$) over an interval of roughly $\Delta t \sim 600$ s. Thus, the slope of the curve in figure 6.11 gives a value of $2 \times 10^{-8} \frac{\text{m}}{\text{s}}$ for V .

To see if the theoretical description of initial adhesion dynamics and disk formation were consistent, the prefactors of the two processes were used to compare the integrin diffusion coefficient (see also section B.1 for prefactor α of the first regime).

Keeping in mind that $\Gamma_0 U = \frac{\sigma \theta_E^2}{2}$ (equation 6.1), equation 6.18 can be rewritten

$$R_i = - \left(\frac{2U\Gamma_0}{\sigma} \right)^{\frac{3}{2}} \frac{\sigma}{\eta} t = \theta_E^3 \frac{\sigma}{\eta} t = V t \quad (6.19)$$

$V = -\frac{\sigma \theta_E^3}{\eta}$ and $\alpha = \left(\frac{\sigma \theta_E^3}{\eta} D^{\frac{3}{2}} \right)^{\frac{1}{4}}$, so,

$$\alpha = \left(V D^{\frac{3}{2}} \right)^{\frac{1}{4}}, \quad (6.20)$$

and therefore,

$$D = \left(\frac{\alpha^4}{V} \right)^{\frac{2}{3}} \quad (6.21)$$

with $\alpha = 2 \times 10^{-7}$ S.I. and $V = 2 \times 10^{-8} \frac{m}{s}$. This gives a value of $D \sim 2 \times 10^{-13} \frac{m^2}{s}$. The integrin diffusion coefficient was measured by Gönnerwein et al. to be $\sim 6 \times 10^{-13} \frac{m^2}{s}$ [169]. The experimentally measured value of the dewetting velocity is therefore in reasonable agreement with the value obtained from the model .

B.2.2 Growth from the Edge of the Ring

The final stage of adhesion proceeds by the movement of the edge of the ring toward the center, and not by nucleation of new adhesive patches. The non-adhered membrane in the center of the adhesive ring is tense and it is therefore unlikely that new adhesion patches would nucleate at the center of the remaining water blister. Consequently the adhesion zone grows from the edge of the adhesion zone.

B.2.3 Growth Acceleration at Longer Times

At later stages of adhesion, the center becomes more and more depleted of liquid. From figure 6.11 it is evident that the velocity of the ring closure speeds up and the radius diminishes much faster than $\sim t$. This might be due to membrane fluctuations in the almost depleted dimple, which would allow the membrane to come in contact with the surface. Bonds could then be established more quickly and the adhesion zone would grow faster.

B.2.4 Mechanisms of Water Depletion

The mechanism of liquid depletion from the rim and the non-adhered zone is not understood in detail. Two possible ways are shown in figure 6.13. The liquid could permeate through the lipid membrane or it could flow via the narrow gap between the vesicle membrane and the substrate.

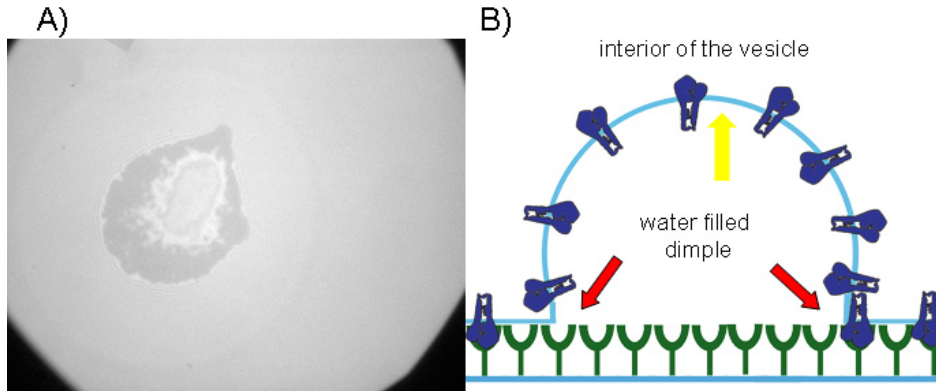


Figure 6.13. Possible mechanisms for water depletion from the central water dimple. A) RICM image of the dimple. B) The liquid can permeate the lipid membrane (yellow) or it can flow through the adhesion patch (red).

B.2.5 Conclusion

The last part of the adhesion process, the disk formation, can be described by a dewetting process, as proposed by de Gennes and Brochard-Wyart [178]. As predicted, the inner radius R diminished at constant velocity (see figure 6.11). The dewetting velocity was approximately $2 \times 10^{-7} \frac{m}{s}$ which was shown to be consistent with the theory. Furthermore, the de Gennes-Brochard-Wyart model suggests that Γ_{int} is constant and similar to Γ_0 implying that no enrichment of stickers occurs in the adhesion zone.

C Conclusion and Perspective

The adhesion of integrin-functionalized vesicles can be separated into three essential steps:

1. Formation of single adhesion patches
2. Coalescence of single patches and ring formation
3. Disk formation

The details of the formation of single patches and the disk formation were compared with theoretical predictions. The intermediate stage, where some patches have fused but others have not, is complex and was not discussed.

In the first step, single adhesion patches of ≈ 200 nm in size appear, grow, and eventually fuse. Theoretical modelling by de Gennes and Brochard-Wyart predicts that the radius of an individual patch grows with $R \sim t^{\frac{5}{8}}$, while other models predict a growth rate of $R \sim \sqrt{t}$ [140]. The experimental data were

fitted equally well by either power law. A larger amount of data will be needed to distinguish clearly between the two models.

Our experiments were consistent with the prediction that the concentration of stickers in the adhesion zone, Γ_{int} , is comparable to the concentration on the rest of the vesicle, Γ_0 . Thus, for this system diffusion does not lead to an enrichment of stickers in the adhesion zone. This has interesting biological consequences. For example, in cells the cytoskeleton might function as a stabilizer to obtain the enrichment of integrin molecules needed to form focal adhesions and similar structures. This could be a control system to prevent unwanted accumulation of integrins.

The third observed stage of the adhesion process is the formation of a homogeneous adhesion patch. It was shown that the ring closes with a constant velocity: $R = Vt$. This adhesion process can be well described by the dewetting model of de Gennes and Brochard-Wyart [178]. The measured dewetting velocity was of order $2 \times 10^{-7} \frac{m}{s}$ which was shown to be consistent with the known integrin diffusion coefficient. Furthermore, the model suggests that the sticker concentration in the adhesion zone, Γ_{int} , should be a constant and similar to the concentration on the rest of the vesicle, Γ_0 , meaning that by diffusion does not enrich the stickers in the adhesion zone.

Several experiments can be proposed to confirm these results. It appears that the concentration in the adhesion patch, Γ_{int} , is comparable concentration on the rest of the vesicle, Γ_0 . It should be possible to confirm this using fluorescently labeled integrin and total internal reflection fluorescence (TIRF) microscopy. TIRF is very sensitive to thin layers on surfaces and should therefore be ideal for observing the adhesion zone close to the substrate.

In addition, the influence of the initial integrin concentration Γ_0 on the vesicle, and the RGD concentration on the substrate should both be investigated. The system could be further developed by introducing an actin cytoskeleton inside the integrin-containing vesicle. If the actin polymers were functionally attached to the integrin proteins in the membrane it would be possible to verify if the actin cortex can lead to enrichment of integrin in small patches, as in the case of focal adhesions. These experiments would show that integrin alone is not able to build focal adhesion spots (no enrichment in the adhesion zone by diffusion), and that triggering actin binding to integrin is necessary. Such a model system could confirm the important role of the actin cytoskeleton in stabilizing integrin-RGD adhesion in biological cells.

CHAPTER 7

Conclusion

Inspired by the work performed in the group of Prof. Sackmann at TU Munich [168], [140], [169] a unique biomimetic system was developed to study early integrin-mediated cell adhesion. The results could be explained with the help of the theoretical models by Françoise Brochard-Wyart and Pierre-Gilles de Gennes.

Improving a method previously developed in our laboratory [3], the transmembrane protein integrin $\alpha_{IIb}\beta_3$ was reconstituted into giant unilamellar vesicles (GUVs). The first step of the method is the detergent-mediated reconstitution of solubilized membrane proteins into small proteoliposomes. For the second step, these preformed proteoliposomes are partially dried under controlled humidity and GUVs are then formed by electrosweeling of the partially dried film. The reconstitution process has been validated by analyzing protein incorporation and biological activity. Confocal microscopy showed that the fluorescently-labeled proteins were homogeneously incorporated into the membrane.

Moreover, after reconstitution, the proteins retain their biological activity as demonstrated by enzyme-linked immunosorbent assay (ELISA) of small vesicles and spectrofluometry on small vesicles interacting with RGD-functionalized quantum dots (RGD is a ligand of integrin $\alpha_{IIb}\beta_3$). Biological activity in GUVs was checked by adhesion tests of the GUVs onto surfaces covered with RGD.

The adhesion of floppy integrin-carrying vesicles onto fibrinogen covered surfaces was studied in detail. In the first step, single adhesion patches of about 200 nm in size form, grow, and eventually fuse. Theoretical modelling by de Gennes and Brochard-Wyart predicted that the radius of a single patch

CHAPTER 7. CONCLUSION

should grow as $R \sim t^{\frac{5}{8}}$, while other models predict growth following of $R \sim \sqrt{t}$ [140]. The data were fitted equally well by both power laws. A larger amount of data will be needed to distinguish clearly between the two models. The prefactor α obtained experimentally was in the same range as the theoretically predicted prefactor.

The intermediate situation, where some patches have fused while others have not, is complex and was not discussed. The third stage of the adhesion process is the formation of a homogeneous adhesion patch. It was shown that the inner ring radius shrinks with a constant velocity. This adhesion process can be well described by a dewetting model of de Gennes and Brochard-Wyart [178]. The measured dewetting velocity was of order $2 \times 10^{-7} \frac{m}{s}$ which was shown to be consistent with theory.

The model suggests that the concentration of stickers in the adhesion zone, Γ_{int} , is of the same order as the concentration in the rest of the vesicle, Γ_0 . This has interesting biological consequences as it implies that enrichment of stickers in the adhesion zones of cells does not result only from the diffusion of stickers. Instead, to obtain enrichment in integrin-rich focal adhesions and similar structures it may be necessary for the cytoskeleton to function as a stabilizer. This may be a control system to prevent unwanted integrin accumulation.

Additional experiments would be helpful to confirm that the concentration of integrin in the adhesion patch Γ_{int} is comparable to the concentration on the rest of the vesicle Γ_0 . One approach would be to image fluorescently labeled integrin via total internal reflection fluorescence (TIRF) microscopy. TIRF is very sensitive to a thin layer above a surface so it would be ideal for observing the adhesion zone. This would allow direct measurement of integrin concentration in the adhered zones and the non-adhering regions.

The influence of the initial integrin concentration Γ_0 on the adhesion dynamics should be investigated. Also, improving the reconstitution method or by exploring new methods for electroformation [128], it might be possible to obtain a higher integrin concentration on the vesicle. Presently, the maximum achievable concentration is 125 integrins per μm^2 which is comparable to the biological concentration on cells. On platelets, however, the concentration of integrin $\alpha_{IIb}\beta_3$ is 10-fold higher. Using other reconstitution methods (e.g. other detergents) it may be possible to produce vesicles with higher protein density.

The RGD concentration on the surface could also be better controlled and varied by using controlled biofunctionalized substrates developed in the group of M. Möller (RWTH Aachen, Germany). This group has developed a method to control the RGD-density on a substrate using multi-branched star-shaped

PEG polymers. First tests on these substrates are under way.

Alternatively, the substrate could be modified using the nanopatterned bio-functionalized surfaces developed in the group of Joachim Spatz [54]. These substrates provide good control of the surface density of RGD ligands. Using these nanopatterned substrates, the Spatz group showed that cells can only adhere to the underlying substrate when the distance between integrin binding sites is below an upper limit. Furthermore, they established that many cell types share this upper limit. Experiments with the integrin-carrying vesicles should be compared with results for cells, to understand the role of the conformational change of adhering integrins, integrin clustering, and the impact of the internal cytoskeleton.

The system could be further improved by introducing an actin cytoskeleton inside the integrin-containing vesicle. Several groups have been working on actin networks in model cells [209], [210], [211] although this is still a challenging task. If the actin polymers could be functionally attached to the integrin proteins in the membrane (see chapter 2), one could check if the actin cortex can lead to enrichment of integrin in small patches (as occurs in focal adhesions) by stabilizing the integrin in the adhesion zone. Initial experiments are under way to combine integrin-containing vesicles with an actin cytoskeleton. These experiments could show that integrin alone is not able to build focal adhesion spots (no enrichment in adhesion zone by diffusion), and that triggering actin binding to integrin is necessary for integrins to cluster in cells. Eventually even proteins like ROCK or mDia1 (as discussed in chapter 2) could be introduced to further expand the system. Such a model system could confirm the important role of the actin cytoskeleton in stabilizing integrin-RGD adhesion in biological cells.

Furthermore, it would be interesting to investigate if integrins act as so-called *catch bonds*. As reported for a member of the selectin family, low forces decrease L-selectin-PSGL-1 off-rates (catch bonds), whereas higher forces increase off-rates (slip bonds) [212]. Catch bonds enabled increasing force to convert short-lived tethers into longer-lived tethers, which decreased rolling velocities and increased the regularity of rolling steps. A similar behavior is predicted for integrins [213], [214]. Using our model system, this hypothesis could be investigated in flow chamber assays.

Introducing more and more components of the complex integrin-actin system would progressively build up the complexity of an artificial cell, bringing it closer to biological systems. Numerous unsolved questions, such as the complex process of internal signaling, could be addressed with such a bottom-up approach. However, the preparation of such complex systems is likely to be

CHAPTER 7. CONCLUSION

experimentally challenging.

Eventually, using such bottom-up approaches should lead to a deeper understanding of cell spreading and cell communication. This should be of interest in medical research in fields such as the integrin-dependent development of tumors. Biomimetic systems may contribute to understanding the role of integrins in these processes and play a role in the development and testing of new therapeutic approaches.

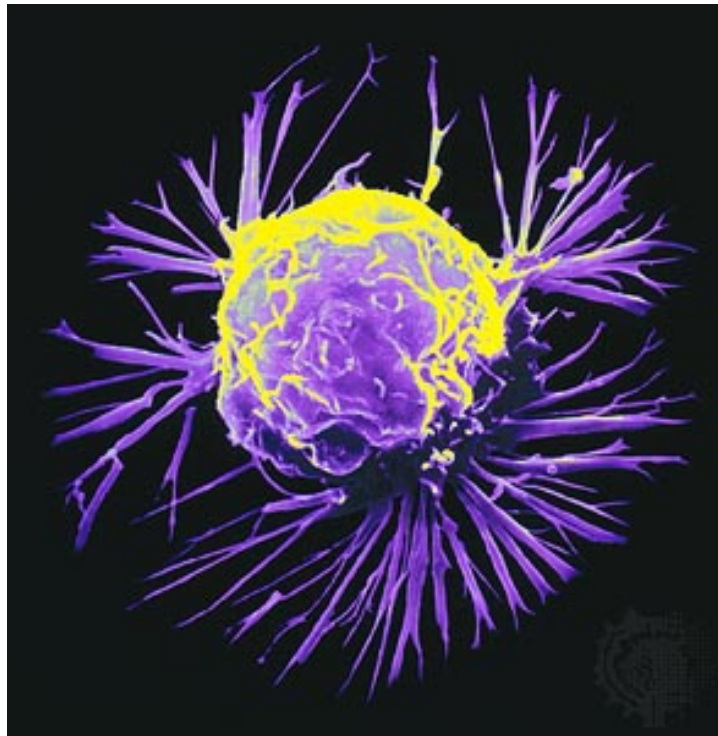


Figure 7.1. *Scanning electron micrograph of a breast cancer cell, showing an abnormally uneven surface and cytoplasmic projections. What is the role of integrin in the development of carcinogenic tissue? From [215].*

APPENDIX A

Materials and Methods

A Materials

A.1 Lipids

Lipids were purchased from Avanti Polar Lipids, Inc., Alabaster, AL, USA. Lipids stocks were in chloroform at a concentration of 10 mg/ml and were stored under an argon atmosphere at -20 °C to prevent lipid degradation.

In this study, the following lipids were used:

Avanti Product Number: 840051
Egg PC 99%
L- α -Phosphatidylcholine (Egg, Chicken)
Molecular Weight: 760 g/mol.

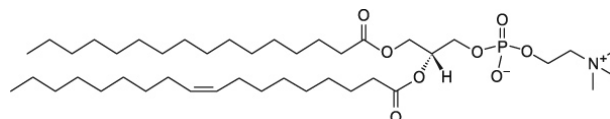


Figure A.1. Molecular structure of Egg PC

Avanti Product Number: 840101
Egg PA
L- α -Phosphatidic Acid (Egg, Chicken-Monosodium Salt)
Molecular Weight: 697 g/mol.

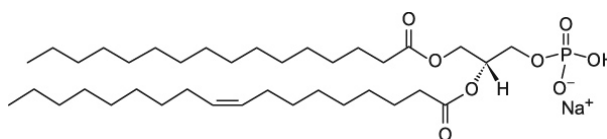


Figure A.2. Molecular structure of Egg PA

Avanti Product Number: 880130
 18:1 PEG2 PE
 1,2-Dioleoyl-*sn*-Glycero-3-Phosphoethanolamine-N-[Methoxy(Polyethylene glycol)-2000] (Ammonium Salt)
 Molecular Weight: 2,801 g/mol.

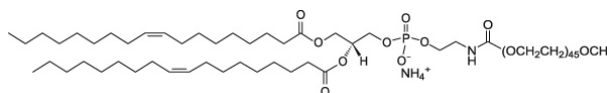


Figure A.3. Molecular structure of DOPE-PEG2000

Avanti Product Number: 880160
 16:0 PEG2 PE
 1,2-Dipalmitoyl-*sn*-Glycero-3-Phosphoethanolamine-N-[Methoxy(Polyethylene glycol)-2000] (Ammonium Salt)
 Molecular Weight: 2,749 g/mol.

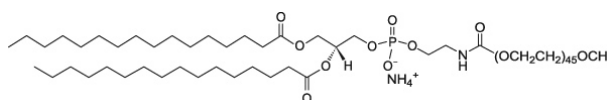


Figure A.4. Molecular structure of DMPE-PEG2000

Avanti Product Number: 880330
 18:1 PEG3 PE
 1,2-Dioleoyl-*sn*-Glycero-3-Phosphoethanolamine-N-[Methoxy(Polyethylene glycol)-3000] (Ammonium Salt)
 Molecular Weight: 3,771 g/mol.

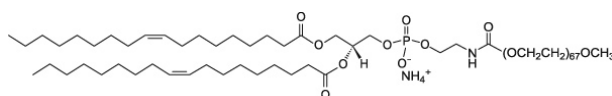


Figure A.5. Molecular structure of DOPE-PEG3000

Avanti Product Number: 880230

18:1 PEG5 PE

1,2-Dioleoyl-*sn*-Glycero-3-Phosphoethanolamine-N-[Methoxy(Polyethylene glycol)-5000] (Ammonium Salt)

Molecular Weight: 5,797 g/mol

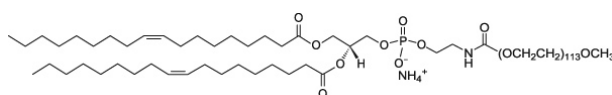


Figure A.6. Molecular structure of DOPE-PEG5000

Avanti Product Number: 850375

18:1 PC (cis)

1,2-Dioleoyl-*sn*-Glycero-3-Phosphocholine (DOPC)

HYGROSCOPIC AS LYOPHILIZED POWDER

Molecular Weight: 786 g/mol

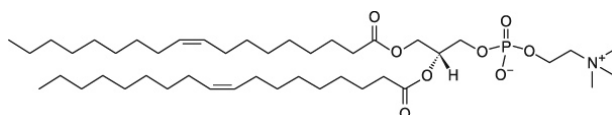


Figure A.7. Molecular structure of DOPC

A.2 Other Products

Solvents were purchased from VWR International, France.

Sugars, poly-L-Lysine (P8920) 0.1% w/v, casein (C6905) and Tris® buffer were purchased from Sigma-Aldrich CO. St.Louis, MO, USA.

Fibrinogen (catalog number: 341578) was purchased from Calbiochem, EMD Chemicals, Inc., Gibbstown, NJ, U.S.A..

Biobeads® SM-2 Adsorbent (catalog number 152-3920) were purchased from Bio-Rad Laboratories, Hercules, CA, U.S.A..

mPEG-Mal-5000(Methoxy-Poly(Ethylene Glycol)Maleimide (average M.W. 5000)) was purchased from Nectar™ Therapeutics, and was later purchased at Sigma Aldrich (catalog number 63187).

HEPES buffer was purchased from ICN Biomedicals Inc., Aurora, OH, USA. Sigillum wax was purchased from Vitrex Medical Limited, Denmark. Parafilm® 992 (Menasha, WI, USA) was used to build observation chambers. ITO conducting glass slides were purchased from PJO GmbH, Iserlohn, Germany.

Glass cover slides from Erie Scientific Company, Portsmouth, NH, USA (No. 1 quality, 0.13-0.16 mm, 40 x 60 mm) and Fisher Scientific International®, USA (No. 1 quality, 0.13-0.17 mm, 25 x 25 mm) were used.

Water was filtered with an Elix® Water Purification System equipped with a 0.22 μm Millipak® filter.

A Heidolph Topmix 94323 was used to vortex the aqueous lipid solution.

SUVs were produced using a tip sonicator from MSE Scientific Instruments, Crawley, UK.

Solution osmolarities were measured with a Roebbling Micro-Osmometer Type 13.

B Methods

Microscope experiments were performed with a Zeiss Axiovert 135 equipped with a CCD camera (CoolSnap^{HQ}, Princeton Instruments) and a Uniblitz shutter. All images were analyzed with software provided with the camera (MetaVue, Universal Imaging Corp.). RICM and fluorescence measurements were performed using a HBO 100 mercury lamp on the epi-fluorescent port with an Antiflex 63x objective. For RICM an interference filter ($\lambda = 546 \text{ nm}$) was used. For phase contrast observation of GUVs, a phase 2 condenser was used together with a 40x Neofluar long distance objective.

For confocal microscopy, a setup based on a commercial Nikon TE2000 inverted microscope (Nikon) was used. The confocal head was an eC1 confocal system (Nikon) with two laser lines (488nm, 543nm).

Images were analyzed with ImageJ (Wayne Rasband, National Institutes of Health, USA, <http://rsb.info.nih.gov/ij/>) and data treated with Origin® (<http://www.OriginLab.com>).

A Hettich EBA 12 centrifuge with a universal 307 rotor was used.

APPENDIX B

Experimental Techniques

This chapter presents all standard microscopy techniques used in this study. The technical details for each experimental setup are given in appendix A. These are

- Reflection Interference Contrast Microscopy (RICM)
- Epifluorescence Microscopy
- Phase Contrast Microscopy
- Confocal Microscopy

A Reflection Interference Contrast Microscopy (RICM)

Reflection interference contrast microscopy (RICM) is a widely used quantitative interference technique to determine the distance between an object and a substrate with nanometer vertical resolution and a lateral resolution of ($\sim 200\text{-}300\text{ nm}$).

As shown in Figure B.1, monochromatic light reflects from both the glass surface and the membrane surface (of the GUV or cell) and the resulting interference pattern depends upon the distance between the two surfaces. It is well adapted to investigate adhesion phenomena in giant vesicles and cells.

Reflection interference microscopy (RIM) has been used as a powerful tool for cell scientists since its introduction by Curtis in 1964 [216]. It was greatly improved by the invention of reflection contrast by Ploem in 1975 [217]. However, quantitative analysis was only possible after the theoretical work of Rädler and Sackmann in 1993 [218]. Currently, the resolution in the surface profile is $0.3\ \mu\text{m}$ laterally and $1\ \text{nm}$ out of plane. The optical thickness of a membrane

can be determined with 0.2 nm accuracy. Dual-wavelength reflection interference contrast microscopy (DW-RICM) using two different wavelengths for illumination has been developed to measure absolute optical distances [219].

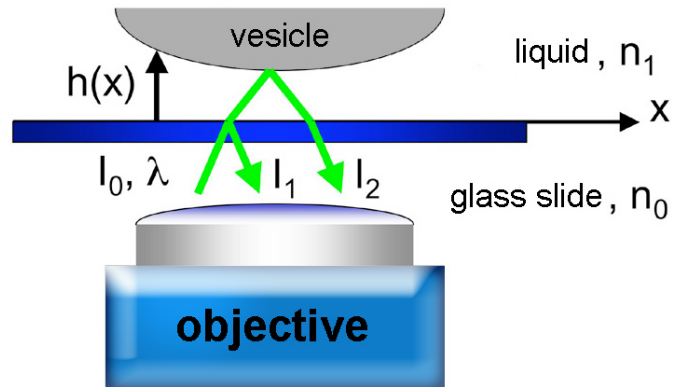


Figure B.1. Schematic of RICM method. A monochromatic light beam (wavelength λ) reflects from both the object and the glass surface to form an interferogram. n_0 and n_1 are the refractive indices of the glass substrate and the medium. I_0 is the initial light intensity, I_1 is the intensity of light reflected from the glass substrate and I_2 is the intensity of the light reflected from the object. From [218].

Figure B.1 depicts the experimental set-up for RICM. For our experiments, the sample consisted of a vesicle sitting on (or adhered to) a glass cover slip which was mounted on an inverted microscope. Monochromatic illumination is provided by a combination of mercury lamp and interference filter ($\lambda = 546$ nm, $\Delta\lambda = 5$ nm, green). This illumination is episcopic, meaning that the sample is illuminated through the objective. The reflected light is then collected by the objective and high resolution images are recorded with a digital camera (CoolSnap^{HQ}, Ropper). An example of an RICM image from a tightly adhered vesicle is shown in figure B.2.

For each point in the image, the intensity is determined by the distance between the substrate and the vesicle membrane at that point. For points in adjacent interference rings, the substrate-vesicle separation differs by,

$$i = \frac{\lambda}{2n_1}, \quad (\text{B.1})$$

where λ is the light wavelength and n_1 is the refraction index of the liquid (for water, $n_1 = 1.33$). When using a wavelength $\lambda = 546$ nm, $i = 205$ nm and the change in separation for a half-fringe (going from light to dark) is only 102.5 nm. Consequently, interference fringes can only be resolved in regions where the substrate and vesicle surfaces are almost parallel. For an approximately spherical object such as a vesicle, this corresponds to the region where the vesicle is close to the substrate ($< 1 \mu\text{m}$) (see figure B.2).

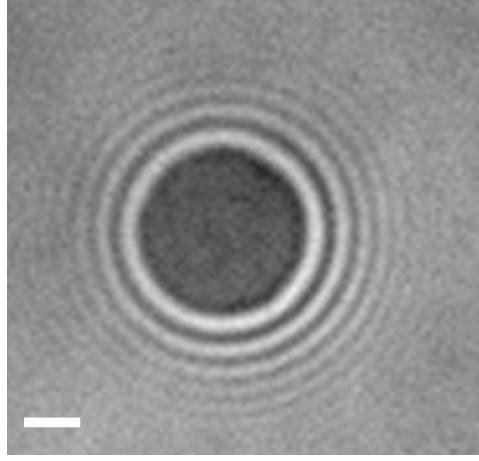


Figure B.2. An RICM image of a vesicle strongly adhering to a substrate. Interference fringes are visible. Bar = 10 μm .

The height profile, $h(x)$, of the object can be obtained by quantitative image analysis. The intensity of the reflections from the substrate-water interface and water-vesicle interface depend on the refractive indices of the substrate (n_0), water (n_1) and vesicle (n_2). The observed (reflected) intensity, $I(h)$, results from the coherent superposition of reflection from the substrate and vesicle surface and is given by

$$I(h) = I_0 \times \frac{r_{01}^2 + 2r_{01}r_{12} \cos 2kh + r_{12}^2}{1 + (r_{01}r_{12})^2 - 2r_{01}r_{12} \cos 2kh} \quad (\text{B.2})$$

where I_0 is the intensity of the incoming beam, $k = 2\pi n_1/\lambda$ is the magnitude of the incident wave-vector and $r_{ij} = (n_i - n_j)/(n_i + n_j)$ is the reflection coefficient of the interface i/j . When terms r_{ij}^n with $n > 2$ are neglected ($r_{ij} \sim 7\%$ for the glass-water interface)

$$I(x) = I_a \sin^2 \left(2\pi \frac{n_1 h(x)}{\lambda} \right) + I_b \quad (\text{B.3})$$

where $I_{max} = I_0(|r_{01}| + |r_{12}|)^2 = I_a + I_b$ is the intensity of the white fringes and $I_{min} = I_0(|r_{01}| - |r_{12}|)^2 = I_b$ is the intensity of the black fringes.

The black circular fringe in the center of figure B.2 corresponds to the adhesion zone of the vesicle.

B Epifluorescence Microscopy

When a fluorescent molecule is illuminated with a light with an excitation wavelength λ_{exc} , the molecule can make a transition from the ground state to

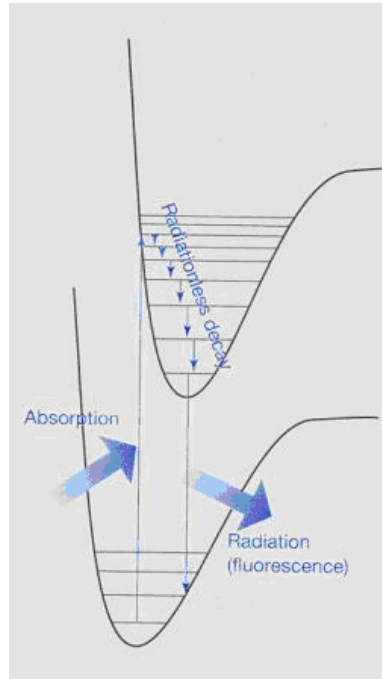


Figure B.3. Schematic representation of molecular fluorescence. From [220].

an excited state (figure B.3) by absorbing a photon. The molecule then relaxes by radiationless decay to lowest excited state. From this lowest excited state, the molecule can make a radiative transition back to the ground state by emitting a photon with wavelength $\lambda_{em} > \lambda_{exc}$. In epifluorescence microscopy, the emitted photons are used to measure the spatial distribution of fluorophores in the sample.

Inverted fluorescence microscopes are equipped with an epi-illumination set-up incorporating interchangeable filter cubes that are matched to the fluorophore. The filter cube is placed beneath the objective and includes a dichroic mirror that couples in the light from the excitation source (figure B.4). Light from the mercury lamp is focussed by a source collector, spatially filtered by a field diaphragm, filtered through a narrow band-pass excitation filter and reflected into the objective by the dichroic beam-splitter. The beam-splitter reflects wavelengths shorter than λ_c and transmits wavelengths longer than λ_c (in practice $\lambda_{exc} < \lambda_c < \lambda_{em}$). Thus, the beam-splitter lets the objective simultaneously serve as a condenser lens for the excitation wavelength and the objective lens for emitted fluorescence. Fluorescent light from the specimen passes straight through the dichroic beam splitter, is filtered by a second band-filter corresponding to λ_{em} and then passes through the optical train of the microscope to reach the ocular and camera. Each fluorescence cube contains the appropriate excitation filter, dichroic beam-splitter, and emission

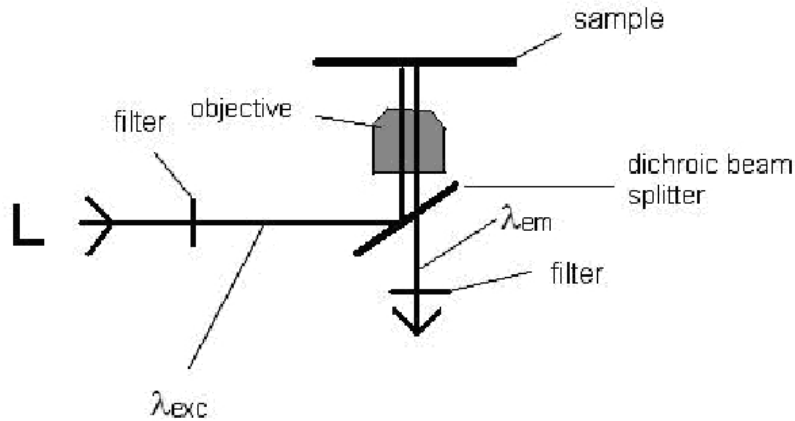


Figure B.4. *Illumination pathway in epifluorescence microscopy.*

filter so they can be rapidly switched as a group to allow imaging of specimens containing multiple fluorophores.

The filters used in our experiments are stated in the experimental section. All images were taken on a Zeiss Axiovert 135 microscope using a cooled, electron multiplying, back-illuminated CCD camera (CoolSnap^{HQ}, Roper) and a Uniblitz shutter. All images were analyzed with MetaVue software (Universal Imaging Corp).

C Phase Contrast Microscopy

Microscopic objects that are distinguished from their surround only by a difference of refractive index lose their Becke line and disappear when brought exactly into focus [221]. (The Becke line is a bright halo of light that appears around the perimeter of a particle when the indices of refraction of the particle and the surrounding medium are different or when the microscope is defocused.) Phase contrast microscopy generates images in which contrast depends on the difference between the refractive index of observed object and the surrounding medium. In conventional dark-field microscopy, an annular aperture is introduced in the focal plane of the condenser and an annular beam-stop is placed in the back focal plane of the objective. When there is no sample in the microscope, light that passes through the condenser annulus is absorbed by the beam-stop in the objective and the image appears "dark". However, a phase object (an object with a different refractive index) scatters some of the light passing through it. This scattered light is not blocked by the annular beam-stop in the objective and forms a bright image of the object.

D Confocal Microscopy

Confocal microscopy is a fluorescence optical imaging technique which can produce sharp fluorescent images of thick specimens. Light from outside the focal plane is eliminated using a confocal pinhole permitting high precision two- and three-dimensional imaging of fluorescent samples [222].

The principle of confocal imaging was patented by Marvin Minsky in 1957 [223], but only became a standard technique in biology at the end of the 1980's. In a conventional (i.e., wide-field) fluorescence microscope, the entire specimen is flooded with light from a light source and so fluorescence is excited throughout the specimen. Although only light originating from the focal plane of the objective is in focus, fluorescence from points behind and in front of the focal plane are also transmitted to the camera. Consequently, sharp features in the focal plane are often obscured by blurry, out-of-focus fluorescence from other parts of the sample.

In contrast, a modern laser scanning confocal microscope (LSCM) eliminates out-of-focus signal using :

- 1) point by point illumination of the sample and
- 2) rejection of out-of-focus fluorescent light.

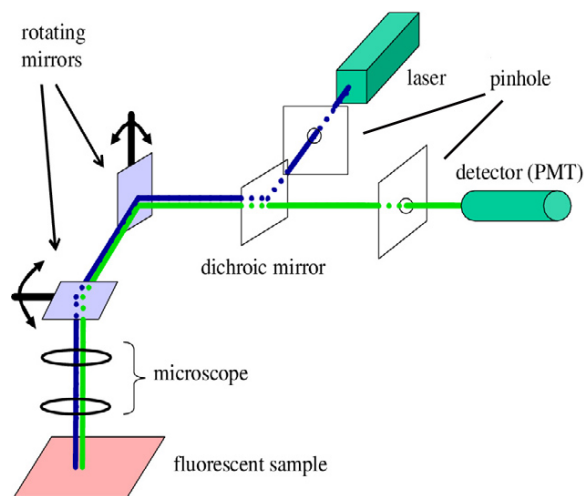


Figure B.5. Schematic diagram of a conventional confocal microscope. The two mirrors scan the light from the laser (pixel by pixel) across the sample to excite fluorescence at each point in the focal plane. The fluorescence signal is collected by the objective, de-scanned by the two mirrors, passes through the dichroic mirror and is brought to a focus at the plane of the observation pinhole. Fluorescence from the focal plane passes through the pinhole and is detected by the PMT. In contrast, fluorescence from behind or in front of the focal plane is out-of-focus at the pinhole and is blocked. Scanning the laser is generally the rate-limiting step for obtaining an image. From [222]

Figure B.5 shows the optical path of a conventional scanning confocal microscope. A laser beam (blue line) passes through the first pinhole and is directed by a dichroic mirror towards a pair of mirrors that scan the light in x and y . The light then passes through the objective and excites the fluorescent sample. The fluorescent (light green) light from the sample passes back through the objective and is descanned by the same mirrors used to scan the sample. The light then passes through the dichroic mirror to a second pinhole placed in the conjugate focal (hence the term confocal) plane of the sample. Fluorescent light from the focal plane of the sample passes through the pinhole, while light from other positions is blocked. Thus, the pinhole selects only the light from the focal plane and the intensity of this signal is then measured by a point detector such as a photomultiplier tube. At each instant only one point of the sample is observed, but by scanning the beam a 2D or 3D image can be obtained. Frequently, confocal microscopy is used because it can isolate the fluorescence from a single plane within the object even in the presence of strong background fluorescence. It is precisely this "sectioning"-ability that enables effective 3D confocal imaging.

Protocols for Protein Purification

A Purification of the Human Platelet Membrane Glycoprotein $\alpha_{IIb}\beta_3$ complex

A.1 Buffers

Nota bene! All buffers should be prepared in plastic beakers.

1. Platelet washing buffer

pH 7.4
0.55 mM acetylsalicylic acid
150 mM NaCl
20 mM Tris HCl
1 mM EDTA

EDTA and acetylsalicylic acid are added to prevent platelet activation.

2. Lysing buffer

pH 7.4
50 mM Tris HCl
1 mM CaCl_2
1 mM MgCl_2
1 % Triton (1 g in 100 ml H_2O)

3. Equilibrating buffer for Con A column

pH 7.4
100 mM NaCl
50 mM Tris HCl
1 mM CaCl₂
1 mM MgCl₂
0.1 % Triton (1 g in 1000 ml H₂O, about 1.6 mM)
0.02 % NaN₃ (3 mM)

4. Elution buffer for Con A column

pH 7.4
100 mM NaCl
50 mM Tris HCl
1 mM CaCl₂
1 mM MgCl₂
0.1 % Triton (1 g in 1000 ml H₂O, about 1.6 mM)
0.02 % NaN₃ (3 mM)
100 mM methyl - D mannopyranoside

5. Equilibrating buffer for Heparin column

pH 7.4
100 mM NaCl
50 mM Tris HCl
1 mM CaCl₂
1 mM MgCl₂
0.1 % Triton (1g in 1000 ml H₂O, about 1.6 mM)
0.02 % NaN₃ (3 mM)

6. Equilibrating buffer for Sepharcryl S300 column

pH 7.4
150 mM NaCl
20 mM Tris HCl
1 mM CaCl₂
1 mM MgCl₂
0.1% Triton (1g in 1000ml H₂O, about 1.6 mM)
0.02 % NaN₃ (3 mM) %

7. Regeneration buffer for Con A/ Heparin columns

pH 7.4
20 mM Tris HCL
1 mM NaCl

8. Regeneration buffer for Sepharycryl S300 column

0.2 mM NaOH

A.2 Purification

Day 1:

Removing Red Cells :

Outdated platelet concentrates (ca. 2500 ml) are used within 14 days of venipuncture. Plastic beakers are used. The ConA-column is equilibrated with buffers (buffers degassed overnight). After centrifugation the red cell pellet is removed.

Centrifugation 215*g for 20 min
Temperature 22°C

Platelet washing:

Centrifugation 1750*g for 30 min
Temperature 22°C

The supernatant is removed and the pellet is weighed.

The pellet is resuspended in the "platelet washing buffer" and washed three times.

Centrifugation 1050*g for 25 min
Temperature 22°C

Cell Lysis:

The pellet is resuspended in 60 ml of the "platelet washing buffer" using a Turrax disperser (20 second/time, 2 times, on ice) and one tablet of Complete™ is added to provide protease inhibitors.

Centrifugation 119000*g for 30 min
Temperature 4°C

Remove the supernatant and keep 1 ml for testing.

Membrane Solubilization:

The pellet is resuspended (Turrax disperser, 20 seconds/time, 2 times, on ice) in 100 ml of the lysing buffer, which contains 1 % Triton. One tablet of Complete™ protease inhibitors is added. The solution is then rotated for 1 hour at 4 °C. A new tablet is added before incubating the sample.

Centrifugation 28200*g for 15 min
Temperature 4°C

The pellet is removed and 1 ml of the supernatant is kept for testing.

The supernatant is now mixed with the material for the Concanavalin A-Sepharose affinity column and the material is applied to the column. Equilibrating buffer for Con A is used to wash the column overnight (0.2 ml/min).

Day 2:

The S300-buffer is degassed. The bound glycoproteins on the Con A column are eluted with the "eluting buffer for Con A".

Bed Volume 20 ml (1.6 x 10 cm)
Flow rate 0.5 ml/min 5ml
5ml/tube room temperature

A 10 % SDS page is prepared, 1 ml of the flow through and the collected elution, respectively, are kept for testing.

Heparin - Sepharose affinity chromatography

The column is equilibrated with the equilibrating buffer for the Heparin column. The elutate from the Con A column (70 ml) is applied to the column. The integrin is in the flow through fractions.

Bed Volume 20 ml (1.6 x 10 cm)
Flow rate 0.5 ml/min 5ml
5ml/tube room temperature

Day 3:

A 10 % SDS PAGE is prepared.

Sephacryl S300 gel filtration

The column is equilibrated with the equilibrating buffer for the Sephacryl column. The elutate from the heparin-sepharous column (65 ml) is concentrated

A. PURIFICATION OF THE HUMAN PLATELET MEMBRANE
GLYCOPROTEIN $\alpha_{IIb}\beta_3$ COMPLEX A

to around 10 ml (Amicon Centriprep) and applied to the column. The integrins are eluted with the equilibrating solution.

Bed Volume 500 ml (2.6 x 100 cm)
Flow rate 1 ml/min
5ml/ tube room temperature

A 10 % SDS PAGE is prepared. The samples are divided into aliquots and stored at -70 °C.

The columns can be regenerated. The Con A and Heparin columns are washed with 1 M NaCl (2 bed volumes) followed by the appropriate column buffer (5 bed volumes).

The S300 column is washed with 0.2M NaOH (2 bed volumes), followed by the appropriate column buffer (3 bed volumes).

The concentration of the obtained integrin is measured using a Bradford kit.

A.3 Enzyme-Linked Immunosorbent Assay (ELISA)

A.3.1 Buffers

1. **S300 buffer**

2L
pH 7.4
150 mM NaCl
20 mM Tris HCl
1 mM CaCl_2
1 mM MgCl_2
0.02 % NaN_3

2. **Diethanolamime solution**

pH 9.5
0.5 mM MgCl_2
100 ml H_2O
10 mM Diethanolamime

3. **p-Nitrophenylphosphat solution**

15 mg in 15 ml Diethanolamime solution

4. **EDTA**

100 mM, pH 8.5

5. **S/T**
400 ml, 0.16 g Tween

6. **S/T/0.1 % Triton**
30 ml, 30 mg Triton

7. **S/T/B**
30 ml, 0.9 g BSA

8. **S/B**
30 ml, 0.9 g BSA

9. **fibrinogen**
plasminogen-depleted, human plasma
100 ml, 80 nM, 2.73 mg in S300

10. **antibody 1**
Rabbit anti-human integrin β_3 polyclonal antibody
1:1000 in S/T/3% BSA

11. **antibody 2**
Anti-rabbit IgG (whole molecule), alkaline phosphate conjugate
1:1000 in S/T/3% BSA

A.3.2 Preparation

ELISA is performed on a 96-well plate (Nunc Immuno Plate, F96 MicroWell™ Maxisorp, 439 454)

1. The wells are coated with fibrinogen in buffer solution, 100 μ l/well overnight.
2. The coated wells are washed twice with 225 μ l buffer solution per well.
3. Unspecific adsorption is blocked with a 3 % BSA solution in buffer solution, which is incubated for 2 h. The wells are not washed afterwards.
4. The integrin is added (in S300/0.04 % Tween/0.01 % Triton solution, 100 μ l/well) and incubated for 1 h.

A. PURIFICATION OF THE HUMAN PLATELET MEMBRANE
GLYCOPROTEIN $\alpha_{IIb}\beta_3$ COMPLEX

B

5. The coated wells are washed twice with 225 μl buffer solution + Tween (S/T) per well.
6. Antibody 1 is applied, 1:1000 in S300/Tween/3 % BSA (S/T/B), 100 μl /well
7. The coated wells are washed four times with 225 μl buffer solution + Tween (S/T) per well.
8. Antibody 2 is applied, 1:1000 in S300/Tween/3 % BSA (S/T/B), 100 μl /well
9. The coated wells are washed four times with 225 μl buffer solution + Tween (S/T) per well.
10. The coated wells are washed twice with 225 μl diethanolamine solution per well.
11. 100 μl of the nitrophenylphosphate solution is applied and incubated for 30 minutes. The solution is left in the well.
12. 100 μl of the EDTA solution is added to each well. The wells turn yellow. Activity can then be quantified with an ELISA reader.

A.4 Fluorescent labeling of the Human Platelet Membrane Glycoprotein $\alpha_{IIb}\beta_3$ complex [1]

Nota bene! Since amine-reactive label is used, TRIS HCl or other buffer containing amines should **not** be used.

10 mg of the integrin is dissolved in 1 ml 0.1 M NaHCO_3 , pH 8.3. The amine-reactive compound (5-(and-6) carboxytetramethylrhodamine, succinimidyl ester, (5(6)-TAMRA, SE), mixed isomers) is dissolved in anhydrous DMF (10mg/ml).

50-100 μl of the fluorescent solution is added slowly (while stirring) to the protein solution and then incubated for 1h at room temperature.

Optional: The reaction is stopped by adding 0.1 ml of freshly prepared 1.5 M hydroxylamine, pH 8.5 and the solution is then left to incubate for 1h.

The protein and the non-bound compound are separated using a gel filtration column (Integrin: superose 6, Pharmacia, Sweden).

The efficiency of the labelling is checked via UV-Vis-spectroscopy.

B Membrane Purification from Human Platelets

B.0.1 Buffers

1. **buffer 1**

1L
pH 7.0
120 mM NaCl
13 mM trisodium citrate
30 mM dextrose

2. **buffer A**

2L
pH 7.4
150 mM NaCl
10 mM TRIS HCl

3. **buffer A + protease blocker**

0.1 mg/ml leupeptin
150 mM NaCl
10 mM TRIS HCl
0.1mM PMSF
10 μ /ml aprotonin

4. **buffer A + Ca²⁺**

2L
pH 7.4
150 mM NaCl
10 mM TRIS HCl
1 mM Ca²⁺

5. Sucrose gradient

9.015 g sucrose
30 ml buffer A

B.1 Purification

Platelet membranes were purified after Smyth et al. [201].

Day 1:

Removing Red Cells :

Outdated platelet concentrates (ca. 2500 ml) are used within 14 days of venipuncture. Plastic beakers are used.

Red cells were removed by centrifugation (pellet = red blood cells)

Centrifugation 215*g for 20 min
Temperature 22°C

Platelets (2.5 L) were isolated from the solution and washed twice in buffer 1.

Centrifugation 700*g for 20 min
Temperature 22°C

The washed platelets were resuspended in buffer A and placed in the pressure chamber (~ 50 ml) of a Parr cell disruption bomb (Parr Instrument Co., Moline, IL, USA). The chamber was filled with nitrogen to a pressure of 8280 kPa and maintained at 22 °C for 30 min before the pressure was rapidly lowered. The contents were discharged into the same buffer + protease blocker.

Day 2:

The resultant suspension was centrifuged in an Ti45 Beckman rotor and resuspended in buffer A.

Centrifugation 100 000*g for 30 min
Temperature 4°C

Sucrose gradient

A 27 % sucrose gradient was prepared and layered over the resuspended solution.

APPENDIX C. PROTOCOLS FOR PROTEIN PURIFICATION B

Centrifugation 100 000*g for 3h
Temperature 4°C

The membranes were recovered from the interface of the sucrose solution, resuspended in buffer A with 1mM CaCl₂, and centrifuged again.

Centrifugation 100 000*g for 1h
Temperature 4°C

A qualitative Bradford test of functionality of the integrin was positive. The protein concentration was not tested.

Preparation Protocols for GUVs

A Preparation of Giant Unilamellar Vesicles without integrin - Standard Protocol

12 μ l of a 1 mg/ml lipid solution (typically EPC or DOPC) in chloroform was spread onto glass ITO-coated slides (slides coated with a thin conductive layer of indium titanium oxide (ITO)). Chloroform was removed by placing the slides in a vacuum chamber for at least two hours. A growth chamber was built using Vitrex Sigillum Wax[®] (see figure D.1B), filled with sucrose solution (osmolarity \sim 170 mOsM) and sealed with the wax. The growth chamber was then connected to a signal generator and vesicles were allowed to swell for three hours. At the beginning of the electroformation process, the voltage was raised using a home-build ramp in intervals of 3 minutes from 20 mV, 60 mV, 0.1 V, 0.3 V, 0.5 V, 0.7 V, 0.9 V to 1.1 V (10 Hz sinusoid, RMS). For the remainder of the three hours, the voltage remained at 1.1 V. Finally, a square wave at 4 Hz and 1.1 V (RMS) was applied for 30 minutes to separate the membranes of individual vesicles. The vesicles were kept at room temperature and used within the following day.

B Preparation of Giant Unilamellar Vesicles with integrin

B.1 Biobeads[®] Preparation

Biobeads[®] were washed once with methanol and then washed several times with water. The solution was thoroughly degassed with the help of a vacuum

pump. Cleaned biobeads® were kept at 4 °C for several weeks. To add biobeads® to the reconstitution solution, a small portion of the biobeads® suspension was poured onto a clean kimwipe. The biobeads® were then rapidly transferred to the reconstitution solution to prevent inactivation via desiccation.

B.2 Initial Munich Protocol

200 μ l of 10 mg/ml EPC : chloroform solution was transferred to a small round glass vial, dried under a nitrogen flow and then placed under vacuum for 2h. 40 μ g of fluorescently-labeled integrin (TAMRA) and 400 μ g of non-labeled integrin in S300/1% triton buffer was added to the lipids and rotated slowly for 30 minutes. The mixture was kept in a water bath at 15 °C for 30 minutes, and then incubated at 37 °C for 90 minutes. The solution was divided between four 1.5 ml Eppendorf vials, each 1/3 filled with biobeads®, and incubated for 1h. The solution was deposited in droplets of 2 μ l onto clean ITO-glass and kept in a saturated atmosphere overnight (see figure D.1A). A chamber was built with Vitrex Sigillum Wax® (see figure D.1B), filled with sucrose solution (osmolarity \sim 170 mOsM) and sealed with the wax.

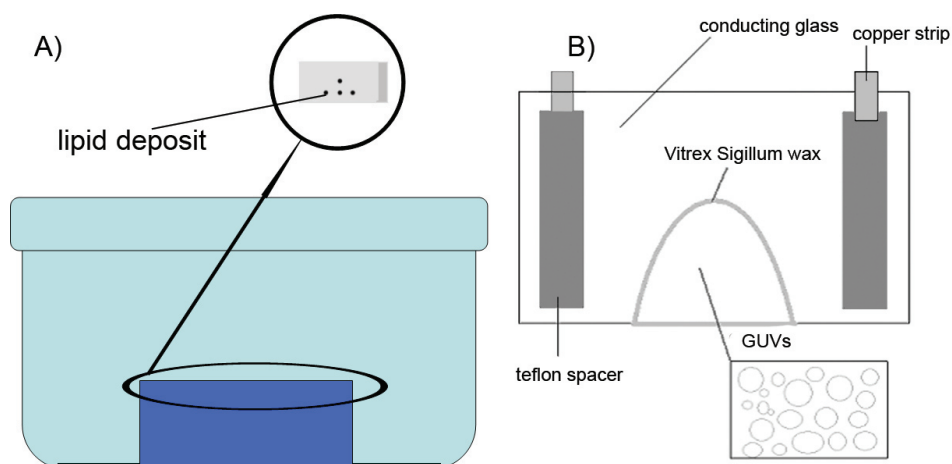


Figure D.1. A chamber is built with Vitrex Sigillum Wax®, filled with sucrose solution (osmolarity \sim 170 mOsM) and sealed with the wax.

The chamber was then connected to signal generator and vesicles were allowed to swell for three hours. The voltage (AC sinusoid, 10Hz) was raised using a home-built ramp in intervals of 3 minutes from 20 mV, 60 mV, 0.1 V, 0.3 V, 0.5 V, 0.7 V, 0.9 V to 1.1 V. For the remainder of the 3 hours, the voltage was kept at 1.1V. Finally, a square wave (4 Hz, 1.1V RMS) was applied for 30 minutes. This method lead to very few, very small (diameter of max. 5 μ m) vesicles.

B.3 Initial Paris Protocol

3800 μl CHCl_3 was added to 200 μl of a 10 mg/ml EPC (in CHCl_3) and the solution was transferred to a round, glass-bottomed vial. The chloroform was removed with a rotary evaporator and the lipid was then thoroughly dried in vacuum for about 1h. 1 ml of H_2O was added (= 2mg/ml) and the solution was vortexed and sonicated with a tip sonicator (90 s). The solution was then divided into 4 aliquots of 250 μl .

Next, 13.4 μl of the integrin (1.5 mg/ml) and 2 μl of a 5 % Triton solution were slowly stirred overnight.

70 μl of the lipid solution and 3.6 μl of a 5% Triton solution were stirred for 30 minutes at room temperature. The protein was then added and the solution was stirred for another 30 minutes. To remove the detergent, 4.2 mg of biobeads® was added and the solution was stirred for 1h. Two further rounds of biobeads were added.

The biobeads® were then removed and 72.2 μl of H_2O was added.

The solution was deposited in droplets of 2 μl onto clean ITO-glass and partially dehydrated overnight (see figureD.1A). A vesicle growth chamber was built with Vitrex Sigillum Wax® (see figureD.1B), filled with sucrose solution (osmolarity ~ 170 mOsM) and sealed with the wax. The chamber was then connected to a signal generator and vesicles were allowed to swell for three hours. The voltage (10Hz sine wave, RMS) was raised using a home-build ramp in intervals of 3 minutes from 20 mV, 60 mV, 0.1 V, 0.3 V, 0.5 V, 0.7 V, 0.9 V to 1.1 V. For the remainder of the growth period, the voltage was kept at 1.1 V. Finally, a square wave (4Hz, 1.1 V RMS) was applied for 30 minutes although this step was not crucial. The method occasionally produced vesicles.

B.4 Final Paris Protocol (higher lipid-integrin-ratio)

280 μl of a 1 mg lipid : 1ml water solution containing 85 mol% EPC, 10 mol% EPA, and 5 mol% DMPE-PEG 2000 was prepared. First, the lipid stock solutions (in chloroform) were mixed in the appropriate proportions. The chloroform was then evaporated in a small vial and the lipid was dried in a vacuum oven for two hours. Water was added to yield a 1 mg/ml solution. The solution was then vortexed and sonicated with a tip sonicator for 60 seconds. The aqueous lipid solution was then mixed with 2.65 μl Triton solution 100x and stirred for 30 minutes at room temperature. 10 μg of integrin (10% TAMRA labeled) was added and stirred for another hour. 15 mg of biobeads® was added and stirred overnight. The resulting solution (1.5 μl / droplet) was deposited onto ITO slides and dried for 3-4 hours in a water-saturated atmosphere. A chamber was built with Vitrex Sigillum Wax® (see figure D.1), filled with sucrose solution (osmolarity \sim 170 mOsM) and sealed with the wax. The chamber was then connected to a signal generator (10 Hz sinusoid) and the vesicles were allowed to swell overnight. The voltage was raised using a home-build ramp in intervals of 3 minutes from 20 mV, 60 mV, 0.1 V, 0.3 V, 0.5 V, 0.7 V, 0.9 V to 1.1 V (RMS). For the remainder of the growth period the voltage was kept at 1.1V (RMS). On a number of occasions, this protocol gave large ($> 15 \mu\text{m}$ in diameter), unilamellar, round GUVs.

C Preparation of Giant Unilamellar Vesicles from purified platelet membranes

Following the dehydration/hydration and electroformation protocol for integrin-containing vesicles, GUVs were grown from the purified membrane preparation (see appendix for preparation details). The solution obtained from membrane purification (1.5 μl / droplet) was deposited onto ITO slides and dried for 3-4 hours (see figure D.1A). A chamber was built with Vitrex Sigillum Wax® (see figure D.1B), filled with sucrose solution (osmolarity \sim 170 mOsM) and sealed with the wax. The chamber was then connected to signal generator and vesicles were allowed to swell over night. The voltage (10Hz sine wave) was raised using a home-build ramp in intervals of 3 minutes from 20 mV, 60 mV, 0.1 V, 0.3 V, 0.5 V, 0.7 V, 0.9 V to 1.1 V (RMS) and then left at this level (1.1V RMS) for the rest of the growth period.

Deposits of the concentrated membrane solution did not produce vesicles. The concentrated membrane solution was diluted with buffer A*. This diluted

C. PREPARATION OF GIANT UNILAMELLAR VESICLES FROM
PURIFIED PLATELET MEMBRANES C

solution was then deposited on ITO slides and vesicles could then be obtained.

buffer A*
2L, pH 7.4
150 mM NaCl
10 mM TRIS

Protocols for Adhesive Surfaces and Adhesion Tests

A Passivated Surfaces

A.1 Preparation of PEG surfaces

The PEG-passivated surfaces were prepared following procedures described by Cuvelier et. al. [145]:

Glass cover slips (24 mm x 50 mm) were treated with a solution of 70 % sulfuric acid and 30 % hydrogen peroxide (piranha solution) for 10 minutes, washed with MilliQ water and stored in methanol. Before use they were dried under nitrogen gas.

A.1.1 Silanisation

The following solution was prepared (**in the following order!**):

1. 55 ml methanol
2. 2.3 ml H₂O
3. 473 μ l glacial acetic acid
4. 1.17 ml mercaptopropyl-trimethoxy-silane

The glass cover slips were mounted on a rack, and incubated in the silanization solution for two hours at room temperature (or overnight at 4 °C). The cover slips were then rinsed twice with methanol, dried under nitrogen gas and

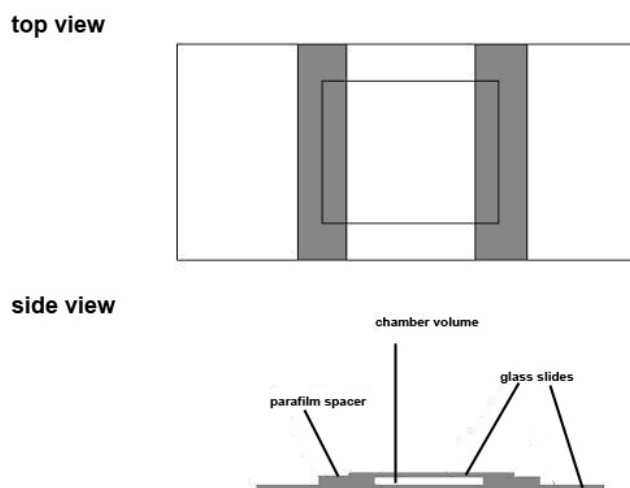


Figure E.1. Observation chamber for RICM and fluorescence microscopy experiments

heated for 5 minutes at 120 °C in air. At this stage, the silanised surfaces were quite stable and could be stored under vacuum for several days.

A.1.2 PEG Binding

A solution of 2 mg/ml mPEG-Mal-5000 (methoxy-poly(ethylene glycole) maleimide average M.W. 5000) in PBS was freshly prepared. 100 μ l of the solution was put on the surface of the glass slide and spread using a piece of Parafilm®. The cover slips were incubated for 1h hour at room temperature. If the results were unsatisfactory, the cover slips were incubated for 2h at room temperature, or overnight at 4 °C.

After incubation the cover slips were washed with MilliQ water and dried under nitrogen gas. Cover slips were then stored under vacuum and could be used up to several weeks later.

A.1.3 Observation Chamber

Observation chambers were built as shown in figure E.1. Two glass cover slips were separated by Parafilm® strips (typically 6 layers) to give a chamber with a volume of approximately 200 μ l. A soldering iron was used to melt the Parafilm® strips so that they firmly adhered to to the glass.

The chamber was filled with buffered glucose* solution and a few microliters of vesicle solution was then injected.

*buffered glucose
pH 7.4
180 mM glucose
10 mM TRIS
1 mM Mg ²⁺
1 mM Mn ²⁺

The chamber was used for RICM, epifluorescence, and phase contrast microscopy.

A.2 Casein Surfaces

Glass cover slips (24 mm x 50 mm) were treated with a solution of 70 % sulfuric acid and 30 % hydrogen peroxide (piranha solution) for 10 minutes, washed with MilliQ water and stored in ethanol. Before use, cover slips were dried under a stream of nitrogen gas. 100 μ l of a 1 ‰ w/v Poly-L-Lysin : water solution was spread across the glass surface by placing a piece of Parafilm® on top of the droplet. The sample was incubated for 10 minutes at room temperature before excess solution was removed with a KimWipe®. 100 μ l of a 1mg/ml casein in 10 mM HEPES (pH 7.4) buffer was filtered (0.2 μ m Millipore filter), spread across the glass surface with a piece of Parafilm®, and incubated for 1h. The sample was then rinsed with a buffered glucose solution (as above). A chamber was assembled as described in Section A.1.3 (see figure E.1). The chamber was filled with the buffer glucose solution and 10 μ l of the vesicle solution was slowly injected through a glass capillary. The vesicles could then be studied by RICM, epifluorescence and phase contrast microscopy.

A.3 Fibrinogen Surfaces

RGD-covered fibrinogen surfaces were prepared using the following protocol. Glass cover slips (24 mm x 50 mm) were treated with a solution of 70 % sulfuric acid and 30 % hydrogen peroxide (piranha solution) for 10 minutes, washed with MilliQ water and stored in ethanol. Coverslips were dried under nitrogen gas and 100 μ l of a 1 ‰ w/v Poly-L-Lysin: water solution was spread across the surface using a piece of Parafilm®. (see figure E.2)

The sample was incubated for 10 minutes at room temperature before excess solution was removed with a KimWipe®. 100 μ l of a 1 mg/ml fibrinogen in 10 mM HEPES buffer was then spread onto the glass surface with a piece of Parafilm®, and incubated for 1h. Finally, the sample was rinsed with buffered glucose solution (as above).

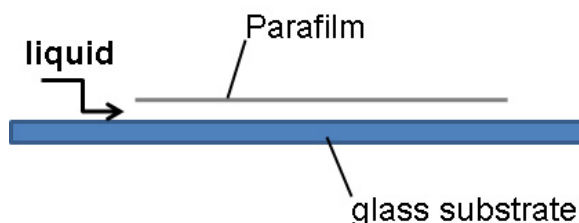


Figure E.2. *A droplet is spread across a glass substrate using a piece of Parafilm®.*

A chamber was assembled as described in Section A.1.3 (see figure E.1). The chamber was filled with the buffer glucose solution and 10 μl of the vesicle solution was slowly injected using a glass capillary. The vesicles were then studied by RICM, epifluorescence and phase contrast microscopy.

B Adhesion Assay for Integrin-Containing GUVs

Fibrinogen surfaces were prepared as described above. 20 μl of the integrin carrying vesicle solution was injected into the observation chamber. The vesicles were studied via RICM, epifluorescence and phase contrast microscopy. First adhesion events occurred within 5 minutes and adhesion took up to 60 minutes to complete.

C Adhesion Assay in the Presence of Soluble RGD

Fibrinogen surfaces were prepared as described above. Meanwhile, 100 μl of the integrin containing GUVs were incubated with 100 μl of a 1 mg/ml RGD solution in 10 mM HEPES, pH 7.4. Vesicles were incubated for 60 minutes. 20 μl of the vesicle-RGD solution was injected into the observation chamber. The vesicles were observed for 30 to 60 minutes using RICM, epifluorescence and phase contrast microscopy.

Protocols for Quantum Dot (QD) Assays

A Fluorescence Microscopy of QDs

Functionalized quantum dots were kindly provided by the group of V. Marchi-Artzner, University of Rennes.

As shown in Figure F.1, the three types of QDs were functionalized with RGD, PEG with a negatively charged end-group, and PEG with a zwitterionic end-group.

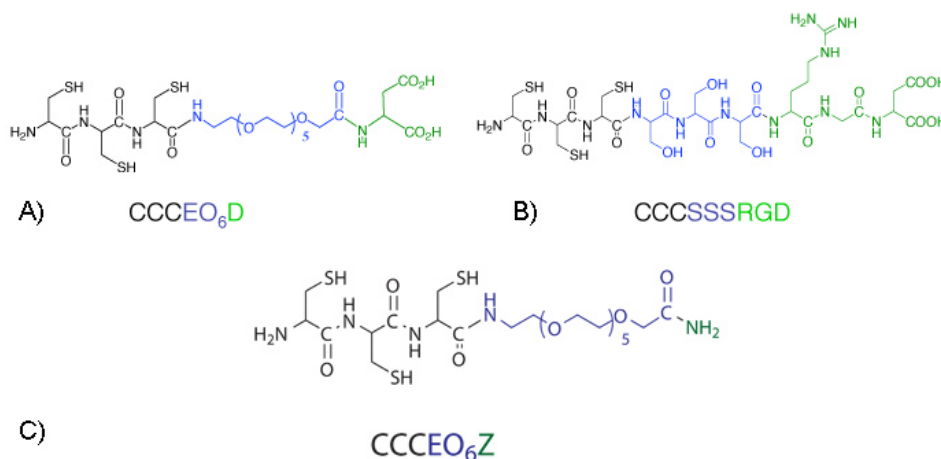


Figure F.1. The functional group on the QDs : A) negatively charged PEG, B) RGD, and C) the zwitterionic group. Private communication A. Dif / V. Marchi-Artzner.

APPENDIX F. PROTOCOLS FOR QUANTUM DOT (QD) ASSAYS B

A.1 Fluorescence Microscopy of Platelets

2 μl of a $2.0\text{-}4.2 \times 10^9$ platelets/ml solution was diluted into 100 μl buffer adjusted to match the platelet's osmolarity and pH.

platelet buffer
314 mOsM, pH 7.4
150 mM NaCl
20 mM TRIS
1 mM Mn^{2+}
1 mM Mg^{2+}

This solution was then incubated with 2 μl of QDs solution (0.8 μM). A 50 % RGD : 50 % negatively charged QD solution was used to study specific binding while a 100 % negatively charged QD solution was prepared for comparison.

The platelets were observed via fluorescence microscopy using a green excitation filter ($\lambda_{max.exc.} = 525 \text{ nm}$, $\lambda_{max.em.} = 565 \text{ nm}$).

B Spectrofluorimetry

B.1 Protocol for Platelets

Buffer was prepared to match the platelet's osmolarity and pH.

platelet buffer
314 mOsM, pH 7.4
150 mM NaCl
20 mM TRIS
1 mM Mn^{2+}
1 mM Mg^{2+}

50 μl of a $2.0\text{-}4.2 \times 10^9$ platelets/ml solution was diluted in 1 ml buffer. This solution was then incubated for 2-5 minutes with 2 μl QDs (0.8 μM). The quantum dot solution consisted of either a 50% RGD : 50 % negatively charged endgroup solution or a 100 % negatively charged PEG solution. A QD blank sample was prepared by mixing 10 μl of the QDs (50 % RGD: 50 % negatively charged endgroup, 0.8 μM) with 500 μl buffer.

To remove unbound quantum dots, the samples were centrifuged for 15 minutes at 14 000 rpm (140 000 g), the supernatant removed and the pellet resuspended in 100 μl of buffer. This process was then repeated. Finally, the fluorescence emission spectrum was measured for $\lambda_{exc} = 360 \text{ nm}$.

B.2 Protocol for Proteoliposomes

Several samples were prepared (all 200 nM):

1. A blank sample containing only QDs (50 % functionalized with RGD : 50 % zwitterionic endgroup) in H₂O
2. Proteoliposomes + RGD QDs (50 % RGD-functionalized : 50 % zwitterionic endgroup)
3. Proteoliposomes + PEG QDs (100 % zwitterionic)
4. Small vesicles without protein + RGD QDs (50 % RGD-functionalized : 50 % zwitterionic endgroup)
5. Small vesicles without protein + PEG QDs (100 % zwitterionic)

While the liposomes/proteoliposomes were incubating (45-60 minutes), solutions were prepared for a sucrose gradient to allow removal of the unbound QDs via ultra-centrifugation.

First, the sample was mixed with a 60 % sucrose solution to give a total volume of 1 ml. 6 ml of 40 % sucrose solution was carefully layered over this solution followed by 3,5 ml of a 5 % sucrose solution. The sample was then centrifuged for 15h at 4 °C (Beckmann L80, rotor SW41, 38 000 rpm). After centrifugation, the liposomes/proteoliposomes formed a white band at the interface of the 5 % and the 40 % solutions. The fluorescence emission spectrum for this fraction was measured for $\lambda_{ex} = 360$ nm.

APPENDIX F. PROTOCOLS FOR QUANTUM DOT (QD) ASSAYS B

Bibliography

- [1] Molecular Probes. *Conjugation with Amine-Reactive Probes*, 0143 edition, 08 98.
- [2] <http://www.nobel.se/medicine/educational/poster/1999/index.html>. time of access: July 18th, 2008.
- [3] P. Girard, J. Pécréaux, P. Falson, J.-L. Rigaud, and P. Bassereau. A new method for the reconstitution of large concentrations of transmembrane proteins into giant unilamellar vesicles. *Biophys. J.*, 87:419–429, 2004.
- [4] J. B. Manneville, P. Bassereau, S. Ramaswamy, and J. Prost. Active membrane fluctuations studied by micropipet aspiration. *Phys. Rev. E*, 64(2 Pt 1):021908, 2001.
- [5] P. S. Frenette and D. D. Wagner. Adhesion molecules—part 1. *N. Eng. J. Med.*, 334(23):1526–1529, 1996.
- [6] <http://www.steve.gb.com/science/>. time of access: July 18th, 2008.
- [7] R. O. Hynes. Integrins: a family of cell surface receptors. *Cell*, 48(4):549–554, 1987.
- [8] B. Alberts. *Molecular Biology of the Cell*. Garland Science, New York, 4th edition edition.
- [9] C. A. Whittaker and R. O. Hynes. Distribution and evolution of von willebrand/integrin a domains: widely dispersed domains with roles in cell adhesion and elsewhere. *Mol. Biol. Cell*, 13(10):3369–3387, 2002.
- [10] R. D. Burke. Invertebrate integrins: structure, function, and evolution. *Int. Rev. Cytol.*, 191:257–284, 1999.

- [11] A. L. Hughes. Evolution of the integrin alpha and beta protein families. *J. Mol. Evol.*, 52(1):63–72, 2001.
- [12] R. O. Hynes and Q. Zhao. The evolution of cell adhesion. *J. Cell Biol.*, 150:89–96, 2000.
- [13] M. J. Humphries. Integrin structure. *Biochem. Soc. Trans.*, 28:311–339, 2000.
- [14] <http://walz.med.harvard.edu/Research/>. time of access: July 18th, 2008.
- [15] P. J. Newman. Platelet GPIIb-IIIa: molecular variations and alloantigens. *Thromb. Haemost.*, 66(1):111–118, 1991.
- [16] B. Hu, S. Senfang, Z. Guttenberg, M. Bärmann, and Sackmann E. Interaction between the integrin $\alpha_{IIb}\beta_3$ and synthesized cyclic hexapeptide containing rgd. *Chinese Science Bulletin*, 45(23):2148–2152, 2000.
- [17] J. J. Calvete. *Cell Adhesion Molecules*. Plenum Press, 1993.
- [18] B. D. Adair and M. Yeager. Three-dimensional model of the human platelet integrin $\alpha_{IIb}\beta_3$ based on electron cryomicroscopy and x-ray crystallography. *Proc. Natl. Acad. Sci. USA*, 99(22):14059–14064, 2002.
- [19] M. Kloszewiak, S. Timmons, T. J. Lukas, and J. Hawiger. Platelet receptor recognition site on human fibrinogen. synthesis and structure-function relationship of peptides corresponding to the carboxyterminal segment of the γ chain. *Biochemistry*, 23:1767–1774, 1984.
- [20] E. F. Plow, S. E. D'Souza, and M. H. Ginsberg. Ligand binding to GPIIb-IIIa: a status report. *Semin. Thromb. Hemostasis.*, 18:324–332, 1992.
- [21] J. Chen, S. Azucena, and T. A. Springer. Bistable regulation of integrin adhesiveness by a bipolar metal ion cluster. *Nature Struc. Biol.*, 10:995–1001, 2003.
- [22] J. Gailit and E. Ruoslahti. Regulation of the fibronectin receptor affinity by divalent cations. *J. Biol. Chem.*, 263:12927–12932, 1988.
- [23] A. P. Mould, S. J. Barton, J. A. Askari, S. E. Craig, and M. J. Humphries. Role of ADMIDAS cation-binding site in ligand recognition by integrin $\alpha_5\beta_1$. *J. Biol. Chem.*, 278:51622–51629, 2003.
- [24] P. E. Hughes and M. Pfaff. Integrin affinity modulation. *Trends Cell Biol.*, 8:359–364, 1998.

- [25] G. A. Marguerie, E. F. Plow, and T. S. Edgington. Human platelets possess an inducible and saturable receptor specific for fibrinogen. *J. Biol. Chem.*, 255:5357–5363, 1979.
- [26] B. Savage and Z. M. Ruggeri. Selective recognition of adhesive sites in surface-bound fibrinogen by glycoprotein IIb-IIIa on nonactivated platelets. *J. Biol. Chem.*, 266:11227–11233, 1991.
- [27] G. A. Marguerie, T. S. Edgington, and E. F. Plow. Interaction of fibrinogen with its platelet receptor as part of a multistep reaction in adp-induced platelet aggregation. *J. Biol. Chem.*, 255:154–161, 1980.
- [28] A. L. Frelinger, X. P. III Du, E. F. Plow, and M. H. Ginsberg. Monoclonal antibodies to ligand-occupied conformers of integrin $\alpha_{IIb}\beta_3$ (glycoprotein IIb-IIIa) alter receptor affinity, specificity, and function. *J. Biol. Chem.*, 266:17106–17111, 1993.
- [29] R. J. Faull, N. L. Kovach, J. M. Harlan, and M. H. Ginsberg. Affinity modulation of integrin alpha 5 beta 1: regulation of the functional response by soluble fibronectin. *J. Cell Biol.*, 121:155–62, 1993.
- [30] T. E. O’Toole, J. C. Loftus, X. Du, A. A. Glass, Z. M. Ruggeri, S. J. Shattil, E. F. Plow, and M. H. Ginsberg. Affinity modulation of the $\alpha_{IIb}\beta_3$ integrin (platelet GPIIb-IIIa) is an intrinsic property of the receptor. *Cell Regul.*, 1:883–893, 1990.
- [31] A. Sonnenberg, A. A. de Melker, A. M. Martinez de Velasco, H. Janssen, J. Calafat, and C. M. Niessen. Formation of hemidesmosomes in cells of a transformed murine mammary tumor cell line and mechanisms involved in adherence of these cells to laminin and kalinin. *J. Cell. Sci.*, 106:1083–1102, 1993.
- [32] J. J. Calvete. Platelet integrin GPIIb/IIIa: Structure-function correlations. an update and lesson from other integrins. *Proc Soc Exp Biol Med*, 222:29–38, 1999.
- [33] J. J. Calvete. Structures of integrin domains and concerted conformational changes in the bidirectional signaling mechanism of $\alpha_{IIb}\beta_3$. *Proc. Soc. Exp. Biol. Med.*, 229:732–744, 2004.
- [34] T. Xiao, J. Takagi, B. S. Collier, J.-H. Wang, and T. A. Springer. Structural basis for allostery in integrins and binding to fibrinogen-mimetic therapeutics. *Nature*, 432:61–67, 2004.
- [35] Y.-Q. Ma, J. Qin, and E. F. Plow. Platelet integrin $\alpha_{IIb}\beta_3$: activation mechanisms. *J. Thromb. Haem.*, 5 (7):1345–1352, 2007.

- [36] J. Takagi and T.A. Springer. Integrin activation and structural rearrangement. *Immunological Reviews*, 186:141, 2002.
- [37] B. Müller, H.G. Zerwes, K. Tangemann, J. Peters, and J. Engel. Two-step binding mechanism of fibrinogen to β_3 integrin reconstituted into planar lipid bilayers. *J. Biol. Chem.*, 268:6800–6808, 1993.
- [38] W. Huber, J. Hurst, D. Schlatter, R. Barner, J. Hübscher, W.C. Kouns, and B. Steiner. Determination of kinetic constants for the interaction between the platelet glycoprotein IIb-IIIa and fibrinogen by means of surface plasmon resonance. *Eur. J. Biol. Chem.*, 227:647–656, 1995.
- [39] B. M. Gumbiner. Proteins associated with the cytoplasmic surface of adhesion molecules. *Neuron*, 11(4):551–564, 1993.
- [40] R. O. Hynes. Integrins: versatility, modulation, and signaling in cell adhesion. *Cell*, 69(1):11–25, 1992.
- [41] B. M. Gumbiner. Cell adhesion: the molecular basis of tissue architecture and morphogenesis. *Cell*, 84(3):345–357, 1996.
- [42] <http://www.ladinfo.org/Adhesion.jpg>. time of access: July 18th, 2008.
- [43] E. J. Kunkel, J. L. Dunne, and K. Ley. Leukocyte arrest during cytokine-dependent inflammation in vivo. *J. Immunol.*, 164(6):3301–3308, 2000.
- [44] R. Alon, D. A. Hammer, and T. A. Springer. Lifetime of the p-selectin-carbohydrate bond and its response to tensile force in hydrodynamic flow. *Nature*, 374(6522):539–542, 1995.
- [45] Y. Takada, X. Ye, and S. Simon. The integrins. *Genome Biol*, 8(5):215, 2007.
- [46] S. W. Schneider, S. Nuschele, A. Wixforth, C. Gorzelanny, A. Alexander-Katz, R. R. Netz, and M. F. Schneider. Shear-induced unfolding triggers adhesion of von willebrand factor fibers. *Proc. Natl. Acad. Sci. USA*, 104(19):7899–7903, 2007.
- [47] www.kup.at/kup/images/browser/747.jpg. time of access: July 18th, 2008.
- [48] M. H. Ginsberg, X. Du, and E. F. Plow. Inside-out integrin signalling. *Curr. Opin. Chem. Biol.*, 4(5):766–771, 1992.
- [49] M. A. Schwartz, M. D. Schaller, and M. H. Ginsberg. Integrins: emerging paradigms of signal transduction. *Annu. Rev. Cell. Dev. Biol.*, 1995.
- [50] S. K. Sastry and A. F. Horwitz. Integrin cytoplasmic domains: mediators of cytoskeletal linkages and extra- and intracellular initiated transmembrane signaling. *Curr. Opin. Chem. Biol.*, 5(5):819–831, 1993.

- [51] Y. P. Chen, T. E. O'Toole, T. Shipley, J. Forsyth, S. E. LaFlamme, K. M. Yamada, S. J. Shattil, and M. H. Ginsberg. "inside-out" signal transduction inhibited by isolated integrin cytoplasmic domains. *J. Biol. Chem.*, 269(28):18307–18310, 1994.
- [52] H. Lodish, A. Berk, C. A. Kaiser, M. Krieger, M. P. Scott, A. Bretscher, H. Ploegh, and P. T. Matsudaira. *Molecular Cell Biology*. 6th edition edition, 2007.
- [53] D. Cuvelier, M. Théry, Y.-S. Chu, S. Dufour, J.-P. Thiéry, M. Bornens, P. Nassoy, and L. Mahadevan. The universal dynamics of cell spreading. *Curr. Biol.*, 17(8):694–699, 2007.
- [54] M. Arnold, E. A. Cavalcanti-Adam, R. Glass, J. Blümmel, W. Eck, M. Kantlehner, H. Kessler, and J. P. Spatz. Activation of integrin function by nanopatterned adhesive interfaces. *ChemPhysChem*, 5(3):383–388, 2004.
- [55] S. V. Graeter, J. Huang, N. Perschmann, M. López-García, H. Kessler, J. Ding, and J. P. Spatz. Mimicking cellular environments by nanostructured soft interfaces. *Nano. Lett.*, 7(5):1413–1418, 2007.
- [56] D. E. Discher, P. Janmey, and Y.-L. Wang. Tissue cells feel and respond to the stiffness of their substrate. *Science*, 310(5751):1139–1143, 2005.
- [57] J.P. Spatz and B. Geiger. Molecular engineering of cellular environments: cell adhesion to nano-digital surfaces. *Methods Cell Biol.*, 83:89–111, 2007.
- [58] E. Zamir and B. Geiger. Components of cell-matrix adhesions. *J. Cell Sci.*, 114(Pt 20):3577–3579, 2001.
- [59] C. D. Nobes and A. Hall. Rho, Rac, and Cdc42 GTPases regulate the assembly of multimolecular focal complexes associated with actin stress fibers, lamellipodia, and filopodia. *Cell*, 81(1):53–62, 1995.
- [60] K. Rottner, A. Hall, and J. V. Small. Interplay between Rac and Rho in the control of substrate contact dynamics. *Curr. Biol.*, 9(12):640–648, 1999.
- [61] M. A. del Pozo, L. S. Price, N. B. Alderson, X. D. Ren, and M. A. Schwartz. Adhesion to the extracellular matrix regulates the coupling of the small GTPase Rac to its effector PAK. *EMBO J.*, 19(9):2008–2014, 2000.
- [62] E. A. Clark, W. G. King, J. S. Brugge, M. Symons, and R. O. Hynes. Integrin-mediated signals regulated by members of the Rho family of GTPases. *J. Cell Biol.*, 142(2):573–586, 1998.

- [63] B. Geiger and A. Bershadsky. Assembly and mechanosensory function of focal contacts. *Curr. Opin. Chem. Biol.*, 13(5):584–592, 2001.
- [64] M. Amano, Y. Fukata, and K. Kaibuchi. Regulation and functions of Rho-associated kinase. *Exp. Cell Res.*, 261(1):44–51, 2000.
- [65] G. Totsukawa, Y. Yamakita, S. Yamashiro, D. J. Hartshorne, Y. Sasaki, and F. Matsumura. Distinct roles of ROCK (Rho-kinase) and MLCK in spatial regulation of MLC phosphorylation for assembly of stress fibers and focal adhesions in 3T3 fibroblasts. *J. Cell Biol.*, 150(4):797–806, 2000.
- [66] T. Ishizaki, Y. Morishima, M. Okamoto, T. Furuyashiki, T. Kato, and S. Narumiya. Coordination of microtubules and the actin cytoskeleton by the Rho effector mDia1. *Nat. Cell Biol.*, 3(1):8–14, 2001.
- [67] D. Riveline, E. Zamir, N. Q. Balaban, U. S. Schwarz, T. Ishizaki, S. Narumiya, Z. Kam, B. Geiger, and A. D. Bershadsky. Focal contacts as mechanosensors: externally applied local mechanical force induces growth of focal contacts by an mDia1-dependent and ROCK- independent mechanism. *J. Cell Biol.*, 153(6):1175–86, 2001.
- [68] I. Kaverina, K. Rottner, and J. V. Small. Targeting, capture, and stabilization of microtubules at early focal adhesions. *J. Cell Biol.*, 142(1):181–190, 1998.
- [69] I. Kaverina, O. Krylyshkina, and J. V. Small. Microtubule targeting of substrate contacts promotes their relaxation and dissociation. *J. Cell Biol.*, 146(5):1033–1044, 1999.
- [70] I. Kaverina, O. Krylyshkina, M. Gimona, K. Beningo, Y. L. Wang, and J. V. Small. Enforced polarisation and locomotion of fibroblasts lacking microtubules. *Curr. Biol.*, 10(12):739–742, 2000.
- [71] T. Shemesh, B. Geiger, A. D. Bershadsky, and M. I. M. Kozlov. Focal adhesions as mechanosensors: a physical mechanism. *Proc. Natl. Acad. Sci. USA*, 102(35):12383–12388, 2005.
- [72] A. Besser and S. A. Safran. Force-induced adsorption and anisotropic growth of focal adhesions. *Biophys. J.*, 90(10):3469–3484, 2006.
- [73] <http://encarta.msn.com/>. time of access: July 18th, 2008.
- [74] J. N. Israelachvili. *Intermolecular and Surface Forces*. Academic Press, London, 2nd edition edition, 1992.
- [75] R. Lipowsky and E. Sackmann, editors. *Structure and Dynamics of Membranes*. Elsevier North Holland, Amsterdam.

- [76] J. E. Rothman and J. Lenard. Membrane asymmetry. *Science*, 195(4280):743–753, 1977.
- [77] P. F. Devaux and R. Morris. Transmembrane asymmetry and lateral domains in biological membranes. *Traffic*, 5(4):241–246, 2004.
- [78] R. L. Smith and E. Oldfield. Dynamic structure of membranes by deuterium NMR. *Science*, 225(4659):280–288, 1984.
- [79] M. J. Saxton and K. Jacobson. Single-particle tracking: applications to membrane dynamics. *Annu Rev Biophys Biomol Struct*, 26:373–399, 1997.
- [80] D. Axelrod, D. E. Koppel, J. Schlessinger, E. Elson, and W. W. Webb. Mobility measurement by analysis of fluorescence photobleaching recovery kinetics. *Biophys. J.*, 16(9):1055–1069, 1976.
- [81] E. Haustein and P. Schwille. Fluorescence correlation spectroscopy: novel variations of an established technique. *Annu. Rev. Biophys. Biomol. Struct.*, 36:151–169, 2007.
- [82] D. Baeriswyl, editor. *Physics in living matter*. Academic Press, 2nd edition edition, 1987.
- [83] G. Cevc and D. Marsh. *Phospholipid bilayers: physical principles and models*, volume 5 of *Cell biology: a series of monographs*. John Wiley & Sons, Inc., New York, 1987.
- [84] Michael Jansen. *Untersuchungen der Wasserpermeation durch Lipid-membranen*. PhD thesis, Universität Kaiserslautern, 1994.
- [85] D. Needham K. Olbrich, W. Rawicz and E. Evans. Water permeability and mechanical strength of polyunsaturated lipid bilayers. *Biophys. J.*, 79:321–327, 2000.
- [86] O. Sandre, L. Moreaux, and F. Brochard-Wyart. Dynamics of transient pores in stretched vesicles. *Proc. Natl. Acad. Sci. USA*, 96:10591–10596, 1999.
- [87] P. B. Canham. The minimum energy of bending as a possible explanation of the biconcave shape of the human red blood cell. *J. Theor. Biol.*, 26(1):61–81, 1970.
- [88] W. Helfrich. Elastic properties of lipid bilayers: theory and possible experiments. *Z. Naturforsch. [C]*, 28(11):693–703, 1973.
- [89] E. A. Evans. Bending resistance and chemically induced moments in membrane bilayers. *Biophys. J.*, 14(12):923–931, 1974.

- [90] R. Kwok and E. Evans. Thermoelasticity of large lecithin bilayer vesicles. *Biophys. J.*, 35(3):637–652, 1981.
- [91] M. Bloom, E. Evans, and O. G. Mouritsen. Physical properties of the fluid lipid-bilayer component of cell membranes : a perspective. *Quart. Rev. Biophys.*, 24:293–397, 1991.
- [92] E. A. Evans and W. Rawicz. Entropy-driven tension and bending elasticity in condensed-fluid membranes. *Phys. Rev. Lett.*, 64(17):2094–2097, 1990.
- [93] K. Olbrich, W. Rawicz, D. Needham, and E. Evans. Water permeability and mechanical strength of polyunsaturated lipid bilayers. *Biophys. J.*, 79(1):321–327, 2000.
- [94] P.-H. Puech, N. Borghi, E. Karatekin, and F. Brochard-Wyart. Line thermodynamics: adsorption at a membrane edge. *Phys. Rev. Lett.*, 90(12):128304, 2003.
- [95] J. F. Faucon, M. D. Mitov, P. Méléard, I. Bivas, and P. Bothorel. Bending elasticity and thermal fluctuations of lipid membranes. theoretical and experimental requirements. *J. Phys. France*, 50:2389–2414, 1985.
- [96] M. A. Peterson, H. Strey, and E. Sackmann. Theoretical and phase contrast microscopic eigenmode analysis of erythrocyte flicker : amplitudes. *J. Phys. II France*, 2:1273–1285, 1992.
- [97] J. Pécréaux, H.-G. Döbereiner, J. Prost, J.-F. Joanny, and P. Bassereau. Refined contour analysis of giant unilamellar vesicles. *Eur. Phys. J. E*, 13:277–290, 2004.
- [98] P. Méléard, J.-F. Faucon, M. D. Mitov, and Bothorel P. Pulsed-light microscopy applied to the measurement of the bending elasticity of giant liposomes. *Europhysics Letters*, 19:267–271, 1992.
- [99] M. Kummrow and W. Helfrich. Deformation of giant lipid vesicles by electric fields. *Phys. Rev. A*, 44(12):8356–8360, 1991.
- [100] J.-C. Bacri, V. Cabuil, A.C. Cebers, C Menager, and R. Perzynski. Flattening of ferro-vesicles undulations under a magnetic field. *Europhysics Letters*, 33:235–240, 1996.
- [101] D. V. Zhelev, D. Needham, and R. M. Hochmuth. A novel micropipet method for measuring the bending modulus of vesicle membranes. *Biophys. J.*, 67(2):720–727, 1994.
- [102] L. Miao, U. Seifert, M. Wortis, and H.-G. Döbereiner. Budding transitions of fluid-bilayer vesicles: The effect of area-difference elasticity. *Phys. Rev. E*, 49(6):5389–5407, 1994.

-
- [103] H.-G. Döbereiner. *"Fluctuating vesicle shapes" in Giant vesicles*. Perspectives in Supramolecular Chemistry. John Wiley & Sons, 2000.
- [104] E. Sackmann. The seventh Datta lecture. Membrane bending energy concept of vesicle- and cell-shapes and shape-transitions. *FEBS Lett.*, 346(1):3–16, 1994.
- [105] T. Browicz. Further observation of motion phenomena on red blood cells in pathological states. *Zbl. med. Wissen*, 28:625–627, 1890.
- [106] F. Brochard and J.-F. Lennon. Frequency spectrum of the flicker phenomenon in erythrocytes. *Journal de Physique*, 36:1035–1047, 1975.
- [107] Philippe Girard. *Membranes hors d'équilibre: échanges et transport actif*. PhD thesis, Université de Paris VII, 2004.
- [108] W. Helfrich and R.M. Servuss. Undulations, steric interactions and cohesion of fluid membranes. *Il Nuovo Cimento*, 3 D:137–161, 1984.
- [109] J. B. Fournier, A. Ajdari, and L. Peliti. Effective-area elasticity and tension of micromanipulated membranes. *Phys. Rev. Lett.*, 86(21):4970–4973, 2001.
- [110] W. Wintz, H.G. Döbereiner, and U. Seifert. Starfish vesicles. *Europhys. Lett.*, 33:403–408, 1996.
- [111] R. Lipowsky and E. Sackmann, editors. *Structure and dynamics of membranes: from cells to vesicles*, volume 1A. Elsevier science B.V., 1995.
- [112] S. Svetina and B. Zeks. Membrane bending energy and shape determination of phospholipid vesicles and red blood cells. *Eur. Biophys. J.*, 17(2):101–111, 1989.
- [113] U. Seifert. Configurations of fluid membranes and vesicles. *Advances in Physics*, 46:13–137, 1997.
- [114] V. Heinrich, B. Bozic, S. Svetina, and B. Zeks. Vesicle deformation by an axial load: from elongated shapes to tethered vesicles. *Biophys. J.*, 76(4):2056–2071, 1999.
- [115] R. E. Waugh, J. Song, S. Svetina, and B. Zeks. Local and nonlocal curvature elasticity in bilayer membranes by tether formation from lecithin vesicles. *Biophys. J.*, 61(4):974–982, 1992.
- [116] H.-G. Döbereiner, E. Evans, M. Kraus, U. Seifert, and M. Wortis. Mapping vesicles shapes into the phase diagram: a comparison of experiment and theory. *Phys. Rev. E*, 55:4458–4474, 1997.

- [117] R. Heinrich, S. Svetina, and B. Zeks. Nonaxisymmetric vesicle shapes in a generalized bilayer-couple model and the transition between oblate and prolate axisymmetric shapes. *Phys. Rev. E*, 48(4):3112–3123, 1993.
- [118] M. Jaric, U. Seifert, W. Wintz, and M. Wortis. Vesicular instabilities: The prolate-to-oblate transition and other shape instabilities of fluid bilayer membranes. *Phys. Rev. E*, 52(6):6623–6634, 1995.
- [119] H.-G. Döbereiner, E. A. Evans, U. Seifert, and M. Wortis. Spinodal fluctuations of budding vesicles. *Phys. Rev. Lett.*, 75(18):3360–3363, 1995.
- [120] J. Käs and E. Sackmann. Shape transitions and shape stability of giant phospholipid vesicles in pure water induced by area-to-volume changes. *Biophys. J.*, 60:825–844, 1991.
- [121] H. G. Döbereiner, J. Käs, D. Noppl, I. Sprenger, and E. Sackmann. Budding and fission of vesicles. *Biophys. J.*, 65(4):1396–1403, 1993.
- [122] E. Farge and P. F. Devaux. Shape changes of giant liposomes induced by an asymmetric transmembrane distribution of phospholipids. *Biophys. J.*, 61(2):347–357, 1992.
- [123] Y. Jie, L. Quanhui, L. Jixing, and O.-Y. Zhing-Can. Numerical observation of nonaxisymmetric vesicles in fluid membranes. *Phys. Rev. E*, 58:4730–4736, 1998.
- [124] Y.-H. Chan and S. G. Boxer. Model membrane systems and their applications. *Curr. Opin. Chem. Biol.*, 11(6):581–587, 2007.
- [125] M. I. Angelova, S. Soléau, P. Méléard, J. F. Faucon, and P. Bothorel. Preparation of giant vesicles by external ac electric fields. kinetics and applications. *Progr. Colloid. Polym. Sci.*, 89:127–131, 1992.
- [126] L. Mathivet, S. Cribier, and P.F. Devaux. Shape change and physical properties of giant phospholipid vesicles prepared in the presence of an ac electrical field. *Biophys. J.*, 70:1112–1121, 1996.
- [127] P. Sens and H. Isambert. Undulation instability of lipid membranes under electric field. *Phys. Rev. Lett.*, 88(12):128101–128114, 2002.
- [128] L. R. Montes, A. Alonso, F. M. Goni, and L. A. Bagatolli. Giant unilamellar vesicles electroformed from native membranes and organic lipid mixtures under physiological conditions. *Biophys. J.*, 93:3548–3554, 2007.
- [129] Jean-Baptiste Manneville. *Fluctuations de Membranes Actives*. PhD thesis, Institut Curie, 1999.

- [130] T. Pott, H. Bouvras, and P Méléard. Giant unilamellar vesicle formation under physiologically relevant conditions. *Chem. Phys. Lipids*, article in press, 2008.
- [131] N. Rodriguez, F. Pincet, and S. Cribier. Giant vesicles formed by gentle hydration and electroformation: a comparison by fluorescence microscopy. *Colloids Surf. B Biointerfaces*, 42(2):125–130, 2005.
- [132] <http://www.ecs.umass.edu/hamiltion/2003/juanavendano.htm>. time of access: July 18th, 2008.
- [133] M. Karlsson, K. Scott, A.-S. Cans, A. Karlsson, R. Karlsson, and O. Orwar. Micropipet-assisted formation of microscopic networks of unilamellar lipid bilayer nanotubes and containers. *Langmuir*, 17:6754–6758, 2000.
- [134] Nicolas Biais. *Systèmes biomimétiques vésiculaires confinés. Méthodes et applications à l'encapsulation d'asters de microtubules et de ferrofluides*. PhD thesis, Université Paris VII: Paris, 2004.
- [135] H. Aranda-Espinoza and et al. Electrostatic repulsion of positively charged vesicles and negatively charged objects. *Science*, 285(5426):394–397, 1999.
- [136] T. Baumgart, S. T. Hess, and W. W. Webb. Imaging coexisting fluid domains in biomembrane models coupling curvature and line tension. *Nature*, 425(6960):821–824, 2003.
- [137] S. L. Veatch and S. L. Keller. Separation of liquid phases in giant vesicles of ternary mixtures of phospholipids and cholesterol. *Biophys. J.*, 85:3074–3083, 2003.
- [138] L. A. Bagatolli and E. Gratton. Two photon fluorescence microscopy of coexisting lipid domains in giant unilamellar vesicles of binary phospholipid mixtures. *Biophys. J.*, 78(1):290–305, 2000.
- [139] M. K. Doeven, J. H. A. Folgering, V. Krasnikov, E. R. Geertsma, G. van den Bogaart, and B. Poolman. Distribution, lateral mobility and function of membrane proteins incorporated into giant unilamellar vesicles. *Biophys. J.*, 88(2):1134–1142, 2005.
- [140] A. Boulbitch, Z. Guttenberg, and E. Sackmann. Kinetics of membrane adhesion mediated by ligand-receptor interaction studied with a biomimetic system. *Biophys. J.*, 81(5):2743–2751, 2001.
- [141] L. Limozin and E. Sackmann. Polymorphism of cross-linked actin networks in giant vesicles. *Phys. Rev. Lett.*, 89:168103, 2002.

- [142] L. Limozin, A. Roth, and E. Sackmann. Microviscoelastic moduli of biomimetic cell envelopes. *Phys. Rev. Lett.*, 95(17):178101, 2005.
- [143] D. K. Fygenson, M. Elbaum, B. Schraiman, and A. Libchaber. Microtubules and vesicles under controlled tension. *Phys. Rev. E*, 55(1):850–859, 1997.
- [144] V. Emsellem, O. Cardoso, and P. Tabeling. Vesicle deformation by microtubules: A phase diagram. *Phys. Rev. E*, 58:4807–4810, 1998.
- [145] D. Cuvelier, C. Vezy, A. Viallat, P. Bassereau, and P. Nassoy. Mimicking cell/extracellular matrix adhesion with lipid membranes and solid substrates: Requirements, pitfalls and proposals. *J. Phys.: Condensed Matter*, 16:2427–2437, 2004.
- [146] V. Noireaux and A. Libchaber. A vesicle bioreactor as a step toward an artificial cell assembly. *Proc. Natl. Acad. Sci. USA*, 101 (51):17669–17674, 2004.
- [147] S. Pautot, B.J. Frisken, and D.A. Weitz. Production of unilamellar vesicles using an inverted emulsion. *Langmuir*, 19 (7):2870–2879, 2003.
- [148] J. C. Stachowiak, D. L. Richmond, T. H. Li, A. P. Liu, S. H. Parekh, and D. A. Fletcher. Unilamellar vesicle formation and encapsulation by microfluidic jetting. *Proc. Natl. Acad. Sci. USA*, 105:4697–4702, 2008.
- [149] S. Safran. *Statistical Thermodynamics of Surfaces, Interfaces and Membranes*. Westview Press, 1994.
- [150] E. Zimmerman, B. Geiger, and L. Addadi. Initial stages of cell-matrix adhesion can be mediated and modulated by cell-surface hyaluronan. *Biophys. J.*, 82(4):1848–1857, 2002.
- [151] http://www.botany.ubc.ca/biol350/section4/22_02.jpg. time of access: July 18th, 2008.
- [152] E. Evans. Probing the relation between force–lifetime–and chemistry in single molecular bonds. *Annu. Rev. Biophys. Biomol. Struct.*, 30:105–128, 2001.
- [153] R. Merkel, P. Nassoy, A. Leung, K. Ritchie, and E. Evans. Energy landscapes of receptor ligand bonds explored with dynamic force spectroscopy. *Nature*, 397:20–21, 1999.
- [154] G. I. Bell. Models for the specific adhesion of cells to cells. *Science*, 200(4342):618–627, 1978.
- [155] P. Bongrand, P. Claesson, and A. Curtis, editors. *Studying Cell Adhesion*. Springer, Heidelberg, 1994.

- [156] G. Kaplanski, C. Farnarier, O. Tissot, A. Pierres, A.-M. Benoliel, M.-C. Alessi, S. Kaplanski, and P. Bongrand. Analysis of transient binding events mediated by e-selectin in a laminar shear flow. *Biophys. J.*, 64:1922–1933, 1993.
- [157] E. Evans, D. Berk, and A. Leung. Detachment of agglutinin-bonded red blood cells. I. Forces to rupture molecular-point attachments. *Biophys. J.*, 59(4):838–848, 1991.
- [158] E. L. Florin, V. T. Moy, and H. E. Gaub. Adhesion forces between individual ligand-receptor pairs. *Science*, 264(5157):415–417, 1994.
- [159] A. Pierres, A. M. Benoliel, and P. Bongrand. Use of a laminar flow chamber to study the rate of bond formation and dissociation between surface-bound adhesion molecules: effect of applied force and distance between surfaces. *Faraday Discuss.*, (111):321–30; discussion 331–43, 1998.
- [160] A. Pierres, D. Touchard, A.-M. Benoliel, and P. Bongrand. Dissecting streptavidin-biotin interaction with a laminar flow chamber. *Biophys. J.*, 82(6):3214–3223, 2002.
- [161] A. Pierres, A. M. Benoliel, P. Bongrand, and P. A. van der Merwe. Determination of the lifetime and force dependence of interactions of single bonds between surface-attached CD2 and CD48 adhesion molecules. *Proc. Natl. Acad. Sci. USA*, 93(26):15114–15118, 1996.
- [162] E. Evans, K. Ritchie, and R. Merkel. Sensitive force technique to probe molecular adhesion and structural linkages at biological interfaces. *Biophys. J.*, 68(6):2580–2587, 1995.
- [163] Damien Cuvelier. *Adhésion cellulaire et tubes de membrane : Quelques aspects dynamiques, mécaniques et rhéologiques*. PhD thesis, Université Pierre et Marie Curie, 2005.
- [164] P.-G. de Gennes. Wettings: statics and dynamics. *Rev. Mod. Phys.*, 57:827–863, 1985.
- [165] P.-G. de Gennes, F. Brochard Wyart, and D. Quéré. *Gouttes, bulles, perles et ondes*. Belin, 2002.
- [166] J. Rädler, T. J. Feder, H. H. Strey, and E. Sackmann. Fluctuation analysis of tension-controlled undulation forces between giant vesicles and solid substrates. *Phys. Rev. E*, 51:4526–4536, 1995.
- [167] D. Cuvelier, O. Rossier, P. Bassereau, and P. Nassoy. Micropatterned "adherent/repellent" glass surfaces for studying the spreading kinetics of individual red blood cells onto protein-decorated substrates. *Eur. Biophys. J.*, 32(4):342–354, 2003.

- [168] Z. Guttenberg, A. R. Bausch, Bin Hu, R. Bruinsma, L. Moroder, and E. Sackmann. Measuring ligand-receptor unbinding forces with magnetic beads: Molecular leverage. *Langmuir*, 16:8984–8993, 2000.
- [169] S. Gönnenwein, M. Tanaka, B. Hu, L. Moroder, and E. Sackmann. Functional incorporation of integrins into solid supported membranes on ultrathin films of cellulose: impact on adhesion. *Biophys. J.*, 85(1):646–655, 2003.
- [170] P.-H. Puech and F. Brochard. Membrane tensiometer for heavy giant vesicles. *Eur. Phys. J. E*, 15:127–132, 2004.
- [171] U. Seifert and R. Lipowsky. Adhesion of vesicles. *Phys. Rev. A*, 42(8):4768–4771, 1990.
- [172] R. Lipowsky and U. Seifert. Adhesion of vesicles and membrane. *Molecular Crystals and Liquid Crystals*, 202:17–25, 1991.
- [173] U. Seifert and R. Lipowsky. *Adhesion and unbinding of vesicles*. Nova Science Publisher, 1993.
- [174] C. Tordeux, J.-B. Fournier, and P. Galatola. Analytical characterization of adhering vesicles. *Phys. Rev. E*, 65(4 Pt 1):041912, 2002.
- [175] M. Dvolaitzky, P.-G. de Gennes, M.-A. Guedeau, and L. Jullien. Une perceuse moléculaire? = A molecular drill? *C. R. Seances Acad. Sci. Sér.2*, 316:1687–1690., 1993.
- [176] S.R. Hodges and O.E. Jensen. Spreading and peeling dynamics in a model of cell adhesion. *J. Fluid Mech.*, 460:387–409, 2002.
- [177] V. B. Shenoy and L. B. Freund. Growth and shape stability of a biological membrane adhesion complex in the diffusion-mediated regime. *Proc. Natl. Acad. Sci. USA*, 102(9):3213–3218, 2005.
- [178] P.-G. de Gennes, Puech. P.-H., and F. Brochard-Wyart. Adhesion induced by mobile stickers: A list of scenarios. *Langmuir*, 19:7112–7119, 2003.
- [179] P.-H. Puech, V. Askovic, P.-G. de Gennes, and F. Brochard-Wyart. Dynamics of vesicle adhesion: Spreading versus dewetting coupled to binder diffusion. *Biophys. Rev. Lett.*, 1:85–95, 2006.
- [180] D. Cuvelier and P. Nassoy. Hidden dynamics of vesicle adhesion induced by specific stickers. *Phys. Rev. Lett.*, 93:228101–4, 2004.
- [181] E. Karatekin, O. Sandre, H. Guitouni, N. Borghi, P.-H. Puech, and F. Brochard-Wyart. Cascades of transient pores in giant vesicles: line tension and transport. *Biophys. J.*, 84(3):1734–1749, 2003.

- [182] A. Kloboucek, A. Behrisch, J. Faix, and E. Sackmann. Adhesion-induced receptor segregation and adhesion plaque formation: A model membrane study. *Biophys. J.*, 77(4):2311–2328, 1999.
- [183] A. Alberstdörfer, T. Feder, and E. Sackmann. Adhesion-induced domain formation by interplay of long-range repulsion and short-range attraction force: A model membrane study. *Biophys. J.*, 73:245–257, 1997.
- [184] J. R. Nardi, R. Bruinsma, and Sackmann E. Adhesion induced reorganisation of charged fluid membranes. *Phys. Rev. E*, 58:6340–6354, 1998.
- [185] A. Smith, B. G. Lorz, U. Seifert, and E. Sackmann. Antagonist-induced deadhesion of specifically adhered vesicles. *Biophys. J.*, 90(3):1064–1080, 2006.
- [186] B. G. Lorz, A. Smith, C. Gege, and E. Sackmann. Adhesion of giant vesicles mediated by weak binding of sialyl-lewisx to e-selectin in the presence of repelling poly(ethylene glycol) molecules. *Langmuir*, 23(24):12293–12300, 2007.
- [187] V. Marchi-Artzner, B. G. Lorz, C. Gosse, R. Merkel L. Jullien, H. Kessler, and E. Sackmann. Adhesion of arg-gly-asp (rgd) peptide vesicles onto an integrin surface: Visualization of the segregation of rgd ligands into the adhesion plaques by fluorescence. *Langmuir*, 19 (3):835–841, 2003.
- [188] B. Hu, D. Finsinger, K. Peter, Z. Guttenberg, M. Bärmann, H. Kessler, A. Escherich, L Moroder, W. Baumeister, S. Sui, and E. Sackmann. Intervesicle cross-linking with integrin $\alpha_{IIb}\beta_3$ and cyclic RGD-lipopeptide. a model of cell- adhesion processes. *Biochemistry*, 39:12284–12294, 2000.
- [189] Stefanie Gönnerwein. *Generic and Specific Cell Adhesion: Investigations of a Model System by Micro-Interferometry*. PhD thesis, TU Munich, 2003.
- [190] D. Levy, A. Gulik, A. A. Bluzat, and J.-L. Rigaud. Reconstitution of the sarcoplasmic reticulum Ca^{2+} -ATPase: mechanisms of membrane protein insertion into liposomes during reconstitution procedures involving the use of detergents. *Biochim. Biophys. Acta.*, 1107:283–298, 1992.
- [191] J.-L. Rigaud, D. Levy, G. Mosser, and O. Lambert. Detergent removal by non-polar polystyrene beads: application to membrane reconstitution and two-dimensional crystallization. *Eur. Biophys. J.*, 27:305–319, 1998.

- [192] D. Lévy, A. Bluzat, M. Seigneuret, and J. L. Rigaud. A systematic study of liposome and proteoliposome reconstitution involving biobead-mediated triton x-100 removal. *Biochim. Biophys. Acta*, 1025(2):179–190, 1990.
- [193] J. L. Rigaud, B. Pitard, and D. Levy. Reconstitution of membrane proteins into liposomes: application to energy-transducing membrane proteins. *Biochim. Biophys. Acta*, 1231(3):223–246, 1995.
- [194] L.V. Parise and D.R. Phillips. Reconstitution of the purified platelet fibrinogen receptor. *J. Biol. Chem.*, 260:10698–10707, 1985.
- [195] E.M. Erb, K. Tangemann, B. Bohrmann, B. Müller, and J. Engel. Integrin $\alpha_{IIb}\beta_3$ reconstituted into lipid bilayers is nonclustered in its activated state but clusters after fibrinogen binding. *Biochemistry*, 36:7395–7402, 1997.
- [196] G. Conforti, A. Zanetti, I. Pasquali-Ronchetti, D Quaglino, Jr., P. Neyroz, and E. Dejanaz. Modulation of vitronectin receptor binding by membrane lipid composition. *J. Biol. Chem.*, 265:4011–4019, 1990.
- [197] Pierre-Henri Puech. *Vésicules géantes décorées-adhésion et transport*. PhD thesis, Université Paris VI, 2003.
- [198] E. Evans, D. J. Klingenberg, W. Rawicz, and F. Szoka. Interactions between polymer-grafted membranes in concentrated solutions of free polymer. *Langmuir*, 12(12):3031–3037, 1996.
- [199] N. T. Neff, C. Lowrey, C. Decker, A. Tovar, C. Damsky, C. Buck, and A. F. Horwitz. A monoclonal antibody detaches embryonic skeletal muscle from extracellular matrices. *J. Cell Biol.*, 95:654–666, 1982.
- [200] Kai Peter. *Isolation und Charakterisierung des Zellrezeptors Integrin $\alpha_{IIb}\beta_3$ - Studie zur Bindung an zytosolische Proteine und biokompatible Oberflächen*. PhD thesis, Technische Universität München, 1999.
- [201] S. S. Smyth and L. V. Parise. Regulation of ligand binding to glycoprotein IIb-IIIa (integrin $\alpha_{IIb}\beta_3$) in isolated platelet membranes. *Biochem. J.*, 292:749–758, 1993.
- [202] A. Roux, G. Cappello, J. Cartaud, J. Prost, B. Goud, and P. Bassereau. A minimal system allowing tubulation with molecular motors pulling on giant liposomes. *Proc. Natl. Acad. Sci. USA*, 99(8):5394–5399, 2002.
- [203] J.N. Israelachvili. The different faces of poly(ethylene glycol). *Proc. Natl. Acad. Sci. USA*, 94:8378–8379, 1997.

- [204] L. Chai, R. Goldberg, N. Kampf, and J Klein. Selective adsorption of poly(ethylene oxide) onto a charged surface mediated by alkali metal ions. *Langmuir*, 24:1570–1576, 2008.
- [205] G. Lei and R.C. MacDonald. Effects on interactions of oppositely charged phospholipid vesicles of covalent attachment of polyethylene glycol oligomers to their surfaces: Adhesion, hemifusion, full fusion and "endocytosis". *J. Membrane Biol.*, 221:97–106, 2008.
- [206] P. Vermette and L. Meagher. Interactions of phospholipid-and poly(ethylene glycol)-modified surfaces with biological systems: relation to physico-chemical properties and mechanisms. *Colloids and Surfaces B: Biointerfaces*, 28:153–198, 2003.
- [207] P. Martin and F. Brochard. Dewetting at soft interfaces. *Phys. Rev. Lett.*, 80:3296–3299, 1998.
- [208] F. Brochard-Wyart and P.-G. de Gennes. Adhesion induced by mobile binders: Dynamics. *Proc. Nat. Acad. Sci. U.S.A.*, 99:7854–7859, 2002.
- [209] L. Limozin and E. Sackmann. Polymorphism of cross-linked actin networks in giant vesicles. *Phys. Rev. Lett.*, 89(16):168103, 2002.
- [210] A. P. Liu and D. A. Fletcher. Actin polymerization serves as a membrane domain switch in model lipid bilayers. *Biophys. J.*, 91(11):4064–4070, 2006.
- [211] J. Heuvingh, M. Franco, P. Chavrier, and C. Sykes. Arf1-mediated actin polymerization produces movement of artificial vesicles. *Proc. Natl. Acad. Sci. USA*, 104(43):16928–16933, 2007.
- [212] T. Yago, J. Wu, C. Diana Wey, A. G. Klopocki, C. Zhu, and R. P. McEver. Catch bonds govern adhesion through I-selectin at threshold shear. *J. Cell Biol.*, 166(6):913–923, 2004.
- [213] M. Dembo, D. C. Torney, K. Saxman, and D. Hammer. The reaction-limited kinetics of membrane-to-surface adhesion and detachment. *Proc R Soc Lond B Biol Sci*, 234(1274):55–83, 1988.
- [214] J. Emsley, C. G. Knight, R. W. Farndale, M. J. Barnes, and R. C. Liddington. Structural basis of collagen recognition by integrin alpha2beta1. *Cell*, 101(1):47–56, 2000.
- [215] www.britannica.com. time of access: July 18th, 2008.
- [216] A. Curtis. The mechanism of adhesion of cells to glass. *J. Cell Biol.*, 20:199, 1964.

- [217] J. S. Ploem. *Reflection-contrast microscopy as a tool for investigation of the attachment of living cells to a glass surface*. Mononuclear Phagocytes in Immunity. Oxford: Blackwell Scientific Publications, infection and pathology edition, 1975.
- [218] J. Rädler and E. Sackmann. Imaging optical thickness and separation distances of phospholipid vesicles at solid surfaces. *Journal de Physique II France*, 3:727, 1993.
- [219] J. Schilling, K. Sengupta, S. Goennenwein, A. R. Bausch, and E. Sackmann. Absolute interfacial distance measurements by dual-wavelength reflection interference contrast microscopy. *Phys. Rev. E*, 69(2 Pt 1):021901, 2004.
- [220] P. Atkins. *Physical Chemistry*. Oxford University Press, Oxford, 7th ed edition, 2002.
- [221] F. Zernike. *Concepts in Classical Optics*, chapter The wave theory of microscopy image formation, pages 525–536. W.H. Freeman, San Fransisco, 1958.
- [222] V. Prasad, D. Semwogerere, and E. R. Weeks. Confocal microscopy of colloids. *J. Phys.: Condens. Matter*, 19:113102–113127, 2007.
- [223] M. Minsky. (patent publication number: Us3013467), 1957.